UNIVERSITA' DEGLI STUDI
DI VERONA

DEPARTMENT OF BIOTECHNOLOGY

GRADUATE SCHOOL OF SCIENCE ENGINEERING AND MEDICINE

DOCTORAL PROGRAM IN
NANOTECHNOLOGY AND NANOMATERIALS FOR BIOMEDICAL APPLICATIONS

Cycle/year XXVII/2012

VIBRATIONAL SPECTROSCOPY STUDY OF POLYMER-BASED COMPOSITE MEMBRANES FOR FUEL CELL APPLICATIONS

FIS 01 - EXPERIMENTAL PHYSICS

COORDINATOR: Prof. Adolfo Speghini
TUTOR: Prof. Gino Mariotto

DOCTORAL CANDIDATE: Valentina Allodi

Contents

Introduction

The research on new energy solutions is nowadays a key point in order to develop a sustainable society. Great efforts have been made in the last years on the improvement and commercialization of alternative energy systems, like solar cells, wind turbines, geothermal well, bio-fuels and hydrogen. In this view, fuel cells represent a promising system for a clean and efficient power generation, based on the conversion of the hydrogen chemical energy into electricity through a chemical reaction, with pure water as waste emission.
Among the various type of fuel cells, proton exchange membrane fuel cells (PEMFC) are particularly promising for automotive applications due to their low start-up time and low working temperature, but are still affected by issues that limit their diffusion on the market, like the sharp decay of proton conductivity of one of the main component, the proton conductive membrane, at high temperature ($T > 100$ °C) and low humidity conditions. An attractive strategy explored in order to obtain membranes with better performances is the incorporation into the host polymer matrix of inorganic acidic materials, able to increase the system water retention and at the same time the total number of acidic sites. Until now a large variety of different filler and membranes materials have been studied in literature, usually with promising results in terms of membrane performances under critical conditions. However, to optimize and properly tailor these systems a deeper understanding of their structure and operation mechanism is required and experimental techniques like Raman and infrared spectroscopy represent a valuable tool to clarify the effects of the filler incorporation on the membrane structure and properties. The specific aim of the present thesis is to carry out a systematic Raman and infrared analyses on different composite membranes containing nanosized fillers.
To introduce the studied systems, in the first chapter of the thesis the fuel cell working principles are presented, together with the description of the main type of fuel cell systems currently under study. Special attention is given to the proton exchange membrane fuel cells, in particular to their components, strengths and problems. In chapter 2, Raman and infrared spectroscopy theories and experimental details are presented. The experimental part is divided

between chapter 3, 4 and 5. In total, two different polymer matrices and five nano-fillers are studied: in chapter 3 a system composed by SnO_2 (with and without sulfate functionalization) and Nafion is analysed, in chapter 4 the results on sulfated TiO_2 included in Nafion at different weight percentage (2, 5 and 7 %) are presented and finally pure and propyl sulfonate TiO_2 included in SPEEK are studied in chapter 5. For all the systems, the fillers vibrational properties, their effective inclusion into the membranes as well as the effect that the inclusion has on both fillers and polymers have been studied with micro-Raman and infrared spectroscopy. Furthermore, on the Nafion-based systems, a Raman analysis on the inner environment of the composite polymers carried out at different ambient relative humidities and temperatures, never performed before on composite membranes, coupled with infrared and water uptake results, provides deeper insights about the complex behaviour of these composite systems.

Chapter 1

Proton Exchange Electrolyte Fuel Cell

1.1 Why fuel cells?

Fuel cells, due to their high efficiencies and low emissions, have recently received much attention due to the growing concerns on the climate change and the depletion of petroleum-based energy resources. In fact, a fuel cell efficiency can reach over 60 % in electrical energy conversion and a reduction in major pollutants over 90 % [1].
Generally, a fuel cell is an electrochemical devices that directly convert chemical energy (stored in fuels) into electrical energy and heat. In addition to Hydrogen, a large variety of fuels can be used to generate electrical energy, giving the possibility to efficiently employ different energy sources.
Up to now, five categories of fuel cells have received major research efforts:

- **Phosphoric Acid Fuel Cells (PAFCs)**: characterized for the use as electrolyte of liquid phosphoric acid in a bonded silicon carbide matrix and of finely dispersed platinum catalyst on carbon for electrodes.
  The charge transfer inside the cell is due to a flux of hydrogen ions from anode to cathode. This type of fuel cell operates at around 180 °C, is quite resistant to poisoning by carbon monoxide, but has a low electrical efficiency.
- **Solid Oxide Fuel Cells (SOFCs)**: they have solid ceramic, such as stabilized zirconium, as electrolyte. The charge transfer inside the cell is due to a flux of oxygen ions from cathode to anode. Due to the not-acid environment, a precious metal catalyst is not necessary. They can run on hydrocarbon fuels such as methane and due to the high working temperature (800 °C - 1000 °C) usually they run continuously.
- **Molten Carbonate Fuel Cells (MCFCs)**: characterized by the presence

of molten carbonate salt suspended in a porous ceramic matrix as electrolyte and a flux of carbonate ions from cathode to anode. A precious metal catalyst is not required due to the not-acid environment. They can run on hydrocarbon fuels and operate at about 650 °C. Due to the high working temperature they usually run continuously.

- **Alkaline Fuel Cells (AFCs)**: so called for the use of an alkaline solution, i.e. potassium hydroxide in water, as electrolyte. The charge transfer inside the cell is due to a flux of hydroxide ions from cathode to anode. They are very sensitive to poisoning, and are generally fuelled with pure hydrogen and oxygen. Working temperature of AFCs is about 70 °C.
- **Polymer Electrolyte Membrane (PEM) Fuel Cells (or PEMFCs)**: better described in section 1.2, are also called Proton Exchange Membrane fuel cell, and are characterized by an acidic polymer membrane as electrolyte and a flux of hydrogen ions. Platinum based catalyst are generally present on both electrodes. They operate at low temperature (below 100 °C). An important PEM sub-category is represented by Direct Methanol Fuel Cells (DMFC), that use methanol instead of hydrogen as fuel.

1.2 PEM fuel cell

Among the different type of fuel cells, PEMs are characterized by high power density, rapid response to varying load, relatively quick start-up and low operating temperatures. All these features make PEMFCs a promising candidate as the next generation power sources for stationary and portable applications, in particular for vehicle technology [2, 3]. By now most of the major motor companies are studying PEM fuel cells, and some fuel cell vehicles have already been developed, like, for instance, the General Motor HydroGen4, the Ford Focus FCV, the Honda FCEV and others [4]. Almost all of this car models are in an advanced phase of development, with expected commercial availability in the next years. Moreover, Hyundai is currently offering in leasing the Hyundai Tucson fuel cell in Southern California, an offer that will be expanded to other regions as fuelling infrastructure becomes available [5]. Other than in vehicle technology, PEMFC are now used like backup powers, e. g. Ballard FCgen 1020 [6], and portable and residential power supply.
Historically, PEM fuel cells gained prominence in 1959 after the incorporation of an ion-exchange resin as electrolyte by General Electric [7], and the employment of the obtained fuel cell for the Gemini space mission in 1962. A fundamental improvement in PEM technology was then made in the 1970s,

with the adoption of the fluorinated Nafion polymer as the membrane material. However, it was only a couple of decades ago that PEM fuel cell technol-

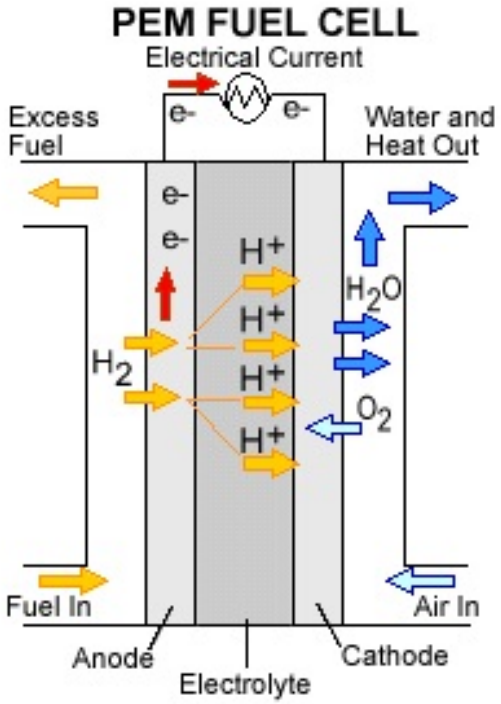

Figure 1.1: PEM fuel cell working scheme, from [8]

ogy gained the industrial attention, with the outcomes of new methods for reducing the amount of platinum required. In particular Raistrick's patent in 1989 [9] and the 1993 patent by Wilson [10], with the invention of the catalyst ink technique for the electrodes fabrication, gave the possibility to reduce the amount of platinum metal needed and at the same time to increase the utilization of the active catalyst.
Today PEMFC can be divided into two main categories: the so called classical PEM fuel cell and the Direct Methanol Fuel Cell (DMFC). Both use a proton exchange fuel cell as electrolyte, but while classical PEM are fuelled by hydrogen, DMFC use methanol. This difference means that the waste from a DMFC is not only pure water but also carbon dioxide, and that other technological problems are involved with respect to classical PEM due to the presence of methanol, like membrane methanol permeation and methanol electro-oxidation. A great advantage is, of course, the easier transport and storage of fuel as compared to the pure hydrogen fuel cell. Since the present thesis work is done on membranes for classical PEMs, and the eventual effect

of the inclusion of these membrane on DMFC will be not discussed, so only the first PEM type will be described in details.
Figure 1.1 represents a classical PEMFC working scheme: hydrogen is fed to the PEM anode where a catalyst separates electrons from protons. The electrolyte membrane does not conduct electrons, so that they must travel outside it via an electrical circuit to reach the other side of the cell, generating an electrical current. At the cathode oxygen combines with electrons and protons, giving water as a product. The half-cell reactions taking place in a PEMFC are:

$$Anode : H_2 \longleftrightarrow 2H^+ + 2e^-$$

$$Cathode : \frac{1}{2}O_2 + 2H^+ + 2e^- \longleftrightarrow H_2O$$

$$Overall : H_2 + \frac{1}{2}O_2 \longleftrightarrow H_2O$$

According to the fundamental structure, a single PEMFC could be divided into different components: *current collectors*, *seals* (gasket), *flow fields* and the *membrane-electrode assembly* (MEA). The MEA, the fuel cell core, is in turn composed by two *electrodes* and the *proton exchange membrane* in between (Figure 1.2). All the cell components are sandwiched between two *end plates* that enable the sealing of the different components by compression.

Furthermore, the two metallic current collectors are the fuel cell connec-

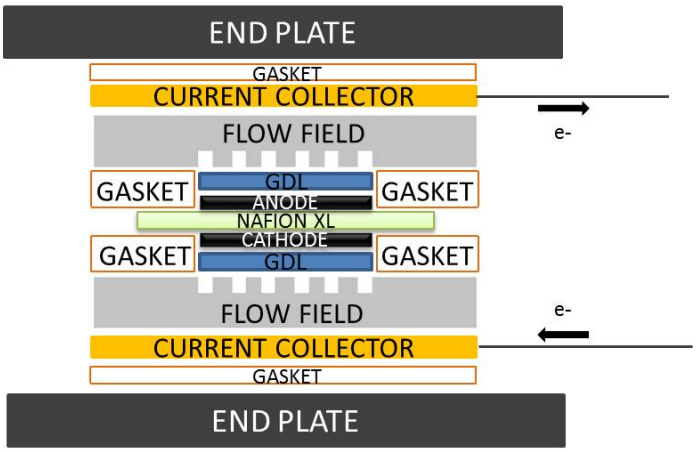

Figure 1.2: PEM fuel cell main components.

tion with the outer electrical circuit. The gaskets are both current insulator, to avoid short circuit, and seals. The two flow field plates, usually made on graphite for laboratory use, have a flow channel conveniently carved on one of the surfaces. Through this channel the reactant gases reaches the fuel cell electrodes, and because only the MEA in direct contact with the reagent will

work properly, different channel designs have been studied in order to increase the gas-electrode contact without effecting the current conduction and the heat dissipation.
All these fuel cell parts are supportive components designed to assure the best gas flux, water and heat dissipation and electrical connection at the MEA, where the electrochemical process takes part.
Electrodes and PEM are the components of the so called MEA. Together with PEMs, electrodes are the most studied fuel cell components, because of their high impact on the total fuel cell cost. In fact, the large amount of Platinum needed in original fuel cells was one of the reasons of their initial exclusion from commercialization, and the reduction of the Pt loading is still a current topic in fuel cells research. Researchers who work on electrodes deal with fuel cell components that, to be effective, need to correctly balances the transport processes required for fuel cell operation: transport of protons from the membrane to the catalyst, of electrons from the current collector to the catalyst and of the reactant and product gases to and from the catalyst layer and the gas channels.
The electrodes can be divided into two main parts, each one with different functions: the gas diffusion layer (GDL) and the catalyst layer (Figure 1.3).
The gas diffusion layer is necessary to sustain the thin catalyst layer and to

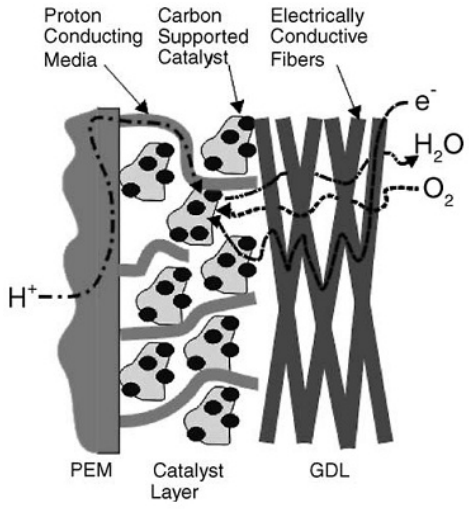

Figure 1.3: PEM fuel cell: electrode structure, from [11]

enhance the MEA zone reachable by gases. It is inserted between the flow field and the catalyst layer and has a thickness in the range from 100 to 300 μm: it is usually made of microporous carbon paper or carbon cloth with a mixture of carbon black and PTFE. Carbon paper or cloth is needed for the

structural strength and to assure the electron conduction. The role of PTFE, due to its hydrophobic structure, is to prevent the electrode flooding (especially at the cathode where water is produced) and to force water to move away toward the gas flow channels [12]. GDL properties are strongly dependent on the level of compression: usually the proper final layer thickness is around 70% - 80% of the initial value. To reach the GDL desired compression the thickness of the gasket around the GDL-electrode zone is properly chosen in order to obtain the right GDL final thickness when the fuel cell is closed by the end plates.

The catalyst layer, also referred to as the active layer, is the location of the half-cell reactions in a PEM fuel cell. Its function is to support the catalyst particles, made of Pt or Pt-alloys, in close contact with the membrane. The first generation of PEM fuel cell had Pt black as electrocatalyst, usually with a loading of 4 mg_{Pt}/cm^2, characterized by long lifetime but with prohibitive cost. A great effort in research was done in reducing Pt loading below 0.4 mg_{Pt}/cm^2, mainly by developing methods to increase the utilization of the deposited platinum [11], but work has still to be done.

Gasteiger et Al. [13] fixed a Pt loading in MEA to ca. 0.15 mg_Pt/cm^2 in order to sustain a large- scale automotive application. To reach this goal both cathode and anode Pt loading have still to be reduced, but while lowering the Pt-loading for anode electrodes even down to 0.05 mg_{Pt}/cm^2 is simple due to the large activity of Pt toward the H_2 oxidation reaction (HOR), a lowering of cathode loadings below 0.4 mg_{Pt}/cm^2 is much more difficult due to the poor activity of Pt for the oxygen reduction reaction (ORR). Two main ways to further decrease the Pt loading are the optimization of electrode structures and the implementation of more active Pt- alloy catalysts. Some Pt-alloys (like PtCr, PtV, PtTi and others) have already shown a higher catalyst activity than pure Pt, with lower costs, but with a higher risk of PEM contamination due to the leaching of non-noble base elements incorporated in the alloy (possible for example for the intrinsic base-metal thermodynamical instability under PEMFC potential in acidic electrolytes).

As for cheaper Platinum-free catalyst, which can be used in higher quantity to compensate the lower activity, PEM acidic environment rules out all particles of non-metals and most of the oxides. A limited success was achieved with transition metal ion stabilized by several nitrogen bound in a graphite-like or aromatic carbon structure, but the durability of these systems is still under investigation [14].

1.3 Polymer electrolyte membranes

The development of commercial ion-conducting polymer electrolytes deeply changed the field of electrochemical devices. In fact, the variety of available polymers gives the possibility to choose a material with the ideal conductivity for a precise ion and the stability needed for the desired application. Moreover, polymeric electrolytes does not have the extreme corrosivity and confinement problems of traditional electrolyte systems like sulfuric acid and potassium hydroxide [15].
As for fuel cells, researchers were engaged in developing organic ion-exchange membranes for this application already in the 40's. The currently most used proton exchange membrane, Nafion, was developed in the late 60's by Du Pont researchers, even if its first use was for perm-selective separator in chloro-alkaly electrolyzers. During the next decades a wide number of PEMs were developed, both poly(perfluorosulfonic acid) membranes like Nafion or with a different chemical structure, like the cheaper but less chemically resistant hydrocarbon polymers [16].
All proton exchange membranes have to fulfil some important properties: they must have a high ionic conductivity with little electronic component and they must be stable in oxidizing and reducing environments due to their role as physical separator for the fuel and oxidant. In addition, the electrolyte must be both mechanically and electrically robust to endure the start-up and shut down procedure, should have the capability for fabrication into membrane electrode assemblies and have a low water transport through diffusion and electro-osmosis [17, 18].
Based on the chemical species, proton exchanging membranes can be divided in 6 main categories:

- **Poly(perfluorosulfonic acid) based membranes**: like Du Pont Nafion, are composed by a fluorinated backbone like PTFE, a fluorocarbon side chain and ionic clusters consisting of sulfonic acid ions attached to the side chains. Other than Nafion®, two examples are Flemion, produced by Asahi Glass and Aciplex-S, produced by Asahi Chemical.
- **Styrene-based membranes**: styrene polymer are easy to synthesize, but if the polymer is not fluorinated the oxidative stability is low. Examples are BAM from Ballard and sulfonated styrene - ethylene - butylene - styrene (SEBS) from Dain Analytic's [19].
- **Poly(arylene ether)s based membranes**: wholly aromatic polymers, have high thermal and chemical resistance [20, 21]. However, the proton conductivity is less at low relative humidity than in Nafion. One example is Sulfonated Poly(Ether Ether Kethone) (SPEEK).
- **Poly(imide)s based membrane**s: five-membered ring polyimides are

high performance material, but with a tendency to fast degradation in water. Six-membered ring are more stable, but still suffers from hydrolysis stability problems. Branching and cross-linking seems to improve oxidative stability and mechanical strength [22, 23].

- **Polyphosphazene based membranes**: characterized by good thermal and chemical stability and an easy addition of various side chain for ion exchange sites. However, their low glass transition temperatures cause poor mechanical properties.
- **polybenzimidazole (PBI)**: if the imidazole hydrogen is replaced by a sulfonated group, PBI can be used as backbone of sulfonated polymers conducting protons in the hydrated state. They have good ion exchange capacity but low water uptake and no data on the temperature dependence of the swelling have been published until now. Moreover, they present a low proton conductivity. Not modified PBI are used instead as high temperature membranes: the polymer, due to the basic nature of benzimidazole group, can absorb polyvalent oxoacids (like sulfuric and phosphoric acid) and proton conduction can occur without water [24]. In this case, problems arises when acid is diluted by water and from the absorption of phosphoric acid on platinum surfaces.

Apart from polybenzimidazole, that rely on protonation of benzimidazole groups for proton conduction, all the other kinds of PEMs listed above usually rely on sulfonic acid as proton conducting moiety. Recently also new proton conductors groups have been investigated, and one promising alternative to sulfonic acid is represented by phosphonic-based polymers. These membranes shows lower acidity than sulfonic acid ones but have better chemical and thermal stability compared to the corresponding sulfonic acid-functionalized polymers [25, 26].
Among the different type of membranes here described, this thesis work is focused on the characterization of Nafion composite membranes and SPEEK composite membranes, so a more detailed description of these two polymers will be presented in the next sections.

1.3.1 Nafion

Nafion is a copolymer of perfluoro-sulfonic acid characterized by hydrophobic fluorocarbon backchains and hydrophilic sidechains with terminal sulfonic acid groups. Its chemical structure is represented in Figure 1.4.
Nafion is obtained by copolymerization of variable amounts of unsaturated perfluoroalkyl sulfonyl fluoride (PSEPVE) with tetrafluoroethylene (TFE).

It is commercially available in different equivalent weights (grams of dry

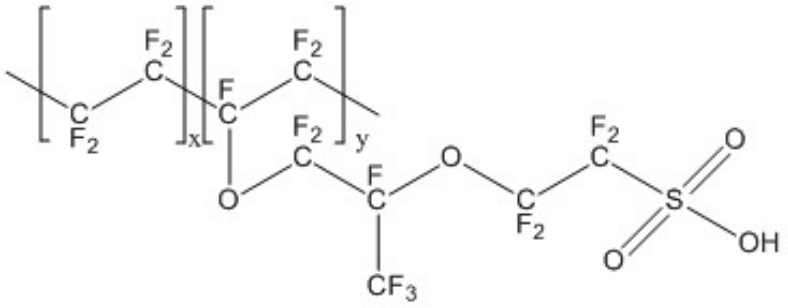

Figure 1.4: Nafion chemical structure

polymer per mole of sulfonic acid groups): a higher percentage of sulfonic group resulted in an increased proton conduction but, on the other hand, also the membrane swelling in water is increased and the mechanical properties are poorer. A good balance between these effects is obtained in Nafion-117 (EW 1100), which in fact is the most used one.
The main problem of Nafion is represented by its production costs. Currently, 1 Kg of polymer costs around 5000 dollars (compared to 10 dollars/Kg for PTFE). This is due to the high cost of manufacture (high cost of monomers, materials dangerous to handle) and to the small market volume. As for automotive application, *Mathias et al.* conducted a study in which they calculated that the membrane cost will drop down to less than 200 dollars/Kg with 1 million car produced per year, a price not prohibitive for automotive application [27]. Based on this analysis, it seems that Nafion-based fuel cell could reach reasonable prices, and the use of Nafion membrane would not completely prevent the PEMFC from being cost competitive with internal combustion engine [15].
In the last forty years a wide number of studies on Nafion have been reported with the aim to analyze the material chemical microstructure and nanoscale morphology. As a matter of fact a deep knowledge of the material structure is mandatory to rationally design the membrane and obtain the optimum performances in terms of proton conductivity, water management, hydration stability at high temperatures, electro-osmotic drag, and, finally, mechanical, thermal, and oxidative stability.
Morphological characterizations using X-rays and neutrons, like small-angle scattering techniques, give data that are, unfortunately, not easy to interpret. Due to this difficulty, different models for Nafion structure have been proposed over the years to explain the experimental data.
One of the first model proposed was the cluster-network model of Gierke [29, 30], based on small-angle X-ray scattering (SAXS) studies. This model

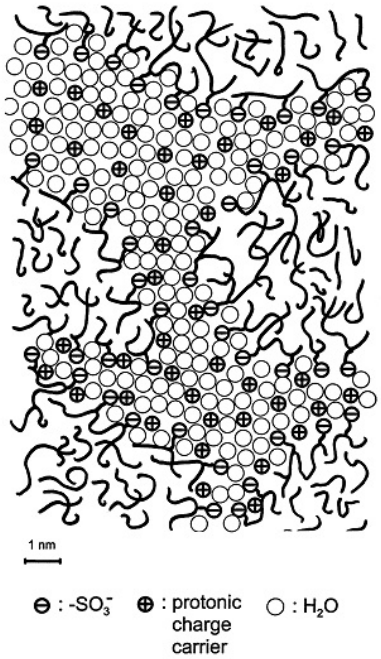

Figure 1.5: Schematic representation of the microstructures of Nafion (derived from SAXS experiments). From [28]

assumes the existence of 40 Å -in-diameter clusters of sulfonate-ended perfluoroalkyl ether groups that are organized as inverted micelles connected by pores that are 10 Å in size.
In the following years, a wide number of other possible structures have been proposed: almost all recognize the existence of ionic groups aggregate in the perfluorinated polymer matrix to form a network of clusters that can be significantly swelled by polar solvents and allow an efficient ionic transport. The main differences between the different model are in the geometry and spatial distribution of the ionic clusters.
More recent SAXS and NMR measurements [28] have given a consistent parametrization for a simple model of Nafion microstructure where water and ion containing domains are channel surrounded by the polymeric material. A pictorial view of this proposed structure is visible in Figure 1.5.
Even if the precise Nafion microstructure is still not completely sure, some basic characteristic are almost universally accepted by now: structural and thermal stability are provided by the PTFE backbone and it is within the hydrophilic domain that proton and water transport occurs. The membrane can thus be divided into three different zones: the fluorocarbon region, the interfacial region, consisting of side chains with solvated sulphonate groups, and the pores central zone, composed by ”bulk-like” water.

It is a matter of fact that Nafion conductivity sharply decrease with lower

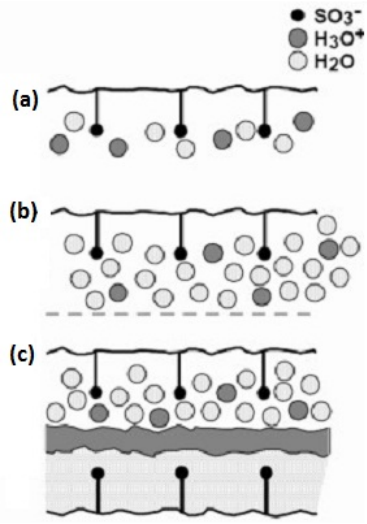

Figure 1.6: Qualitative picture of Nafion environment with different hydration: a) low water content (proton transport along the polymer surface), b) medium water content (interfacial water start to screen sulfonate ions, c) high water content (Grotthus mechanism). From [18]

water content, a complication for the use of Nafion in fuel cells. For this reason, a great effort was made to find theoretical models for ions transport in Nafion and to understand the role of water in the mechanism of proton conduction. One of the most famous model was proposed by Eikerling et al. in 2001 [31, 32], in which they distinguished two different mechanism of proton transports inside a Nafion pore: bulk transport and surface transport. In the pores bulk the mechanism is similar to the proton transport in pure water, in which an 'excess' proton or protonic defect diffuses through the hydrogen bond network of water molecules through the formation or cleavage of covalent bonds (Grotthus mechanism [33]). On the other hand, on the polymer surface, protons hop along the array of SO_3^- ions (surface hopping), but because of the distance between the ionic groups (0.6-1.2 nm) too large to allow a direct movement of the protons from one SO_3^- to the next, these must hop via intermediate water molecules. This protons transport is characterized by a higher activation energy (and thus lower mobility) due to the strong electrostatic interaction between protons and sulfonate ions [34].
The difference in proton conductivity between dry and wet membrane can thus be explained: as the membrane adsorbs more water the size of the pores increases with a consequent increase in bulk-like portion of water and a higher conductivity. The different environments are described in Figure 1.6: at

low hydration (a) hydronium ions move along the polymer surface, then with increasing water content (b) water in interfacial region screens weakly bounded water from ion-dipole interactions and finally, with high water content (c) water and proton move more freely, with an environment more similar to pure water.
This model is validated also by the comparation of water self-diffusion coefficient (obtained by pulsed-field-gradient NMR) and proton diffusion (obtained from conductivity data): the diffusion rates diverge with increasing water content, revealing a predominant Grotthus type hopping at higher hydration and an increasingly decoupled transport of water and protons as the membrane gains more water [35].

1.3.2 SPEEK

Even if it seems possible to create cost competitive fuel cells with Nafion [27, 15], the use of cheaper alternative membranes still presents great advantages. For example, a low price with low scale of production (under the

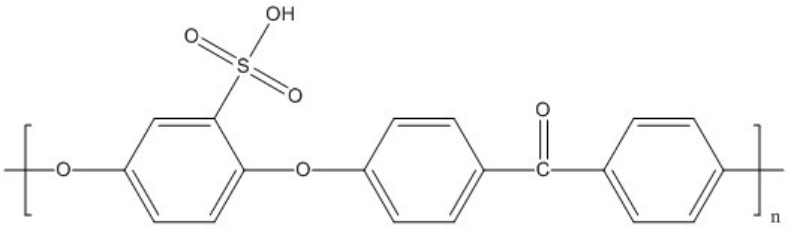

Figure 1.7: SPEEK chemical structure

production volume of 1 million car per year fixed as a good point for decisive manufacture price reduction for Nafion) will be a great incentive for fuel cell technology, giving to it the opportunity to conquer new market position in the near future.
Sulfonated Poly(Ether Ether Kethone) is one of the possible substitutes. Like Nafion, is a sulfonic acid based ionomer, but its backchain is composed by aromatic rings (Figure 1.7).
Compared with Nafion, SPEEK has a lower hydrophobic/hydrophilic distinction, and a less flexible backbone. These characteristics cause to the polymer a less pronounced separation into hydrophobic and hydrophilic domains, confirmed by SAXS experiments. SPEEK microstructure is sketched in Figure 1.8: the water filled channel are narrower and there are more dead-end "pockets" than in perfluorosulfonic membranes [28].
Even if SPEEK is an effective solution in terms of cost, and as a high structure stability, there are still some downsides that limit its utilization. For example,

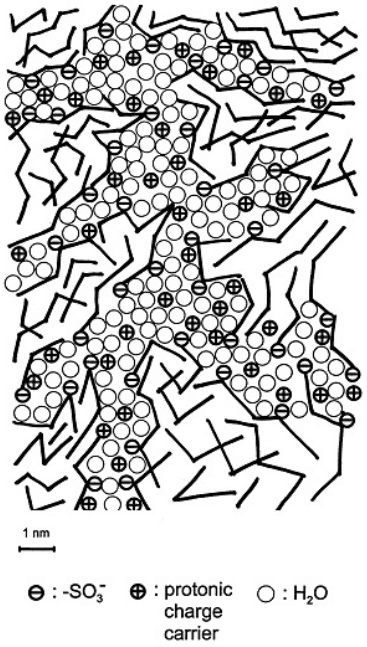

Figure 1.8: Schematic representation of the microstructures of a sulfonated polyetherketone (derived from SAXS experiments). From [28]

although the hydration behaviour is quite similar to Nafion, a great difference is observed in swelling: while exaggerated swelling in liquid water begins at temperatures above 130°C for Nafion, this occurs at significantly lower temperature for SPEEK [36]. Moreover, SPEEK has a lower acidity compared to Nafion (PK_a approximately -1, while for Nafion is -6) and a weak dieletric screening of the negative charge of the sulfonate ions, which caused a strong decrease in proton diffusion compared to water diffusion with decreasing hydration. This proton localization effect, and the tortuous polymer microstructure, cause a strong decrease in proton conduction with low water content, higher that the one observed with Nafion [37]. It is thus clear that to represent a valid alternative to Nafion, this polymer is still to be optimized.

1.3.3 Composite membranes

Both Nafion and SPEEK relay on water molecules as mobile phase for proton conduction. The necessity of a high hydration level (10-30 water molecules per conducting moieties) implies a sharp decrease in proton conduction at low relative humidity and working temperatures above 100 °C. Improving the membranes behaviour at critical condition (high temperature, low RH) will cut the fuel cells cost and increase the durability, due to:

- **lower catalyst susceptibility to poisoning**: catalyst poisoning has been shown to be very dependent on the temperature, and at 80°C (the typical PEMFC working temperature), also a CO content of only 20 ppm can significantly decrease the fuel cell performance, meaning that only very pure hydrogen can be used as fuel[38].
- **simplified water managements**: the necessity of high hydration level implies a careful management of the water and thermal balance, to avoid dehydration or electrodes flooding. Moreover, for a high temperature operation, a high water vapour pressure is needed, which means also a high total pressure in order to have enough partial pressure of reactant gas. As an example, to keep a reactant partial pressure of 0,5 atm at 150°C with a 90 % relative humidity a system pressurization of at least 8 atm is required [38].
- **simplified thermal balance**: a PEMFC operating at 80 °C produces a large amount of heat that need to be removed in order to keep the desired working temperature.

Due to all the listed benefits, a great effort was made in order to synthesize membranes that can maintain a high proton conductivity even at critical conditions.
One of the preferred approach to improve the characteristic of known ionomeric membranes is the dispersion of low solubility acids (e. g. heteropolyacids) or particles of insoluble solids inside the polymer matrix. Among the solids particles, ceramic fillers (usually metal oxides) such as SiO_2, TiO_2, ZrO_2 and zeolite have been widely used to facilitate proton conduction in critical conditions due to the hygroscopicity of these composites, useful to increase the membrane water retention, and to their high stability [39, 40, 41, 42, 43].
To properly tailor the properties of a composite membranes with solid fillers, is important to keep in mind that the compound behaviour will not only depends on the nature of the ionomer and of the powder added, but also on the size and the amount of the dispersed particles. For example, a high interface interaction between the filler and the polymer cause a higher influence of the dispersed particles on the original polymer characteristics [44]. Due to this, usually nano-particles, with a high specific surface, have a greater effect on membrane properties compared to micro-particles.
Different methods were used to add nanocomposites to the polymer matrix: a commonly used technique is based on the impregnation of the ionomers solution with the inorganic oxide particles as fine powders, another way consists instead on the inclusion into the ionomeric solution of a precursor, generally an acidic metal alkoxides solution and the subsequent conversion of the precursor material into the desired oxide.
The inclusion of pure metal oxide has a beneficial effect on the water reten-

tion, but can have some downsides: due to the lower intrinsic proton conductivity of the oxide, compared to the membrane one, sometime the overall membrane conduction decreases with the filler inclusion. This mainly happen at high filler quantity, when the oxide beneficial water retention effect is exceeded by the negative effect caused by the lower filler conductivity. To avoid this, in the last years a new class of fillers have been developed: sulfate-supported metal oxides. These fillers in fact combine the hygroscopicity of the metal oxide with the proton conduction properties of superacid systems. According to Gillespie's definition [45], any acid can be called a superacid when its acidity is higher then that of pure H_2SO_4. Usually these acidity values are reached by mixing a fluorine- containing Brönsted acid and a fluorinated Lewis acid, but also other system were discovered. In sulfated metal oxide the superacidity is due to the change of acidity on the oxide surface after the addition of SO_4^{2-} ions. It's important to point out that not all metal oxides become superacid after the sulfate addition: MgO, CaO, CuO, NiO ZnO and others didn't show any acidity improvement, while an acidity strength increase was observed for TiO_2 ,ZrO_2, SnO_2 and SiO_2 [46]. The sulfate effect on the oxide surface that allows the superacidity condition is illustrated in Figure 1.9: the inductive effect of S=O in the complex increase the Lewis acidity of the metal ion, and when water molecules are present the Lewis acid sites are converted into Brönsted acid sites [47].

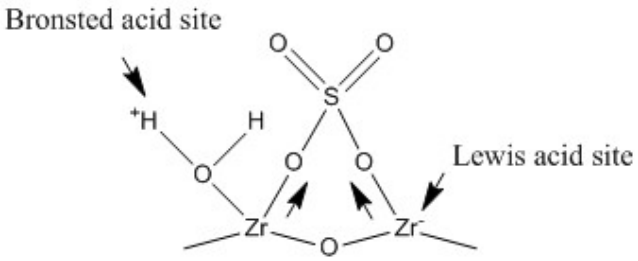

Figure 1.9: Brönsted and Lewis acid sites in metal oxide superacids

The increased proton conductivity of these systems with respect to simple metal oxides is due to the presence of these sites: Brönsted acids sites increase the ion exchange capacity of the filler (due to the higher number of H^+ created) and provide additional proton hopping sites, fundamental for proton conduction.
In the next section two solid oxides, used as membrane fillers in the present thesis work, will be described more in details.

1.3.4 Oxide fillers

1.3.4.1 Tin dioxide

Two forms of tin oxides are generally known: stannic oxide, also called tin dioxide (SnO_2) and stannous oxide, or tin monoxide (SnO). The presence of two different oxides reflects the dual valency of tin, that can exists in two oxidation states: +2 and +4. The two tin oxides crystal structures are different: SnO, if crystallize at ambient condition, possesses a litharge structure (other structures are typical of different conditions, like the so-called γ-SnO [48]), while SnO_2 has a rutile structure. Among the two, the stannic oxide is the thermodynamically most stable form, and at elevated temperature SnO react to give Sn + SnO_2 [49]. Stannic oxide has been deeply studied because it is the more abundant form of tin oxide and is the one of technological significance: it is widely used, and up to now it has been employed in optoelectronic as conductive transparent oxide, in chemistry as oxidation catalyst and as solid state sensor for gases[50].
Among the various technological application, SnO_2 has been used as filler in PEM fuel cell: due to its hygroscopic behaviour, the relatively high proton conductivity when in hydrate form ($SnO_2 \cdot H_2O$), and its thermal stability, it represent a good choice to improve the membrane behaviour at higher temperature and low ambient humidity.
SnO_2 was included in Nafion by Chen et al. [51] with good results in term of proton conductivity at high temperature (if the inclusion remained under the 10 %) and methanol permeability.
Also other kind of proton conducting membrane have shown better performances with SnO_2 addition. For example, $SnO_2 \cdot H_2O$ was successfully incorporated in sulfonated polysulfone membranes, increasing the proton conductivity at low hydration level due to an enhancement in hydrophilic domain interconnections [52]. Mecheri et al. have studied the effect of SnO_2 inclusion into SPEEK for DMFC, finding a higher proton conductivity, a decrease in methanol permeability and an increase in membrane stability [53]. In a following paper, the authors investigated the SPEEK conduction mechanism with and without the filler, finding a decrease in the tortuosity of proton transport due to the filler presence but not a corresponding decrease in the tortuosity of the water diffusion, and concluding that a non-vehicular proton bridge mechanism was caused by the tin oxide [54].
As already mentioned, a successful way to further increase membranes performances is to add not simple metal oxides but sulfated metal oxides. In the same paper where Nafion +SnO_2 was investigated for DMFC applications, Chen et al. [51] also studied a Nafion + sulfate SnO_2 membrane: the membranes showed better performances than simple Nafion and Nafion +

pure SnO_2 in both ex situ proton conductivity, methanol crossover and fuel cell power density. The same system for standard H_2-O_2 fuel cell has not been studied yet, and this was the aim of the work at which the spectroscopic study reported in chapter 3 belongs to.

1.3.4.2 Titanium dioxide

Tin dioxide, also called titania, is a material with a large number of applications in various fields. For example, it is used as a pigment, as a catalyst, in electronics, electrochemical and ceramic industries and also in pharmaceutical and food products. Among its numerous strengths are the non-toxicity, the high thermal stability and the biological and chemical inertia [55]. Titania exists in a multiplicity of polymorphs, each one with different properties. In nature, TiO_2 can occur in four different structures: in fact, at the three well known natural forms of titanium dioxide, namely rutile (the stable form under ambient condition), anatase and brookite, was more recently added a fourth one by Banfield et al., named TiO_2-B [56]. In addition to these forms, titania has been synthesised in laboratories in other seven structure until now. Due to its hygroscopicity, TiO_2 is a promising candidate for the inclusion in polymer electrolyte membranes in order to increase the membranes water retention. Due to this, during the last decade, a lot of studies have been published in which TiO_2 has been used as filler for fuel cell membranes. Watanabe et al. were among the first to add titania to Nafion, first together with Pt nanopowders [57] and then alone [39]. In both cases an increased water uptake and better performances of the fuel cells were observed, especially when they were fed with dry gases.
Different methods for the oxide inclusion have been reported, even if the most used is the so-called cast process, in which as first the nanopowder is added to the polymeric solution, then the mixture is cast on a Petri dish and finally dried and hot-pressed to obtain the composite membrane. Different TiO_2 synthesis route have been tested as well. Notwithstanding the differences in filler synthesis and inclusion, all the works published up to now reported a general improvement in the fuel cells performances after the titania inclusion in Nafion, especially at low relative humidity and high temperature [58]. An interesting study by Baglio et al. analysed the effect of the titania phase on the performances of a Nafion composite membrane for DMFC, finding no particular differences in the fuel cells electrical properties when the nanoparticles surface area is similar. This suggests that the particles surface, and not the bulk, is the real key parameter in the composite membranes synthesis[59].
As stated above for tin dioxide, a good way to further increase the compos-

ite membranes performances is to functionalize the filler in order to have more acid sites in the composite system, which means an increased number of charge carriers and additional proton hopping sites. Among the various functionalizations, the addition of sulfate groups to titania is an already known method to obtain a powder with high acidity values, even reaching superacidity. This procedure was in fact already adopted for the creation of superacid titania catalyst, used for example for the photocatalytic degradation of organic pollutants [60]. Sakai et al. performed a study on sulfate titanium oxide in view of a future inclusion into electrolyte membranes, finding a powder proton conductivity similar or even higher than the Nafion's [61]. Until now only one work, published by Wu et al., reported the effect of the addition of sulfate titania into Nafion, and the composite membrane subsequent employment in direct methanol fuel cells. In this case the final effects of the filler inclusion were not all good: together with a positive reduced methanol crossover in fact a negative reduced proton conduction and water uptake were reported for the composite membranes [62].
In the fourth chapter of this thesis the spectroscopic investigation of sulfated titania- Nafion system is reported. This analysis was part of a more complex work with the aim to better understand the Nafion-sulfate titania system, still not deeply analysed, and to verify the real effect of the filler on the membrane properties, with particular attention to the application for direct hydrogen fuel cells, a case never studied before.
The inclusion of Titania nanopowders was tried also in other protons conducting polymers, like SPEEK. Composite SPEEK-TiO_2 membranes with a significantly reduced swelling behavior and an increased proton conductivity were synthesized by different groups, like Di Vona et al. and Filho et al. [63, 64, 65] Also for the SPEEK case, a good idea to further increase the membrane performances is the functionalization of the titania in order to increase the total number of acid centers. One of the possible functionalized titania, studied with Raman and IR spectroscopies and described in chapter 5, is TiO_2RSO_3H nanopowder. The inclusion of this material in SPEEK membranes in fact increase the number of sulfonic group in the system avoiding the drawback of the increased membrane swelling experienced in SPEEK with high degree of sulfonation. Moreover, the presence of bifunctional branches, consisting of hydrophobic aliphatic chains with terminal hydrophilic groups, can ease the uniform filler dispersion in both the hydrophobic and hydrophilic domains of the polymer [66].

Bibliography

[1] D.Papageorgopoulos, "An introduction to the 2010 fuel cell pre solicitation workshop," 2010.

[2] V. Mehta and J. S. Cooper, "Review and analysis of pem fuel cell design and manufacturing," *Journal of Power Sources*, no. 114, pp. 32–53, 2003.

[3] Y. Wang, K. Chen, J. Mishler, S. C. Cho, and X. C. Adroher, "A review of polymer electrolyte membrane fuel cells: Technology, applications, and needs on fundamental research," *US Department of Energy Publications*, no. 132, 2011.

[4] Y. Wang, K. Chen, J. Mishler, S. Cho, and X. C. Adroher, "A review of polymer electrolyte membrane fuel cells: Technology, applications, and needs on fundamental research," *Applied Energy*, pp. 981–1007, 2011.

[5] "Hundai tucson fuel cell," 2014.

[6] "Fcgen -1020acs," 2014.

[7] B. Smitha, S. Sridhar, and A. Khan, "Solid polymer electrolyte membranes for fuel cell applications : a review," *Journal of Membrane Science*, no. 259, pp. 10–26, 2005.

[8] "Fct fuel cells: types of fuel cells," 2009.

[9] I. Raistrick, 1989.

[10] M. S. Wilson, 1993.

[11] S. Litster and G. McLean, "Pem fuel cell electrodes," *Journal of Power Sources*, no. 130, pp. 61–76, 2004.

[12] S. Revankar and P. Majumdar, *Fuel Cells: Principles, Design, and Analysis*. 2014.

[13] H. A. Gasteiger, S. S. Kocha, B. Sompalli, and F. T. Wagner, "Review activity benchmarks and requirements for pt, pt-alloy, and non-pt oxygen reduction catalysts for pemfcs," *Applied Catalysis B: Environmental*, no. 56, pp. 9–35, 2005.

[14] F. Jaouen, S. Marcotte, J. P. Dodelet, and G. Lindbergh, "Oxygen reduction catalysts for polymer electrolyte fuel cells from the pyrolysis of iron acetate adsorbed on various carbon supports," *J. Phys. Chem B*, no. 107, pp. 1376–1386, 2003.

[15] M.Doyle and G. Rajendran, "Perfluorinated membranes," in *Handbook of Fuel Cells - Fundamental, Technology and Applications, Volume 3* (W. Vielstich, H. A. Gasteiger, and A. Lamm, eds.), p. 351, Wiley and Sons, 2003.

[16] M. Rikukawa and K. Sanui, "Proton-conducting polymer electrolyte membranes based on hydrocarbon polymers," *Prog. Polym. Sci.*, no. 25, pp. 1463–1502, 2000.

[17] M. A. Hickner, H. Ghassemi, Y. S. Kim, B. R. Einsla, and J. E. McGrath, "Alternative polymer systems for proton exchange membranes (pems)," *Chem. Rev*, no. 104, pp. 4587–4612, 2004.

[18] A.K.Sahu, S. Pitchumani, P. Sridhar, and A. K. Shukla, "Nafion and modified-Nafion membranes for polymer electrolyte fuel cells: An overview," *Bull. Mater. Sci.*, no. 32, pp. 285–294, 2009.

[19] K. Miyatake and A. Hay, "Effect of equivalent weight on electrochemical mass transport properties of oxygen in proton exchange membranes based on sulfonated α, α, β -trifluorostyrene (bam) and sulfonated styrene-(ethylene-butylene)-styrene triblock (dais-analytical) copolymers," *J. Polym. Sci., Part A: Polym. Chem.*, no. 39, pp. 3770–3779, 2001.

[20] K. Miyatake, K. Oyaizu, E. Tsuchida., and A. S. Hay, "Synthesis and properties of novel sulfonated arylene ether/fluorinated alkane copolymers," *Macromolecules*, no. 34, pp. 2065–2071, 2001.

[21] K. Miyatake, Y. Chikashige, and M. Watanabe, "Novel sulfonated poly(arylene ether): A proton conductive polymer electrolyte designed for fuel cells," *Macromolecules*, no. 36, pp. 9691–9693, 2003.

[22] K. Miyatake, H. Zhou, and M. Watanabe, "Proton conductive polyimide electrolytes containing fluorenyl groups: Synthesis, properties, and branching effect," *Macromolecules*, no. 37, pp. 4956–4960, 2004.

[23] N. Asano, K. Miyatake, and M. Watanabe, "Hydrolytically stable polyimide ionomer for fuel cell applications," *Chem. Mater.*, no. 16, pp. 2841–2843, 2004.

[24] J. Wainright, M. H. Litt, and R. F. Savinell, "High-temperature membranes," in *Handbook of Fuel Cells - Fundamental, Technology and Applications, Volume 3* (W. Vielstich, H. A. Gasteiger, and A. Lamm, eds.), p. 436, Wiley and Sons, 2003.

[25] K. Miyatake and A. Hay, "Synthesis of novel phosphinic acid-containing polymers," no. 39, pp. 1854–1859, 2001.

[26] K. Miyatake and A. Hay, "New poly(aryleneether)s with pendant phosphonic acid groups," *J. Polym. Sci., Part A: Polym. Chem.*, no. 39, pp. 3770–3779, 2001.

[27] M. F. Mathias, R. Makharia, H. A. Gasteiger, J. J. Conley, T. J. Fuller, C. J. Gittleman, S. S. Kocha, D. P. Miller, C. K. Mittelsteadt, T. Xie, S. G. Yan, and P. T. Yu, "Two fuel cell cars in every garage?," *Interface*, pp. 24–35, 2005.

[28] M. Ise, *Polymer Elektrolyt Membranen: Untersuchungen zur Mikrostruktur und zu den Transporteigenschaften für Protonen und Wasser*. Ph.d. thesis, University of Stuttgart, 2000.

[29] T. Gierke and W. Y.Hsu, "Perfluorinated ionomer membranes," in *ACS Symposium Series No. 180* (A. Eisenberg and H. L. Yeager, eds.), p. 283, American Chemical Society, 1982.

[30] T. Gierke, G. E. Munn, and F. C. Wilson, "The morphology in nafion perfluorinated membrane products, as determined by wide- and small-angle x-ray studies," *J. Polym. Sci., Polym. Phys.*, no. 107, pp. 1687–1704, 1981.

[31] M. Eikerling, A. A. Kornyshev, A. M. Kuznetsov, J. Ulstrup, and S. Walbran, "Mechanisms of proton conductance in polymer electrolyte membranes," *J. Phys. Chem. B*, pp. 3646–3662, 2001.

[32] M. Eikerling and A. Kornyshev, "Proton transfer in a single pore of a polymer electrolyte membrane," *J. Electroanal. Chem.*, pp. 1–14, 2001.

[33] C. de Grotthuss, "Sur la décomposition de l'eau et des corps qu'elle tient en dissolution à l'aide de l'électricité galvanique," *Ann. Chim.*, pp. 54–73, 1806.

[34] P. Choi, N. H. Jalani, and R. Datta, "Thermodynamics and proton transport in Nafion ii. proton diffusion mechanisms and conductivity," *Journal of The Electrochemical Society*, no. 152, pp. E123–E130, 2005.

[35] T. A. Zawodzinski, M. Neeman, L. . Sillerud, and S. Cottesfeld, "Determination of water dlffusion coefficients in perfluorosulfonate ionomeric membranes," *J. Phys. Chem.*, pp. 6044–6044, 1991.

[36] K. D. Kreuer, "Hydrocarbon membranes," in *Handbook of Fuel Cells - Fundamental, Technology and Applications, Volume 3* (W. Vielstich, H. A. Gasteiger, and A. Lamm, eds.), p. 423, Wiley and Sons, 2003.

[37] K. Kreuer, "On the development of proton conducting polymer membranes for hydrogen and methanol fuel cells," *J. Membr. Science*, pp. 29–39, 2001.

[38] Q. Li, R. He, J. O. Jensen, and N. Bjerrum, "Approaches and recent development of polymer electrolyte membrane for fuel cell operating above 100°C," *Chem. Mater.*, pp. 4896–4915, 2003.

[39] M. Watanabe, H. Uchida, Y. Seki, and M. Emori, "Polymer electrolyte membranes incorporated with nanometer-size particles of pt and/or metal-oxides: Experimental analysis of the self-humidification and suppression of gas-crossover in fuel cells," *J. Phys. Chem B*, pp. 3129–3137, 1998.

[40] K. T. Adjemian, S. J. Lee, S. Srinivasan, J. Benziger, and A. B. Bocarsly, "Silicon oxide Nafion composite membranes for proton-exchange membrane fuel cell operation at 80-140 °C," *J. Electrochem. Soc.*, pp. A256–A261, 2002.

[41] D. Jung, S. Cho, D. Peck, D. Shin, and J. Kim, "Performance evaluation of a Nafion/silicon oxide hybrid membrane for direct methanol fuel cell," *J. Power Sources*, pp. 173–177, 2002.

[42] A. Arico, V. Baglio, A. D. Blasi, and V. Antonucci, "Ftir spectroscopic investigation of inorganic fillers for composite dmfc membranes," *Electrochem. Commun.*, pp. 862–866, 2003.

[43] A. Saccà, I. Gatto, A. Carbone, R. Pedicini, and E. Passalacqua, "ZrO_2 –Nafion composite membranes for polymer electrolyte fuel cells (pefcs) at intermediate temperature," *J. Power Sources*, pp. 47–51, 2006.

[44] G. Alberti and M. Casciola, "Composite membranes for medium-temperature pem fuel cells," *Annu. Rev. Mater. Res.*, pp. 129–154, 2003.

[45] R. J. Gillespie, "Fluorosulfuric acid and related superadd media," *Acc. Chem. Res.*, no. 1, pp. 202–209, 1968.

[46] M. Hino. Ph.d. thesis, Hokkaido Univ., 1982.

[47] K. Arata, "Solid superacids," *Adv. Cat.*, no. 37, pp. 165–211, 1990.

[48] Y. Li, Y. Li, L. Zhang, Y. Ma, and G. Zou, "The pressure-induced phase transition in SnO: a first-principles study," *J. Phys: Condens. Matter*, no. 19, p. 425230, 2007.

[49] D. Klushina, O. Nadinskaya, and K. Bogatina *Zh. Prikl. Khim.*, no. 79, p. 273, 1959.

[50] M. Batzill and U. Diebold, "The surface and materials science of tin oxide," *Progress in Surface Science*, no. 79, pp. 47–154, 2005.

[51] F.Chen, B. Mecheri, A. D'Epifanio, E. Traversa, and S. Licoccia, "Development of Nafion/tin oxide composite mea for dmfc applications," *Fuel Cells*, no. 10, pp. 790–797, 2010.

[52] B. Mecheri, V.Felice, A. D'Epifanio, A. Tavares, and S. Licoccia, "Composite polymer electrolytes for fuel cell applications: Filler-induced effect on water sorption and transport properties," *ChemPhysChem*, no. 16, pp. 3814–3821, 2013.

[53] B. Mecheri, A. D'Epifanio, E. Traversa, and S. Licoccia, "Sulfonated polyether ether ketona and hydrated tin oxide proton conductiong composites for direct methanol fuel cell applications," *J. Power Sour.*, no. 178, pp. 554–560, 2008.

[54] B. Mecheri, A. D'Epifanio, L. Pisani, F.Chen, E. Traversa, F. Weise, S. Greenbaum, and S. Licoccia, "Effect of a proton conducting filler on the physico-chemical properties of speek based membranes," *Fuel Cells*, no. 9, pp. 372–380, 2009.

[55] V. Swamy, J. Gale, and L. Dubrovinsky, "Atomistic simulation of the crystal structures and bulk moduli of TiO_2 polymorphs," *Journal of Physics and Chemistry of Solids*, no. 62, pp. 887–895, 2001.

[56] J. F. Banfield, D. R. Veblen, and D. J. Smith, "The identification of naturally occurring TiO_2(b) by structure determination using high-resolution electron microscopy, image simulation, and distance least-squares refinement," *American Mineralogist*, no. 76, pp. 343–353, 1991.

[57] M. Watanabe, H. Uchida, Y. Seki, M. Emori1, and P. Stonehart, "Self-humidifying polymer electrolyte membranes for fuel cells," *J. Electrochem. Soc.*, no. 143, pp. 3847–3852, 1996.

[58] Y. Devrim, "Preparation and testing of Nafion/titanium dioxide nanocomposite membrane electrode assembly by ultrasonic coating technique," *J. Appl. Polym. Sci.*, no. 33, p. 40541, 2014.

[59] V. Baglio, A. Aric, A. D. Blasi, V. Antonucci, P. Antonucci, S. Licoccia, E. Traversa, and F. S. Fiory, "Nafion-TiO_2 composite dmfc membranes: physico - chemical properties of the filler versus electrochemical performance," *Electrochimica Acta*, no. 50, p. 12411246, 2005.

[60] G. Colon, M. Hidalgo, G. Munuera, I. Ferino, M. Cutrufello, and J. Navo, "Structural and surface approach to the enhanced photocatalytic activity of sulfated TiO_2 photocatalyst," *Applied Catalysis B: Environmental*, vol. 63, pp. 45–59, 2006.

[61] T.Sakai, S. Kajitani, S. Kim, J. Hamagami, H. Oda, M. Matsuka, H. Matsumoto, and T. Ishihara, "Proton conduction properties of hydrous sulfated nano-titania synthesized by hydrolysis of titanyl sulfate," *Solid State Ionics*, vol. 181, p. 17461749, 2010.

[62] Z. Wu, G. Sun, W. Jin, H. Hou, and S. W. andQ. Xin, "Nafion and nanosize $TiO_2SO_4^{2-}$ solid superacid composite membrane for direct methanol fuel cell," *Journal of Membrane Science*, vol. 313, pp. 336–343, 2008.

[63] J. C. D. Filho, T. R. dos Santos, and A. de Souza Gomes, "Nanostructured polyelectrolytes based on SPEEK/TiO 2 for direct ethanol fuel cells (DEFCs)," *Polmeros*, no. 24, pp. 43–48, 2014.

[64] M. L. D. V. Z. Ahmed, S. Bellitto, A. Lenci, E. Traversa, and S.Licoccia, "SPEEK-TiO_2 nanocomposite hybrid proton conductive membranes via in situ mixed solgel process," *Journal of Membrane Science*, no. 296, pp. 156–161, 2007.

[65] Z. Dou, S. Zhong, C. Zhao, X. Li, T. Fu, and H. Na, "Synthesis and characterization of a series of SPEEK/TiO_2 hybrid membranes for direct methanol fuel cell," *Journal of Applied Polymer Science*, no. 109, pp. 1057–1062, 2008.

[66] D.Cozzi, C. de Bonis, A. DEpifanio, B. Mecheri, A. C. Tavares, and S. Licoccia, "Organically functionalized titanium oxide/ Nafion composite proton exchange membranes for fuel cells applications," *Journal of Power Sources*, no. 248, pp. 1127–1132, 2014.

Chapter 2

Experimental and theoretical background

2.1 Introduction

Raman and infrared spectroscopies allows the study of the vibrational and rotational energy levels of a material, giving responses that are characteristic of the target species. Due to the different mechanisms underlying the two effects (inelastic scattering for Raman, selective adsorption for infrared) they can be used as complementary techniques for materials analysis, because a vibrational mode active with Raman can be IR inactive or vice versa. Moreover, some problems encountered with one technique can be avoided with the other (i. e. fluorescence problem does not exist with IR and water vapour signal is almost null in Raman). For these reasons, both Raman and IR spectroscopy were used in this thesis work, and their experimental and theoretical features are described in this chapter.

2.2 Infrared spectroscopy

The discovery of the infrared region of the electromagnetic spectrum was made in 1800 by Sir William Herschel, that observed the generation of heat during his astronomical observations of the sun [1]. Forty years later the first near-IR absorption spectrum was collected by Sir John Herschel, Sir William's son, using solar radiation, a glass prism and the evaporation of alcohol on a blackened sheet of paper as the detector. In 1850, Melloni used a prism made from a large natural crystal of rocksalt to measure spectra in the middle IR. After these first experiments, a fundamental step towards the IR spectroscopy was the calibration of the spectrum in terms of wavelength, made by Lang-

ley, obtained with the measurement of the dispersion curve of the rocksalt prism. In the first years of the 20th century, thermocouples used as the coil of a galvanometer became the most used IR detectors, replacing the so-called bolometers (consisting of a narrow blackened platinum wire, with resistance depending on the temperature, as one arm of a Wheatstone bridge). However, the new detectors were still affected by problems. In fact, because of its high sensitivity, the galvanometer had to be completely screened from mechanical and electromagnetic disturbances to work properly, limiting the use of IR spectroscopy for routine work. This problem was overcome after the second world war, when developments in electronic amplification methods allowed the substitution of the galvanometer. Moreover, the invention of the double beam spectrometers, where the absorption spectrum is measured together with the incident energy, eliminated the problem of the variable output of thermal IR sources. With these improvements IR spectroscopy started to be a valuable technique for molecular structural analysis and for the qualitative/quantitative analysis of mixtures. More recently, around 1970's, another great revolution took part in the spreading of IR spectrometers: the introduction of Fourier Transform instruments (FT-IR), where the signal is collected at the same time for all the energies and the separation is then made by a PC using Fourier-transform mathematical analysis. These instruments had a great advantage: due to the simultaneous acquisition of the entire energy range, an interferogram measured over the same period of time than is required to record a dispersion spectrum with N- resolution elements has an advantage in signal to noise ratio of $\sqrt{N}$. The introduction and subsequent improvement of FTIR instruments resulted in a total transformation of the power and sensitivity of even routine IR spectrometers, allowing sample-handling methods impossible to be used before, like Attenuated Total Reflection technique and Diffuse Reflection spectroscopy.

2.2.1 Phenomenological aspects of Infrared absorption

The measurement of a sample absorption is always a two step procedure: first the radiation source intensity I_0, also called the background, has to be recorded, then the sample is put into the beam path and the radiation intensity I that hits the detector in this condition is collected. The ratio I / I_0 is the sample *transmittance* (T) and it is dependent on the radiation wavelength. Usually the spectrum intensity is measured in *absorbance*, that is defined as

$$A = -log_{10}(T) \tag{2.1}$$

The abscissa unit in vibrational spectroscopy (Ir and Raman as well) is the wavenumber, expressed in cm^{-1} and connected to the radiation frequency by the relation:

$$\tilde{\nu}_1 = \frac{\nu_1}{c} = \frac{1}{\lambda_1} \tag{2.2}$$

where λ_1 is the corresponding radiation wavelength in vacuum.

2.2.2 Theory of light absorption

Light absorption is an example of radiation-matter interaction. To properly describe this process, time-dependent perturbation theory is extremely useful [2]. The incident electromagnetic wave is represented as an additional term H_1 to the unperturbed Hamiltonian H_0 of the system, that is:

$$H = H_0 + H_1(t)$$

Dealing with a perturbation that is time-dependent, is necessary to consider the solutions of the time-dependent Schrödinger equation:

$$H\Psi = i\hbar(\frac{\delta\Psi}{\delta t}) \tag{2.3}$$

where the time-dependent wave function is

$$\Psi = \psi e^{-E_n t/\hbar} \tag{2.4}$$

The state of the perturbed system Ψ can be expressed as a linear combination of the unperturbed wave functions:

$$\Psi = \sum_n a_n \Psi_n = \sum_n a_n \psi_n e^{-E_n t/\hbar} \tag{2.5}$$

It's important to note here that if the perturbation is time-dependent, also the coefficients a_n will depend on the time. To find how they evolve, we substitute eq. 1.2 in the Schrödinger equation:

$$\begin{aligned} H\Psi &= \sum_n a_n H^{(0))}\Psi_n + \sum_n a_n H^{(1)}\Psi_n \\ i\hbar(\frac{\delta\Psi}{\delta t}) &= \sum_n a_n i\hbar(\frac{\delta\Psi_n}{\delta t}) + \sum_n i\hbar\frac{\delta a_n}{\delta t}\Psi_n \end{aligned} \tag{2.6}$$

The first terms of both equation are equivalent by eq. 2.3, and the same for the central terms. Therefore, including eq.2.4 for the Ψ_n:

$$\sum_n a_n H^{(1)} \psi_n e^{-iE_n t/\hbar} = i\hbar \sum_n \frac{\delta a_n}{\delta t} \psi_n e^{-iE_n t/\hbar} \tag{2.7}$$

To extract the expression for $\frac{\delta a_n}{\delta t}$, we can exploit the orthonormality of the basis, multiplying both sides by ψ_k and integrating all over the space. In this way, only the term $\frac{\delta a_n}{\delta t}$ with n equal to k survives, and we obtain:

$$\sum_n a_n H^{(1)}_{kn} e^{-E_n t/\hbar} = i\hbar \frac{\delta a_n}{\delta t} e^{-iE_n t/\hbar} \tag{2.8}$$

that can be rewritten as

$$\frac{\delta a_n}{\delta t} = \frac{1}{i\hbar} \sum_n a_n H^{(1)}_{kn} e^{i\omega_{kn} t} \tag{2.9}$$

The integration of the last equation from an initial time $t = 0$ when the state of the system was described by the coefficients $a_n(0)$, to the time of interest, in which the coefficients are $a_n(t)$, leads to:

$$a_k(t) - a_k(0) = \frac{1}{i\hbar} \sum_n \int a_n(t) H^{(1)}_{kn} e^{i\omega_{kn} t} dt \tag{2.10}$$

The trouble with eq. 2.10 is that the expression for a general coefficient a_n contains all the others. A way to resolve this problem is to make some approximations. Firstly, we will consider the perturbation weak. In this way the state mixing due to the perturbation remains close to the initial composition, supposed to be equal to a state i. This means that all the components $a_n(0)$ are null except $a_i(0)$. Moreover, we assume that the probability that the system is in any state other than i is always so low at any time that all the terms in $\sum_n$ in eq. 2.10 are zero except the term with n=i. Therefore eq. 2.10 became

$$a_k(t) = \frac{1}{i\hbar} \int H^{(1)}_{ki} e^{i\omega_{ki} t} dt \tag{2.11}$$

With this approximation we are supposing that the system goes from its initial state to the final one by a direct route. In doing so, we are neglecting the possibility to have several transitions in sequence, and thus the perturbation to act more than once: we are dealing with a *first order time dependent perturbation theory*.

We can now consider the $H^{(1)}$ term: in the case of an electromagnetic radia-

tion, its dependence on time will be

$$H^{(1)}(t) = 2H^{(1)}cos\omega t = H^{(1)}(e^{i\omega t} + e^{-i\omega t}) \tag{2.12}$$

and if this is inserted into eq. 2.11 we obtain

$$a_k(t) = H_{ki}\frac{1}{i\hbar}\int (e^{i\omega t} + e^{-i\omega t})e^{i\omega_{ki}t}dt = H_{ki}\frac{1}{i\hbar}\left[\frac{e^{i(\omega_{ki}+\omega)t}-1}{i(\omega_{ki}+\omega)} + \frac{e^{i(\omega_{ki}-\omega)t}-1}{i(\omega_{ki}-\omega)}\right] \tag{2.13}$$

The denominator in the first term is in the order of the radiation frequencies, and so the first term in eq 2.13 is no more than 10^{-15} in an optical spectrum. On the other hand the denominator in the second term can became close to zero as the external perturbation approaches a transition frequency ω_{ki}, and thus the first term is usually overwhelmed by the second one and can be dropped.
The probability P_k of finding the system in a final state k is equal to $|a_k|^2$, and has the expression

$$P_k(t) = \frac{4H^{(1)}_{ik}H^{(1)}_{ki}}{\hbar^2(\omega_{ki}-\omega)^2}sen^2[\frac{1}{2}(\omega_{ki}-\omega)t] \tag{2.14}$$

From this it follows that the transition probability may became close to 1 as the incident field frequency approaches a transition frequency. Moreover, if we consider that with a dipolar interaction (the simplest one between an electromagnetic field E(t) and an atom) the terms $H^{(1)}$ is equal to $-\vec{\mu}\cdot\vec{E}(t)$, is possible to obtain an important selection rule. In fact, as we saw in eq 2.14, the probability of a transition to a state k is proportional to the transition matrix element

$$H^{(1)}_{ki} = \langle\Psi_k|H^{(1)}|\Psi_i\rangle \tag{2.15}$$

and therefore is proportional to the transition dipole moment $\langle\Psi_k|\vec{\mu}|\Psi_i\rangle$. If we expand $\vec{\mu}$ in a Taylor's series, we get

$$\langle\Psi_k|\vec{\mu}|\Psi_i\rangle = \mu_0\langle\Psi_k||\Psi_i\rangle + \sum_i\langle\Psi_k|\frac{d\vec{\mu}}{dQ_i}|\Psi_i\rangle Q_i + ... \tag{2.16}$$

where Q_i are the normal coordinates of vibration. The first term on the right is null for the wave functions orthogonality, and at a first order approximation, to obtain a transition probability not zero, at least one of the $\frac{d\vec{\mu}}{dQ_i}$ must be different from zero.

2.3 Light scattering and Raman effect

The history of Raman spectroscopy began in 1928, when Sir Chandrasekhra Venkata Raman discovered the phenomenon that bears his name. In his studies he used a very simple instrumentation, being the light source the sunlight, a telescope the collector, and his eyes the detector. Despite of this, he was able to detect the extremely weak anelastically scattered component of light, which since then has been known as the Raman effect [3]. The practical use of the Raman scattering was strongly limited for lack of a proper light source until, in 1962, laser sources were developed [4]. In the next years, the Ar^+ (351.1 - 514.5 nm) and the Kr^+ (337.4 - 676.4 nm) lasers became available, and powerful monochromatic light sources were finally exploitable. In the meantime also the detection system was revolutionized, passing from photographic plates to photoelectric systems after World War II, while the use of double or triple monochromators helped in reducing the stray light. Due to all these improvements, Raman spectroscopy has now become a widely used technique in science and engineering.

2.3.1 Phenomenological aspects of the Raman effect

If a detailed analysis is carried out on the radiation scattered by a molecule, two major components can be distinguished: a relatively very intense line at the same frequency ν_0 of the incident radiation, and a series of much less intense lines at frequency $\nu_0 \pm \nu_i$. The presence of scattered peaks shifted from the incident light energy is cause by the Raman effect. In particular, the shifts are always equal to the vibrational transitions, and can be positive or negative, depending if the system absorbs from or give energy to the radiation. In Figure 2.1 an example of scattered light spectrum is given: as can be seen, the Raman lines are much less intense than the elastically scattered line (called Rayleigh line). The reason of this disparity is the much higher probability associated to a Rayleigh event with respect to a Raman one: even if both are scattering process, and thus occur at second order in the perturbation theory, for the Raman effect the creation of a photon has to occur together with the creation or the annihilation of a quantum of vibrational or rotational energy. The disparity between the elastic and the inelastic lines depends on the nature of the system, but, as a rough estimation, we can say that the Rayleigh scattering is about 3 order of magnitude less intense than the exciting radiation, and the intensity of a strong Raman band is about 10^5 times less intense than that of the Rayleigh scattering. A further difference can be found between the more intense Raman lines scattered with a frequency lower than the incident one (ν_0-ν_1), called Stokes lines, and the less intense lines at higher frequency

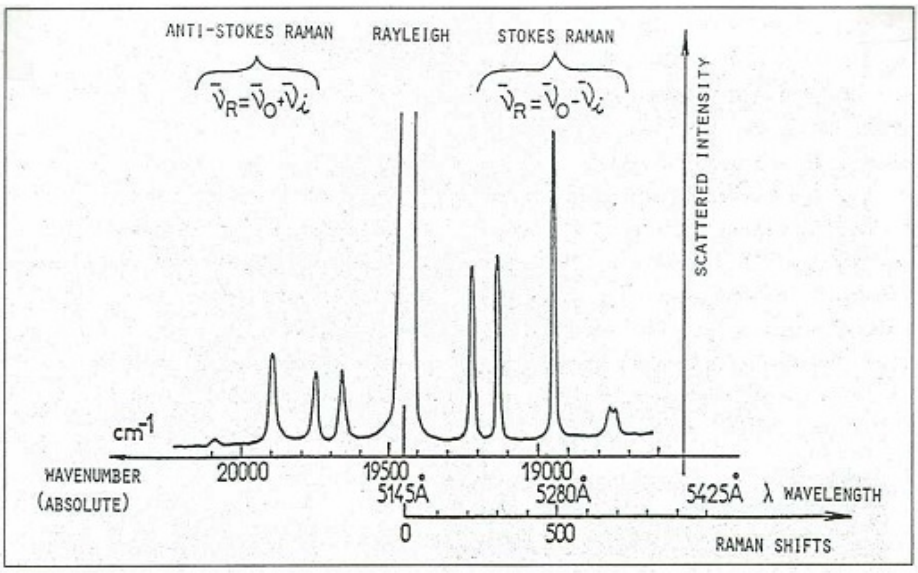

Figure 2.1: Representation of Rayleigh, Stokes and anti-Stokes components. The correspondence between wavelength and wavenumbers is also shown.

(ν_0 + ν_1), known as anti-Stokes lines. The ratio between the Stokes and the anti-Stokes intensity is temperature-dependent and is proportional to

$$exp(\frac{\hbar\omega_\nu}{K_B T}) \tag{2.17}$$

where K_B is the Boltzmann constant, T is the sample temperature and ω_ν is the frequency associated to the vibrational state ν.

Usually the Raman lines positions are showed in relation to that of the exciting light. In this way, the zero of the abscissa correspond to the Rayleigh line.
As we have seen, the Stokes lines are the more intense ones. Unfortunately, if the incident energy is close to an electronic transition of the system, also other lines can appear in the Stokes region, due to the concomitant emission of light from the system (luminescence). This is a first order process in the perturbation theory of the radiation-matter interaction, and usually the light emitted is much more intense than the scattered one. Therefore, the luminescence signal can mask the Raman effect. On the other hand, when the incident light is close to an electronic transition of the molecule (absorption), the Raman intensity can be increased by several orders of magnitude by the resonant excitation, a phenomena called Resonant Raman. The use of resonant excitation to selectively enhance the Raman signal is a widely used technique

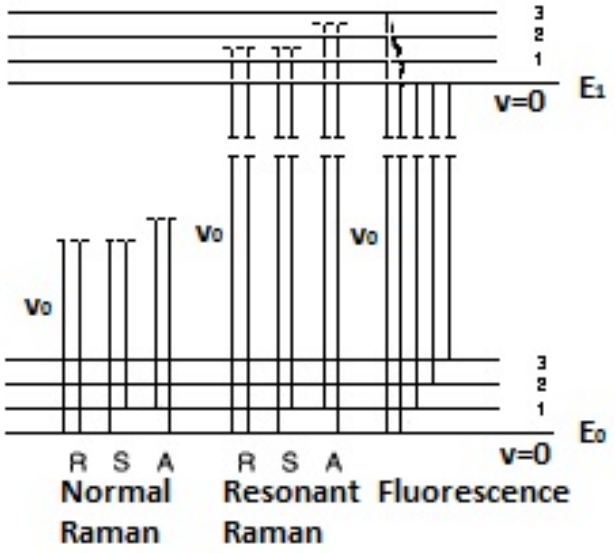

Figure 2.2: Normal Raman, resonant Raman and fluorescence phenomena in terms of energy bands involved.

when the luminescence does not cover the region of the Raman line, or it is not sufficient to mask the Raman signal.

2.3.2 Light scattering processes

To introduce the theory underlying the Raman process we will start from an analysis of a general scattering phenomenon. Let's consider a radiating system whose dimensions are small compared with the wavelength of the incident light: the source of the scattered radiation is the oscillating electric dipole induced by the perturbing electromagnetic fields of the incident light waves (in some particular cases, like in chiral systems, also the induced magnetic dipoles and electric quadrupoles play an important role in the scattering process). It is important to underline that a light scattering process does not involve the absorption of a photon, contrary to what happen in fluorescence or infrared spectroscopy. During a scattering event in fact an incident photon is not really absorbed but instead it perturbs the material's atoms or molecules, inducing an electric dipole. If the scattering phenomenon is a Raman one, this perturbation also excite or de-excite vibrational or rotational energy states. To calculate the intensity of the scattering radiation we have to consider the electric dipole moment set up in the material by the electrical field of the incident radiation. Indicating the incident electric field with

$\vec{E}_i = E_i\hat{e}_i$, the induced dipole moment is:

$$\vec{M} = \vec{\alpha}E_i\hat{e}_i \tag{2.18}$$

where $\vec{\alpha}$ is the polarizability tensor. The radiation energy emitted per unit time by an electric dipole moment oscillating at a frequency ω is:

$$\frac{dW_s}{d\Omega} = \frac{\omega^4}{(4\pi)^2\varepsilon_0 c^3}|\hat{e}_s \cdot \vec{M}|^2 \tag{2.19}$$

where ε_0 is the dielectric constant of the medium (considered isotropic and nonmagnetic), $d\Omega$ is the element of solid angle, c is the speed of light in the medium and $\hat{e}_s$ is the versor indicating the polarization direction of the scattered light.
Replacing equation 2.18 in 2.19 and dividing the latter by the incident energy per unit area and unit time $W_i = \varepsilon_0 c E_i^2$, is possible to obtain the expression fro the differential scattering cross section $d\sigma/d\Omega$:

$$\frac{d\sigma}{d\Omega} = \frac{\omega^4}{(4\pi\varepsilon_0)^2 c^4}|\hat{e}_s \cdot \vec{\alpha} \cdot \hat{e}_i|^2 \tag{2.20}$$

Now we can have to different cases, depending on the characteristics of the tensor $\vec{\alpha}$. With an isotropic polarizability tensor (as in the case of atoms or isotropic small spherical particles), the polarization plane of the incident and scattered light remain the same, and the differential cross section becomes:

$$\frac{d\sigma}{d\Omega} = \frac{\omega^4\alpha^2}{(4\pi\varepsilon_0)^2 c^4}|\hat{e}_s \cdot \hat{e}_i|^2 \tag{2.21}$$

After the integration in all the space directions we obtain the scattering cross section:

$$\sigma = \frac{4\pi\omega^4\alpha^2}{3(4\pi\varepsilon_0)^2 c^4} \tag{2.22}$$

In real systems however the polarizability tensor is usually not isotropic. However, we can always decompose it into the sum of a symmetric part $\langle\vec{\alpha}\rangle$ and an asymmetric one $\vec{\beta}$. Due to this, the cross section will consist of two components: a polarized one, called σ_p, resulting from the symmetrical part $\langle\vec{\alpha}\rangle$ of the polarizability tensor, and a partly depolarized one, called σ_d, given by the asymmetrical part $\vec{\beta}$. It is possible to demonstrate that the two components of the cross section are equal to:

$$\frac{d\sigma_p}{d\Omega} = \frac{\omega^4}{(4\pi\varepsilon_0)^2 c^4}(\langle\alpha\rangle^2 + \frac{4}{15}\beta^2) \tag{2.23}$$

$$\frac{d\sigma_d}{d\Omega} = \frac{\omega^4}{(4\pi\varepsilon_0)^2 c^4}\frac{3}{15}\beta^2 \tag{2.24}$$

The ratio between these two components is equal to:

$$\frac{\sigma_d}{\sigma_p} = \frac{3\beta^2}{15\langle\alpha\rangle^2 + 4\beta^2} \leq \frac{3}{4} \tag{2.25}$$

It is interesting to note that in both cases the intensity of the scattered light depend on the wavelength of the incident photon, and in particular is proportional to the fourth power of its frequency. This explains for example why the clear sky appears to be blue: the scatter of the sunlight has greater intensity in the higher frequencies region correspondent to the blue colour than in the red region.

2.3.3 The Raman effect: classical theory

To understand the origin of the Raman effect we will start using a simple classical treatment on a system composed by one molecule. A good starting point is to consider again the relation between the incident field $\vec{E}$ and the induced electric dipole $\vec{P}$:

$$\vec{P} = \vec{\alpha} \cdot \vec{E} \tag{2.26}$$

The polarizability tensor $\vec{\alpha}$, in general, is a function of the nuclear coordinates and thus of the molecular vibrational frequencies. Due to this, it is possible to describe the variation of the polarizability caused by the molecular vibrations by expanding each component α_{ij} in a Taylor series with respect to the normal coordinates of vibration Q (for simplicity, the expansion will be truncated at the first order, according to the so-called electrical harmonic approximation):

$$\alpha_{ij} = (\alpha_{ij})_0 + \sum_K (\frac{\delta\alpha_{ij}}{\delta Q_i j})_0 Q_k \tag{2.27}$$

where $(\alpha_{ij})_0$ is the value of α_{ij} at the equilibrium configuration, Q_k,Q_l... are normal coordinates of vibration associated with the molecular vibrational frequencies ω_k, ω_l... , and the summations are over all the normal coordinates.
Lets now focus on the mode of vibration Q_k. Equation 2.27 can be rewritten as:

$$(\alpha_{ij})_k = (\alpha_{ij})_0 + (\alpha'_{ij})_k Q_k \tag{2.28}$$

with

$$(\alpha_{ij}\prime) = (\frac{\delta\alpha_{ij}}{\delta Q_i j})_0 \tag{2.29}$$

Equation 2.28 is valid for all the tensor components, so we may write

$$(\vec{\alpha}_k) = \vec{\alpha}_0 + (\vec{\alpha}')_k Q_k \tag{2.30}$$

Assuming simple harmonic motion, the time dependence of Q_k is given by

$$Q_k = Q_{k0} cos(\omega_k t + \delta_k) \tag{2.31}$$

in which δ_k is a phase factor. Combining eq. 2.30 and 2.31 we obtain the time dependence of the polarizability tensor:

$$\vec{\alpha}_k = \vec{\alpha}_0 + \vec{\alpha}'_k Q_{k0} cos(\omega_k t + \delta_k) \tag{2.32}$$

We can now return back to equation 2.26 and introduce the time dependence of $\vec{\alpha}_0$ and of the electrical field $\vec{E} = \vec{E}_0 cos(w_1 t)$, obtaining:

$$\vec{p}^{(1)} = \vec{\alpha}_0 \vec{E}_0 cos(w_1 t) + \vec{\alpha}\prime_k Q_{k0} \vec{E}_0 cos(\omega_k t + \delta_k) cos(w_1 t) \tag{2.33}$$

Using the trigonometric identity

$$cosAcosB = \frac{1}{2}\{cos(A+B) + cos(A-B)\} \tag{2.34}$$

is possible to rewrite the second term in eq.2.33, and the new expression for $\vec{p}^{(1)}$ is now

$$\vec{p}^{(1)} = \vec{p}^{(1)}(\omega_1) + \vec{p}^{(1)}(\omega_1 + \omega_k) + \vec{p}^{(1)}(\omega_1 \omega_k) \tag{2.35}$$

where

$$\begin{aligned} \vec{p}^{(1)}(\omega_1) &= \vec{\alpha}_0 \cdot \vec{E}_0 cos(\omega_1 t) \\ &= \vec{p}^{Ray} cos(\omega_1 t) \end{aligned} \tag{2.36}$$

and

$$\begin{aligned} \vec{p}^{(1)}(\omega_1 \pm \omega_k) &= \vec{p}^{Ram} cos(\omega_1 \pm \omega_k \pm \delta_k) t \\ &= \vec{\alpha}_k^{Ram} \cdot \vec{E}_0 cos(\omega_1 \pm \omega_k \pm \delta_k) t \end{aligned} \tag{2.37}$$

with

$$\vec{\alpha}_k^{Ram} = \frac{1}{2} \vec{\alpha}'_k Q_k \tag{2.38}$$

From this treatment is clear that the radiation emitted by the oscillating dipole can be divided into three different parts:

- $\vec{p}^{(1)}(\omega_1) \propto cos(\omega_0 t)$ is the Rayleigh component
- $\vec{p}^{(1)}(\omega_1 - \omega_k) \propto cos(\omega_0 - \omega_k)t - \delta_k$, is the Stokes Raman component
- $\vec{p}^{(1)}(\omega_1 + \omega_k) \propto cos(\omega_0 + \omega_k)t + \delta_k$, is the anti-Stokes Raman compo-

nent

An important difference between Raman and Rayleigh scattering can be noted from eq. 2.37 and 2.36: while the induced dipole $\vec{p}^{(1)}$ has the same phase as that of the incident field, the Raman induced dipoles $\vec{p}^{(1)}(\omega_1 \pm \omega_k)$ are shifted in phase by a quantity δ_k, which depends on the normal vibration Q_k and changes for the different molecules. This means that interference phenomena are possible only for Rayleigh scattering, where the light irradiated by the different molecules maintains the same phase of the incident radiation, and not for Raman, where each molecule scatters with a different phase. Another important information that is possible to extract from this treatment is in eq. 2.27: not all the possible vibrational frequencies will be observed in a Raman spectrum, but only the ones that produced a change in the polarizability. In fact, for a molecular vibration to be Raman active a fundamental rule has to be respected: at least one of the components of the derived polarizability tensor $(\alpha_{ij})_k$ has to be non-zero. This leads to a fundamental selection rule of Raman spectroscopy: an active vibration must respect the condition

$$(\frac{\delta\alpha_{ij}}{\delta Q_{ij}})_0 \neq 0 \tag{2.39}$$

2.3.4 The Raman effect: quantum theory

A more exhaustive description of the Raman effect can be obtained with a quantum treatment based on time dependent perturbation theory. We can replace the induced electric dipole of the classical theory with the transition electric dipole caused by a molecular transition from an initial state, i, to a final state, f, induced by the incident electric field of frequency ω_l. The transition electric dipole $\vec{p}_{fi}$ can be represented as

$$\vec{p}_{fi} = \langle \Psi'_f | \hat{p} | \Psi'_i \rangle \tag{2.40}$$

where Ψ'_i and Ψ'_f are respectively the time dependent perturbed wavefunctions of the initial and final states of the molecule and $\hat{p}$ is the electric dipole moment operator. Is important to note that the expression

$$\Psi_r = \psi_r e^{-E_r t/\hbar} \tag{2.41}$$

used in the quantum theory of light absorption can be used only if we deal with states that have an infinite lifetime. If we have to consider also states with finite lifetime, as is the case for the Raman effect, the general wave function dependence on time can be written as

$$\Psi_r^{(0)} = \Psi_r exp(-it(\omega_j - i\Gamma_r)) \tag{2.42}$$

where $\omega_j = \frac{E_j}{\hbar}$ and the lifetime τ of the state is proportional to $\frac{1}{2\Gamma_r}$.
In eq 2.41, Ψ'_i and Ψ'_f can be expressed with a series expansion

$$\Psi'_i = \Psi_i^{(0)} + \Psi_i^{(1)} + \Psi_i^{(2)} + ... \tag{2.43}$$

and

$$\Psi'_f = \Psi_f^{(0)} + \Psi_f^{(1)} + \Psi_f^{(2)} + ... \tag{2.44}$$

where the element $\Psi^{(n)}$ is the n-order modification of the unperturbed state $\Psi^{(0)}$ induced by the perturbation. Moreover, the perturbed wave functions can be also written as linear combinations of the unperturbed wave functions, obtaining:

$$\Psi_i^{(n)} = \sum_r a_{p_{ir}}^{(n)} \Psi_r^{(0)} \tag{2.45}$$

for the general n-order element of the perturbed wave function of the initial state.The same procedure can be applied to the perturbed wave function of the final state, which gives

$$\Psi_f^{(n)} = \sum_r a_{p_{fr}}^{(n)} \Psi_r^{(0)} \tag{2.46}$$

where the $a_{p_{ir}}^{(n)}$ and $a_{p_{fr}}^{(n)}$ coefficients are given by the perturbation Hamiltonian. We assume now that the interaction Hamiltonian $\hat{H}_p$ involves only an electric dipole term, and is thus equal to $-\hat{p} \cdot \vec{E}$. It is easy to see that $a_{p_{ir}}^{(1)}$ and $a_{p_{fr}}^{(1)}$ are linear in $\vec{E}$, since to obtain them the perturbation operator acted only once on the unperturbed state. Likewise, $a_{p_{ir}}^{(2)}$ and $a_{p_{fr}}^{(2)}$ are quadratic in $\vec{E}$ and so on for the higher order coefficients. If we substitute the perturbed wave functions in eq 2.41 with the series expansions, we obtain:

$$\begin{aligned} \vec{p}_{fi} = &\langle \Psi_f^{(0)} | \hat{p} | \Psi_i^{(1)} \rangle + \langle \Psi_f^{(1)} | \hat{p} | \Psi_i^{(0)} \rangle + \langle \Psi_f^{(0)} | \hat{p} | \Psi_i^{(2)} \rangle + \\ &\langle \Psi_f^{(2)} | \hat{p} | \Psi_i^{(0)} \rangle + \langle \Psi_f^{(1)} | \hat{p} | \Psi_i^{(1)} \rangle + \langle \Psi_f^{(0)} | \hat{p} | \Psi_i^{(3)} \rangle + \\ &\langle \Psi_f^{(3)} | \hat{p} | \Psi_i^{(0)} \rangle + \langle \Psi_f^{(1)} | \hat{p} | \Psi_i^{(2)} \rangle + \langle \Psi_f^{(2)} | \hat{p} | \Psi_i^{(1)} \rangle + ... \end{aligned} \tag{2.47}$$

These terms can be collected with regards to the order of perturbation (and thus their dependence on the perturbing electric field $\vec{E}$), obtaining the following expression for the linear $\vec{p}_{fi}^{(1)}$, the quadratic $\vec{p}_{fi}^{(2)}$ and the cubic $\vec{p}_{fi}^{(3)}$ terms:

$$\vec{p}_{fi}^{(1)} = \langle \Psi_f^{(0)} | \hat{p} | \Psi_i^{(1)} \rangle + \langle \Psi_f^{(1)} | \hat{p} | \Psi_i^{(0)} \rangle \tag{2.48}$$

$$\vec{p}_{fi}^{(2)} = \langle \Psi_f^{(0)} | \hat{p} | \Psi_i^{(2)} \rangle + \langle \Psi_f^{(2)} | \hat{p} | \Psi_i^{(0)} \rangle + \langle \Psi_f^{(1)} | \hat{p} | \Psi_i^{(1)} \rangle \tag{2.49}$$

$$\vec{p}_{fi}^{(3)} = \langle \Psi_f^{(0)} | \hat{p} | \Psi_i^{(3)} \rangle + \langle \Psi_f^{(3)} | \hat{p} | \Psi_i^{(0)} \rangle + \langle \Psi_f^{(1)} | \hat{p} | \Psi_i^{(2)} \rangle + \langle \Psi_f^{(2)} | \hat{p} | \Psi_i^{(1)} \rangle \quad (2.50)$$

We focus now on the $\vec{p}_{fi}^{(1)}$ term. Applying eq. 2.45 and 2.46, this term can be written as

$$\tilde{\vec{p}}_{fi}^{(1)} = \sum_r a_{fr} \langle \Psi_f^{(0)} | \hat{p} | \Psi_i^{(0)} \rangle + \sum_r a_{ir} \langle \Psi_f^{(0)} | \hat{p} | \Psi_i^{(0)} \rangle \quad (2.51)$$

The tilde on the $\vec{p}_{fi}$ vector is a reminder that this term is usually complex. Due to this, we introduce the real induced transition electric dipole moment $\vec{p}_{fi}$ defined as

$$\vec{p}_{fi}^{(1)} = \tilde{\vec{p}}_{fi}^{(1)} + (\tilde{\vec{p}}_{fi}^{(1)})^{\star} \quad (2.52)$$

The final expression for the ρ component of the induced electric dipole turns out to be (having consider the time dependence of the wave functions expressed in eq. 2.42 and the electric field $\vec{E} = E_0 exp(it\omega_l) + E_0^{\star} exp(-it\omega_l)$

$$\begin{aligned}(p_\rho)_{fi}^{(1)} = \quad & \frac{1}{\hbar} \sum_{r \neq f,i} \left[\frac{\langle \Psi_f^{(0)} | \hat{p}_\sigma | \Psi_r^{(0)} \rangle \langle \Psi_r^{(0)} | \hat{p}_\rho | \Psi_i^{(0)} \rangle}{\omega_{rf} - \omega_l - i\Gamma_r} + \frac{\langle \Psi_f^{(0)} | \hat{p}_\rho | \Psi_r^{(0)} \rangle \langle \Psi_r^{(0)} | \hat{p}_\sigma | \Psi_i^{(0)} \rangle}{\omega_{ri} + \omega_l + i\Gamma_r} \right] \\ & E_{\sigma 0} exp[it(\omega_l + \omega_{fi})] \\ & + \frac{1}{\hbar} \sum_{r \neq f,i} \left[\frac{\langle \Psi_f^{(0)} | \hat{p}_\sigma | \Psi_r^{(0)} \rangle \langle \Psi_r^{(0)} | \hat{p}_\rho | \Psi_i^{(0)} \rangle}{\omega_{rf} + \omega_l + i\Gamma_r} + \frac{\langle \Psi_f^{(0)} | \hat{p}_\rho | \Psi_r^{(0)} \rangle \langle \Psi_r^{(0)} | \hat{p}_\sigma | \Psi_i^{(0)} \rangle}{\omega_{ri} - \omega_l - i\Gamma_r} \right] \\ & E_{\sigma 0} exp[-it(\omega_l - \omega_{fi})] + \quad complex \quad conjugate \end{aligned} \quad (2.53)$$

where

$$\omega_{rf} = \omega_r - \omega_f \quad (2.54)$$

We immediately note that the expression of the induced electric dipole has terms involving two transitions: from the initial state i to an intermediate state r, and from r to the final state f. This is exactly the case excluded in the treatment of light absorption: in fact we are now dealing with a *second order time dependent perturbation theory*.

The terms in eq. 2.53 have two different frequency dependences: those with the frequency $\omega_l - \omega_{fi}$ in the exponential term and those with $\omega_l + \omega_{fi}$. In both cases, the $(\omega_l \pm \omega_{fi})$ term is associated with real radiation only if it is > 0. According to Placzek, the terms involving $(\omega_l - \omega_{fi})$ are the ones that account for both Rayleigh and Raman scattering. In particular, if ω_{fi} is negative the final state is lower in energy than the initial state, like in anti-Stokes Raman, if $\omega_{fi} = 0$ we have a Rayleigh scattering and if ω_{fi} is positive a Stokes Raman event take place. The $(\omega_l + \omega_{fi})$ term, for photons in the visible part of the spectrum, implies that the initial state is an excited electronic state, an eventuality that we will not consider here. The transition dipole p_{fi} is also

defined as $\alpha \cdot \vec{E}$, thus the $\rho\sigma$ component of the polarizability tensor is equal to:

$$(\alpha_{\rho\sigma})_{fi} = \frac{1}{\hbar} \sum_{r \neq f,i} \left[\frac{\langle \Psi_f^{(0)} | \hat{p}_\sigma | \Psi_r^{(0)} \rangle \langle \Psi_r^{(0)} | \hat{p}_\rho | \Psi_i^{(0)} \rangle}{\omega_{ri} - \omega_l - i\Gamma_r} + \frac{\langle \Psi_f^{(0)} | \hat{p}_\rho | \Psi_r^{(0)} \rangle \langle \Psi_r^{(0)} | \hat{p}_\sigma | \Psi_i^{(0)} \rangle}{\omega_{rf} + \omega_l + i\Gamma_r} \right] \tag{2.55}$$

According to this definition, a complete knowledge of the wave functions, energies and lifetimes of all the states of a system would be needed to determine $(\alpha_{\rho\sigma})_{fi}$.

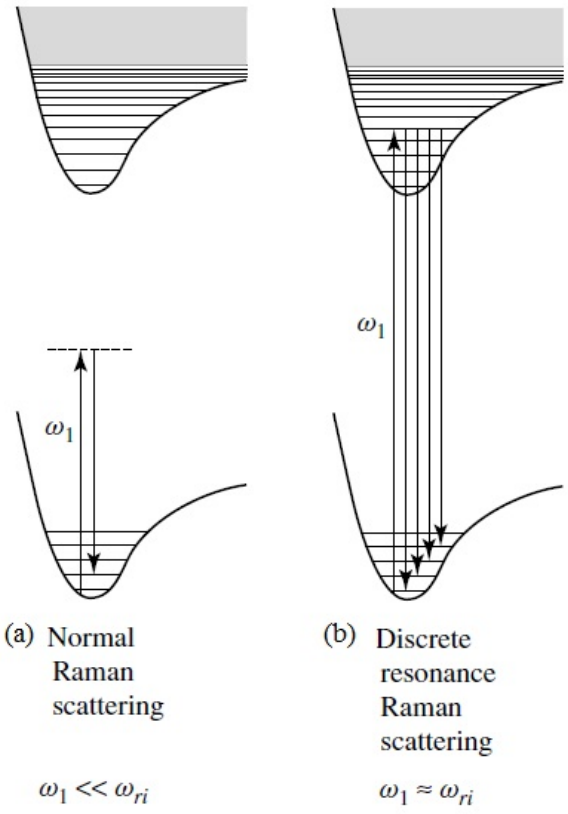

Figure 2.3: Differences between normal Raman and resonant Raman. From [5].

Fortunately, some simplifications can be done that allow a easier calculation, the most important of them being the adiabatic approximation, that allow us to separate the total wave function into an electronic, a vibrational and a rotational part, and to consider the total energy as the sum of the three energies contributions. Other approximations will not be consider here because the calculation of the $(\alpha_{\rho\sigma})_{fi}$ is not the aim of this work, but a detailed

analysis on this argument can be found in D. A. Long *The Raman Effect* [5]. Looking at the denominator term $\omega_{ri} - \omega_l - i\Gamma_r$, we can consider two extreme cases. The first one is when the frequency of the exciting radiation ω_l is much smaller than any absorption frequency ω_{ri} of the molecule. In this case we can omit the ω_l term and also the Γ_r because they are small relative to the ω_{ri}. The illustration of what happen in this case is displayed in Figure 2.1a: the molecule interact with an incident radiation of frequency ω_l and make a transition from an initial stationary state to a so-called virtual state and subsequently pass from the virtual state to a final stationary state. The virtual state is not a stationary state of the system, meaning that it is not a solution of a time-independent Schrödinger equation. Due to this, it does not have a well-defined value of the energy. If instead $\omega_l \approx \omega_{ri}$ we are approaching the condition of resonance (showed in Figure 2.3b): in this case the denominator $\omega_{ri} - \omega_l - i\Gamma_r$ became very small and the polarizability is much greater than in the normal Raman scattering condition, explaining the higher scattering intensity in Resonant Raman.

2.4 Group theory and selection rules

Group theory has a fundamental importance for both Raman and infrared spectroscopies because allows the calculation of the active vibrational modes. In particular, the activity of a mode is directly connected to its symmetry, and different rules exist to calculate Raman and IR active modes. In both cases, the first step is to consider the system symmetry. First, we analyse a system composed by a single molecule. If a movement of the molecule replace every atom with another of the same kind or do not move it at all, is called a symmetry operation. The set of all the possible symmetry operations of a molecule is called point group, where the term point underlines that no symmetry operation can move the point coincident with the center of mass of the molecule. In a real crystallographic system, only 32 point group can exist, listed in table 2.4.

If we deal with a crystal, instead of a molecule, it is always possible to define a unit cell from which the crystal lattice can be obtained through translations in the three space directions. Usually the unit cell of minimum volume, called the primitive cell, is considered. The system symmetry can thus be described through an appropriate space group, i.e. the set of symmetry operation that, when applied, leave the primitive cell unchanged. The 320 possible space groups are linked to the already definite point groups, and can be derived from the latter by the addition of new elements of symmetry (trans-

System	Axes and Angles	32 Crystallographic Point Groups
Triclinic	a b c α β γ	1 $\bar{1}$ $\mathbf{C_1}$ C_i
Monoclinic	a b c 90° β 90°	2 m or $\bar{2}$ $2/m$ $\mathbf{C_2}$ $\mathbf{C_s}$ $\mathbf{C_{2h}}$
Orthorthombic	a b c 90° 90° 90°	222 $mm2$ mmm $\mathbf{D_2}$ $\mathbf{C_{2v}}$ $\mathbf{D_{2h}}$
Tetragonal	a b c 90° 90° 90°	4 $\bar{4}$ $4/m$ 422 $4mm$ $\bar{4}2m$ $4/mmm$ $\mathbf{C_4}$ S_4 C_{4h} $\mathbf{D_4}$ $\mathbf{C_{4v}}$ $\mathbf{D_{2d}}$ $\mathbf{D_{4h}}$
Trigonal (rhombohedral)	aaa or a a c $\alpha\alpha\alpha$ 90° 90° 120°	3 $\bar{3}$ 32 $3m$ $\bar{3}m$ $\mathbf{C_3}$ $\mathbf{C_{3i}}$ $\mathbf{D_3}$ $\mathbf{C_{3v}}$ $\mathbf{D_{3d}}$
Hexagonal	a a c 90° 90° 120°	6 $\bar{6}$ $6/m$ 622 6mm $\bar{6}m2$ $6/mmm$ $\mathbf{C_6}$ $\mathbf{C_{3h}}$ C_{6h} $\mathbf{D_6}$ $\mathbf{C_{6v}}$ $\mathbf{D_{3h}}$ $\mathbf{D_{6h}}$
Cubic	a a c 90° 90° 90°	23 $m3$ 432 $\bar{4}3m$ $m3m$ $\mathbf{T}$ $\mathbf{T_h}$ $\mathbf{O}$ $\mathbf{T_d}$ $\mathbf{O_h}$

Figure 2.4: The seven crystallographic system and the 32 point groups. From [6].

lations, screw axes, glide planes) that can exist only in extended systems.
Coming back to the simple one-molecule system, we focus on the atoms of the molecule, and in particular on the three spacial coordinates x, y and z, of each atom. If we apply one of the symmetry operations belonging to the point group, the coordinate x of the atom i can remain unchanged, changed into the negative of itself, or moved to a completely different coordinate (for example, the y coordinates of atom j). If we repeat this procedure for the coordinates of all the atoms, we can construct a matrix of dimension 3N were a 1 in the position (n,m) means that the n-th coordinate was moved to the m-th one (or to the negative of m if we have a -1). We can construct a similar matrix for all the symmetry operations, and obtain the so-called total representation of the symmetry operations. The sum of the diagonal elements of the total representation is called the character of the operation. A question now arises: can we reduce all of these matrix, in the same time, to a diagonal form, or at least in a block-diagonal form? The answer is yes, and group theory help us in the construction of the new matrix. Each block in the new matrix is called irreducible representation and can be labelled according to its symmetry species, that is the list of its characters for each operation of the point group. The informations about the irreducible representation and their characters for a given point group are summed up in the so called character table (see Table 2.1 for an example). We can see in Table 2.1 that, in addition to the Schoenflies symbol of the point group, the first line contains all the sym-

Table 2.1: Character table for the C_{2h} point group, from [7]

C_{2h}	E	C_2^z	i	o_h		
A_g	1	1	1	1	Rz	α_{xx},α_{yy},α_{zz},α_{xy}
A_u	1	1	−1	−1	T_z	
B_g	1	−1	1	−1	R_x,R_y	α_{xz},α_{yz}
B_u	1	−1	−1	1	T_x,T_y	

metry operations that constitute it. The following lines of the table contains the characters of one of the irreducible representations of the group, preceded by its symbol. The symbol is a convention to describe some properties of the representation, like the dimension (A or B for a one dimensional representation, E for a two-dimensional and F for a three-dimensional), the symmetry with respect to the inversion through the center (u or g), and the symmetry with respect to rotations about the principal axis (A or B for one-dimensional representations). The right side of the character tables indicates the symmetry of molecular translation (T), rotation (R), and polarizability (α). A simple formula exists which gives the number of times each irreducible representation will appear when the reduction process is completed. If the group has g symmetry operation, with characters X_i in some reducible representation, the number N of irreducible representation of symmetry type Γ is given by

$$N = \frac{1}{g} \sum X_i X_i^{\Gamma} \tag{2.56}$$

where X_i is the character of the reducible representation of the symmetry operation i, and X_i^{Γ} is the character of the irreducible representation of symmetry Γ for the symmetry operation i. In this way is possible to know all the irreducible representations of the reduced matrices. After the reduction process of the original matrices, the reduced block-diagonal matrices have of course different basis than the atomic coordinates. In particular, the new basis are a combinations of the atomic coordinates, known as normal coordinates, and each one is characterized by the same symmetry properties of one of the irreducible representations.
The reduced matrices are still of dimension 3N, but if we consider all the independent vibrations of a molecule composed by N atoms we obtain a number equal to 3N - 6: in fact, to the possible 3N movements, we have to exclude 3 rigid translations and 3 rotations of the entire molecule. In term of irreducible representations, we have to exclude three representations that have the same symmetry of a translation, and three with the same symmetry of a rotation. For the next step in the calculation of IR and Raman active modes,

is important to remember that the transition probability is proportional to $\langle \Psi_k | \vec{\mu} | \Psi_i \rangle$ in infrared spectroscopy and to $\langle \Psi_k | \alpha | \Psi_i \rangle$ in Raman spectroscopy. To be different from zero, these integrals have to be invariant under all the symmetry operation of the group, because their values can not vary under operation that leave the system untouched, or, in other words, the symmetry of the integrals must be the same of the molecule, so it must be equal to the total symmetric representation of the point group. For this to be, the direct product of the irreducible representation of the integrands functions (for example Ψ_k, $\vec{\mu}$ and Ψ_i for IR) must contain the totally symmetric irreducible representation A_1. The initial state Ψ_i is already a basis for A_1, and only if μ and Ψ_k have the same irreducible representation their direct product contains A_1, and the integral can be different from zero. Moreover, the symmetries of the components of the $\vec{\mu}$ vector are the same of the coordinate x, y and z of translation, and we can know them from the character table. The symmetry of the first vibrationally excited state is the same as the normal coordinate of the vibrational mode in consideration, meaning that if the system jump to a final excited state Ψ_k, the symmetry of Ψ_k is the same of the normal vibration coordinate k. The symmetries of the normal modes of vibration of the system are equal to the irreducible representations. In the example in tab 2.1, the $\vec{\mu}$ components have the same symmetries than the irreducible representation A_u (μ_z) and B_u (μ_x and μ_y). In we take the normal vibrational modes which are basis for the irreducible representations A_u and B_u, these have the same symmetries than the $\vec{\mu}$ components, and thus are infrared active. The same argument is valid also for Raman active modes, with the polarizability components instead that the $\vec{\mu}$ components.
If we are not considering a single molecule, but a crystal, the calculation of the active modes is not so straight forward, even if the number of vibrational modes and their symmetries can be determined with the same general rule as for free molecules. A method for the analysis of the crystal unit cell and the determination of the selection rules is the *nuclear site group analysis*. With this method the first step is to analyse the position of each atom and under which symmetry element of the point group its environment remain the same, or, in other word, determine the site symmetry of the atom. After this, a mapping procedure is necessary to link the irreducible representation of the site symmetry to the irreducible representation of the crystal point group. This procedure is facilitated by the existence of tables (see for example reference [7]) that already include these informations. Differently from the single molecule case, pure rotational and translational movement do not exist in a lattice. Instead, of all the possible crystal vibrations, three belong to the so-called acustic branches and are characterized by a phonon energy-momentum relationship in which the energy approach zero when the momentum tend to

zero. Being infrared and Raman spectroscopies characterized by a total exchanged momentum really small (a photon in the visible or IR range has a smaller momentum than a phonon of the same energy), the acustic modes are not usually measurable with these two techniques. Due to this, three of the total irreducible representation have to be removed, and are the ones with the same symmetry of the acustic modes, that is the same of the translations. Once that all these procedures are performed, the determination of the Raman and IR active modes remains the same as already seen with a single molecule.

2.5 Experimental setups

2.5.1 Micro-Raman spectrometers

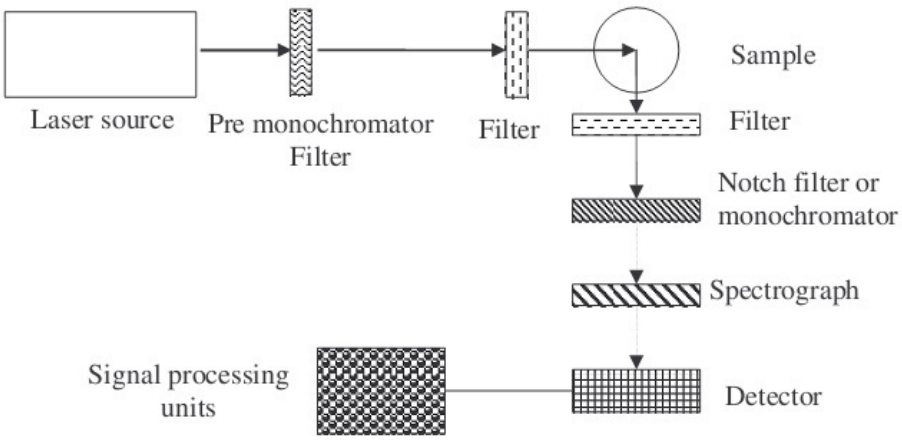

Figure 2.5: General scheme of a Raman spectrometer

An apparatus for the acquisition of a micro-Raman spectrum is essentially composed by the elements shown in Figure 2.5, that are:

- an excitation source, usually a laser beam passing through a system of lenses and filters
- an optical system that focus the light on the sample and concurrently collect the scattered radiation
- a filtering system, that eliminate the Rayleigh component
- a dispersive stage, usually a grating spectrograph
- a photon detector, usually a CCD detector.

In the present thesis, two different micro Raman instruments were used, an Horiba LABRAM HR800 and an Horiba T64000.

2.5.1.1 Horiba LABRAM HR800

The Jobin Yvon HR800 micro-Raman spectrometer is an integrated Raman setup, where a microscope is coupled to a 800 mm focal length spectrograph [8]. The exciting source is a He-Ne laser which provide a line at 632,8 nm, with a power of about 6 mW on the sample surface. If a lower laser power is needed, a neutral filter with optical density 0.3, 0.6, 1, 2, 3 or 4 can be placed in the light path. The laser beam is focused on the sample through an Olym-

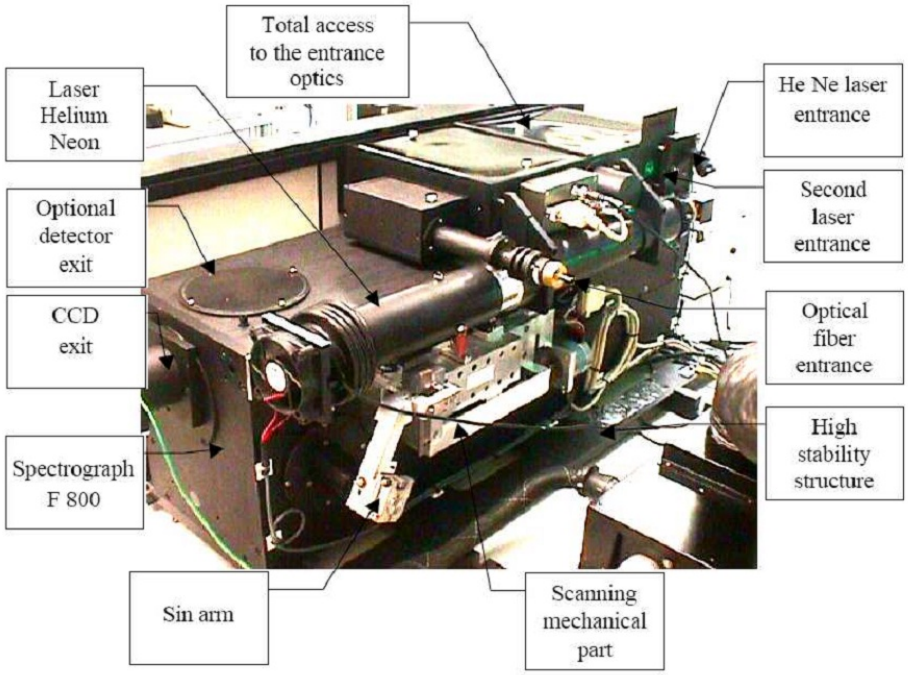

Figure 2.6: Picture of the Horiba LABRAM HR 800 instrument

pus microscope (model BX 40) equipped with different available objectives, having magnification, working distance and numerical aperture enlisted in table 2.2. The sample surface and the focusing point of the laser beam can be observed through a color camera for the direct selection of the sample region to probe. The scattered light is collected by the same objective used for the excitation, in the so-called backscattering configuration. The Rayleigh component is then eliminated by a notch filter, that reflects the light in a narrow wavenumber range centered at the laser line, and allow for the transmission of the inelastically scattered light. If the wavelength of the laser is changed, another notch filter centered at the right wavelength is necessary. This kind of filtering system (Holographic notch filters) is fabricated with laser holography technique and is constituted by a three-dimensional lattice of polymeric microspheres, sandwiched between two quartz plates. The distance between

Table 2.2: Available objectives for the micro-Raman spectrometers

Magnification	Numerical aperture	Working distance (mm)
4X	0.1	20
10X	0.25	10.6
50X	0.75	0.38
50X Long WD	0.5	10.6
80X Long WD	0.75	4.1
100X	0.9	0.21

the microspheres is in the order of the excitation wavelength, meaning that the Rayleigh scattered light is reflected while the inelastic component passes through it. Although this filtering system has a quite narrow range of reflected wavelengths, is impossible to measure spectra in the wavenumber region below 100 cm^{-1} from the exciting line. After the filtering procedure, the scattered radiation is dispersed by the HR800 spectrograph, equipped with two interchangeable gratings of 1800 g/mm and 600 g/mm, respectively, and finally reaches the CCD. This type of detector is made by photosensitive elements, that are charged by the striking photons. The charge reading procedure, made by a single analogue-to-digital converter, is divided in different step: first the top row of pixels is read element by element by moving the elements from left to right, then all the rows are shifted up one step, and the reading procedure of the next row begin.

2.5.1.2 Horiba T64000

The triple monochromator Horiba T64000 system was used to study the spectral region below 200 cm^{-1}, a task possible due to the excellent filtering setup of the Rayleigh line present in this spectrometer [9]. The excitation source consist of a mixed Ar-Kr ion gas-laser (Spectra-Physics; Model: 2018RM03) which provides about fifteen different lines of monochromatic light with wavelengths between 454.5 nm and 676.4 nm (a list of the more intense laser lines is showed in Table 2.3). The laser system is water-cooled to assure the stability of the light beam. Among the various laser system, the multi-line ones present to a greater extent the problem of the plasma lines, which fall at different frequencies from the selected beam. In order to remove them, the beam is preliminarily filtered by a pre-monochromator before being focused into the micrometric region on the sample through the microscope objective. One of the possible configuration of the instrument is the backscattering configuration, where the light is focused and collected by the same objective. The T64000 instrument is equipped with an optical microscope Olympus (model

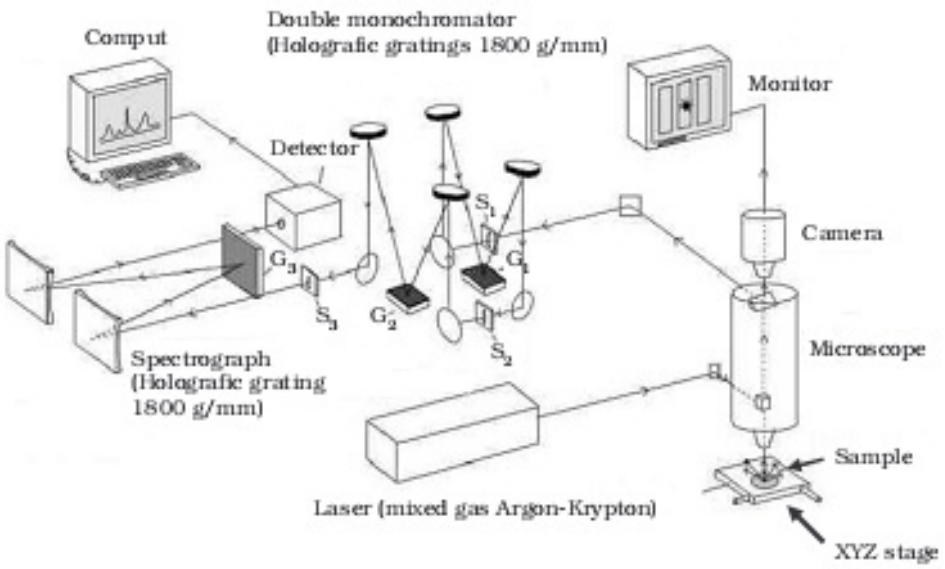

Figure 2.7: Horiba T64000 scheme

BX41) mechanically integrated into the system with the possibility to work with 6 different objectives, already enlisted in Table 2.2.

After the collection, the scattered radiation is filtered to eliminate the intense Rayleigh scattering. For this purpose, as already said, the commonly used notch filters have a great limitation: they can not properly cut the radiation under 100 cm^{-1}. To avoid this restriction, a different type of optical filter was used in this spectrometer, based on thick volume Bragg gratings (VBSs) [10, 11]. These filters are made by photo-thermo-refractive glasses printed with a periodic modulation of the refractive index, which in this way forms a grating having a well-defined Bragg resonance, enabling the design of light

Table 2.3: T64000 : available laser lines

Wavenumber	Power
457.9 nm	30 mW
476.5 nm	150 mW
488.0 nm	250 mW
514.5 nm	250 mW
520.8 nm	100 mW
530.9 nm	200 mW
568.2 nm	150 mW
647.1 nm	300 mW

filters having a narrower bandwidth than notch filters. To obtain a proper cut of the elastic scattering, usually 2 or 3 filters should be placed in series, thus increasing the system costs. The double monochromator of the T64000 spectrometer, exploited to filter the Rayleigh line, can work in two different configurations, depending on how the two single monochromators are coupled. In the subtractive configuration, after the initial selection of the wavenumber range made by the first monochromator, the light is refocused by the second one and finally reselected by the spectrograph, allowing a double cut of the Rayleigh light and a working range close the laser line (until about 5 cm$-$1). In the additive configuration, the light dispersion obtained with the first monochromator is increased by the second one, with an overall gain in the resolution. However, in this case the elimination of the unwanted light is not so efficient as in the subtractive configuration. The system configuration used in this thesis work is the subtractive one, in order to explore the spectral zone not visible with the LABRAM system.
After the double monochromator, the beam is dispersed by the spectrograph and finally reach the multichannel CCD detectors (model Simphony, 1024 X 256 pixels and pixel size 26 μm X 26 μm), cooled by liquid nitrogen down to 134 K. As a matter of fact, for the analysed samples, the LABRAM HR system had the best performance in the wavenumber range over 200 cm^{-1}, resulting in spectra with a higher signal to noise ratio. This is due to the lower total transmittance of the double monochromator compared to that of the notch filter that means, for signal acquisition times of the same duration, a worse signal to noise ratio. Moreover, only a higher samples fluorescence was observed shifting the laser line from 632.8 nm to higher energies, with absolutely no advantages obtained by the use of the T64000 multi-line laser.

2.5.2 FT-IR spectrometer

A simple scheme of an FT-IR instrument is showed in Figure 2.8: the infrared polychromatic radiation is directed toward the interferometer, where a beamsplitter divided the beam in two part: one reaches a moving mirror and the other a fixed mirror. The two rays are then recombined, pass through the sample compartment and arrive to the detector.
The Michelson interferometer, the core of a Fourier Transform infrared spectrometer, deserves a more detailed description. When the beam arrive on the beam splitter, it is divided into two parts. The one that is reflected by the fixed mirror always covers the same distance, but the one that goes to the moving mirror has a different distance to cover as a function of time. This means that when the two beams are reunited they have different phases, and interference phenomena occur. For a monochromatic radiation, the intensity

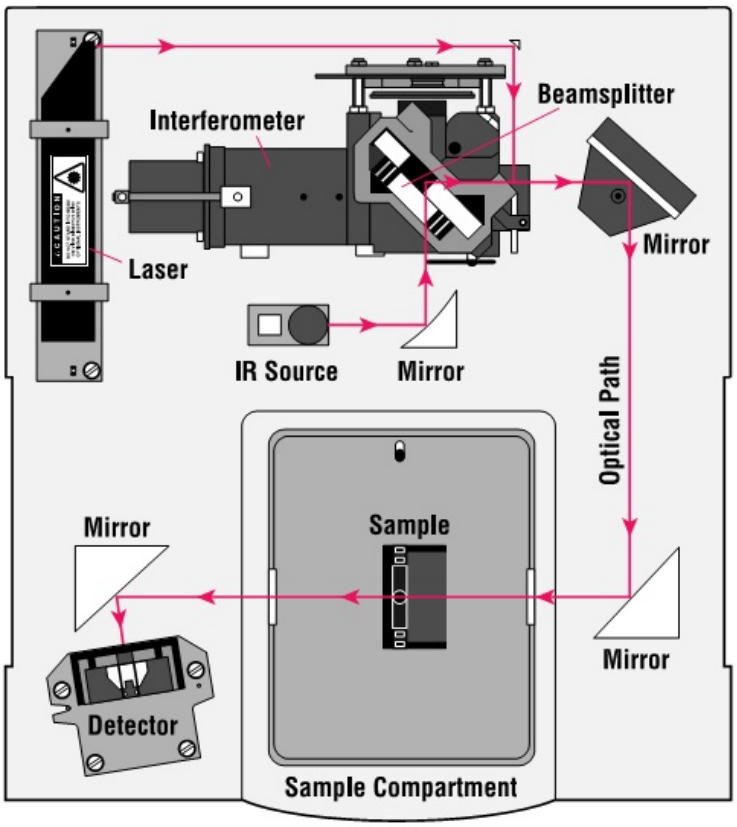

Figure 2.8: Scheme of a Fourier Transform infrared spectrometer, from [12]

after the recombination is

$$I(\delta) = \frac{1}{2} I_0 (1 + cos(2\pi\nu\delta)) \tag{2.57}$$

where I_0 is the intensity before the interferometer, and δ is the optical path difference between the moving and the fixed mirrors, that is time-dependent. The term

$$I(\delta) = \frac{1}{2} I_0 cos(2\pi\nu\delta)) \tag{2.58}$$

is called *interferogram*. In an FT-IR instrument, the infrared beam is composed by an infinite number of monochromatic components. To understand what happen in this case firstly we will deal with a finite number of components and then we will analyse the infinite case. With finite monochromatic components the resulting interferogram is the sum of the individual contributions:

$$I(\delta) = \sum_i B(\nu_i) I_0 (cos(2\pi\nu_i\delta)) \tag{2.59}$$

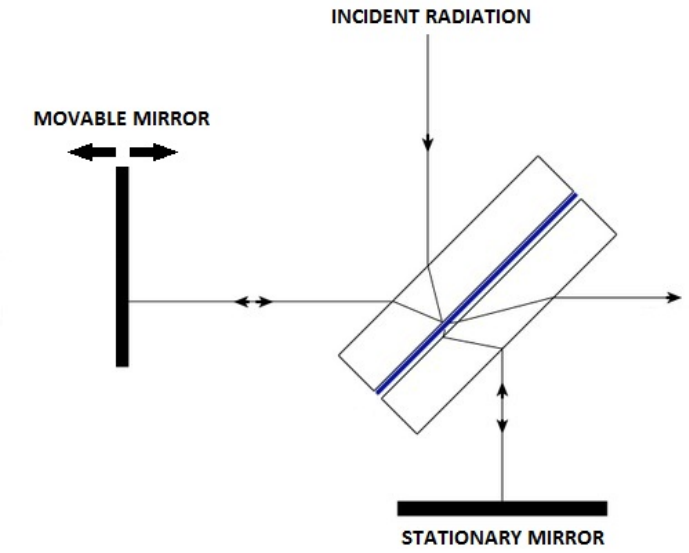

Figure 2.9: Different light paths in a Michelson interferogram.

where $B(\nu_i)$ is proportional to the intensity of the component with wavenumber ν_i. In the case of a continuous spectrum with infinite monochromatic contributions the sum became an integral:

$$I(\delta) = \int_{-\infty}^{+\infty} B(\nu_i) I_0(cos(2\pi\nu_i\delta)) = 2\int_0^{\infty} B(\nu_i) I_0(cos(2\pi\nu_i\delta) \qquad (2.60)$$

where $B(\nu)$ is the source spectrum. The interferogram is thus the inverse Fourier Transform (FT) of the $B(\nu)$ spectrum, and vice-versa, the spectrum is the FT of the interferogram. If a sample absorbs part of the incident light, the interferogram will have a lower contribution from the frequencies ν_i corresponding to a sample adsorption band. After the signal acquisition, a PC is mandatory to perform the Fourier Transform on the interferogram and obtain the spectrum.

2.5.2.1 JASCO FTIR 660 plus

The IR spectrometer used in the present thesis was a single beam Jasco 660 plus FTIR. In this instrument the radiation source is a heated ceramic coil, while the beamsplitter is composed by Ge coated KBr substrates. The transmitted radiation is collected by a DLATGS (deuterated L-alanine doped TriGlicine Sulfate, a pyroelectric material) detector [13]. The sample chamber and the interferometer chamber can be evacuated separately to avoid the presence of CO_2 and water vapour, that strongly absorb the infrared radiation. Gas like N_2 can be purged in the chambers as well. The instrument has a maxi-

mum resolution of 0.5 cm^{-1}, but for all the spectra presented in this work the resolution was set to 4 cm^{-1} to avoid excessive noise.

2.5.2.2 ATR technique

Attenuated Total Reflection (ATR) spectroscopy is an alternative technique for the measure of IR absorption, particularly suitable for really thin samples or too-adsorbing ones. Usually the sample is measured as received, and no additional preparation is needed. With this technique, the IR beam coming from the radiation source is deflected into a crystal, with a proper entrance angle to assure the complete beam reflection at the crystal inner surface (see Figure 2.10 for the radiation path scheme). To obtain this, the entrance an-

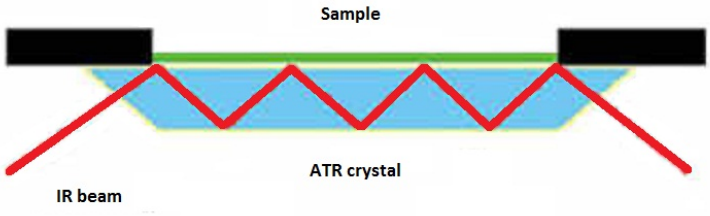

Figure 2.10: Multiple reflection inside an ATR crystal

gle has to be bigger than the critical angle θ_c, that has a value given by the equation

$$\theta_c = sen^{-1}(\frac{n_2}{n_1}) \tag{2.61}$$

where n_1 is the refractive index of the crystal, and n_2 the one of the sample [14]. If this is respected, multiple internal reflection of the IR radiation are obtained inside the crystal. If a sample is put onto the crystal surface a part of the radiation, called evanescent wave, enter in the first μm of the sample surface, and here is partially adsorbed. This happens for each multiple reflection, thus giving multiple absorptions. The depth of penetration of the evanescent wave, called d, is defined as the distance at which the wave intensity is $\frac{1}{e}$ of the original one, and its value is is dependent on the wavelength of the incident radiation, the angle of incidence and the sample and crystal refractive index:

$$d = \frac{\lambda}{2\pi\, n_1 \sqrt{sen^2\theta - (n_2/n_1)^2}} \tag{2.62}$$

In our laboratory, two crystals are available: one is made by ZnSe and the other by Ge, both with an entrance angle of 45°, but with different refractive index n (n=4 for Ge, n=2.4 for ZnSe) and chemical resistance. Usually in the

IR range d is about 2 microns with the ZnSe crystal cut at 45°, and about 1 microns for the Germanium crystal in the same conditions. The higher refractive index of Ge with respect to ZnSe also means, for high refractive index samples like composite polymers, that the critical angle is bigger than 45°for ZnSe but is still lower for Ge, and only with the last one the total reflection condition is fulfilled.

Bibliography

[1] N. Sheppard, *The Historical Development of Experimental Techniques in Vibrational Spectroscopy*.

[2] P. W. Atkins, *Molecular quantum mechanics*. 1983.

[3] C. Raman and K. Krishnan, "A new type of secondary radiation," *Nature*, vol. 121, pp. 501–502, 1928.

[4] T. Gilson and P. Hendra, *Laser Raman Spectroscopy*. 1970.

[5] D. A. Long, *The Raman effect*. 2002.

[6] K. Nakamoto, *Infrared and Raman Spectra of Inorganic and Coordination Compounds: Theory and applications in inorganic chemistry*. 1997.

[7] D. Rousseau, R. Bauman, and S. Porto, "Normal mode determination in crystals," *Journal of Raman spectroscopy*, no. 10, pp. 253–290, 1981.

[8] H. Jobin-Yvon, "Labram series."

[9] H. Jobin-Yvon, "Triple raman spectrometers."

[10] S. Blais-Ouellette, 2009.

[11] D. Psaltis, "Coherent optical information systems," *Science*, vol. 298, pp. 1359–1363, 2002.

[12] Thermo-Nicolet, *Introduction to Fourier Transform Infrared Spectrometry*.

[13] S. ES, *Pyroelectric DLATGS Infrared Detectors For Instrumentation*.

[14] P. technologies, *HATR Horizontal Attenuated Total Reflectance Accessory*.

Chapter 3

Composite Nafion with SnO_2 and SnO_2-S as filler

3.1 Tin oxides vibrational properties

All the tin oxide powders studied in this work are nanometric, a characteristic that always influences the vibrational features of a material. However, the vibrational properties of the single crystal are always a good starting point for the interpretation of the nanosystem features. According to nuclear site group analysis, in order to calculate the crystal active modes is fundamental to know which space group the composite belong to and the atoms site symmetries.
In the case of SnO_2, the primitive cell has a tetragonal rutile structure belonging to the D_{4h}^{14} space group, with two molecules per unit cell (Fig 3.1a). The

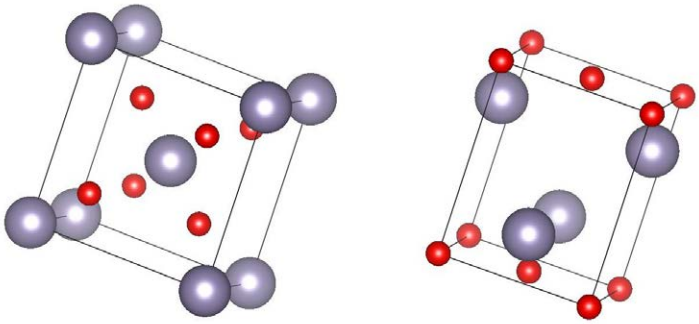

Figure 3.1: a) SnO_2 crystal unit cell and b) SnO crystal unit cell. Oxygen atoms are colored in red, tin atoms in violet. Figures obtained with the program VESTA [1]

two Sn atoms are in sites with $D_{2h}^{'}$ symmetry, while the four O atoms are in $C_{2v}^{'}$ sites (Wyckoff 2a and 4f sites, respectively). With these sites occupied, the

irreducible representations of the vibrational modes at the Γ point of the Brillouin zone are: $1A_{1g} + 1A_{2g} + 2A_{2u} + 1B_{1g} + 1B_{2g} + 2B_{1u} + 1E_g + 4E_u$. Among the 18 total vibrational modes, 3 has to be acoustic: looking at the character table for the D_{4h} symmetry (table 3.1) is possible to conclude that the acoustic irreducible representation are A_u and E_u. The remaining 15 optical modes are not all active in Raman or IR; again the active modes are easily recognizable: 5 are Raman active, (A_{1g}, B_{1g}, B_{2g} and one twofold degenerate E_g) and 7 are IR active (A_{2u} and three twofold degenerate E_u). From literature corresponding atomic displacements of the Raman active modes is known: the A_{1g} and B_{2g} modes are related to the contraction and expansion of the Sn-O bond, while the E_g modes are due to the vibration of oxygen in the oxygens plan [2].
As regards the vibrational energy, 3 of the 4 expected Raman peaks were observed in single crystal at about 476, 638 and 782 cm^{-1}, while no evidence was found of the fourth peak, that theoretically has to be at a energy of about 100 cm^{-1} [3]. IR peaks were detected, for single crystal, at 465 cm^{-1} (A_{2u}) and 243, 284 and 605 cm^{-1} (3 E_u) [4].

Due to the presence in the analysed samples of SnO (as it will be shown in the next section), also the calculation of the active modes for this oxide form has been included. As already explained in Chapter 1, SnO has a different crystal structure than SnO_2, with a different spatial group symmetry, even if still tetragonal: it belongs in fact to the D^7_{4h} group. Inside the crystal site the tin atoms are in sites with symmetry C_{4v}, while oxygens are in D_{2d} sites. Due to this, the vibrational irreducible representations are 1 A_{1g} + 2 A_{2u} + 1 B_{1g} + 2 E_g + 2 E_u. Having the same point group than SnO_2 (D_{4h}), the character table (Table 3.1) and the selection rules are identical, resulting in six Raman active modes (with symmetry A_{1g}, B_{1g} and two twofold degenerate E_g)and three IR active modes (with symmetry A_{2u} and E_u). The atom displacements corresponding to the active modes are known from [6]: all the Raman modes are movement of tin or oxygen atoms on the same plain in opposite directions, while the IR active modes are characterized by the same vibrational direction for atom of the same element (causing a displacement of the tin sublactice with respect to the oxygen sublactice). SnO Raman peaks were detected at 113 and 211 cm^{-1} in thin films ([6]), with E_g and A_{1g} symmetry respectively [7], while the B_{1g} peak and second E_g peak, predicted around 360 and 475 cm^{-1}have never been detected. In IR spectra, usually a broad band is found around 300 cm^{-1}, that correspond to a superposition of the expected A_{2u} and E_u peaks [8].
Due to the growing interest in nanostructured systems, several studies have been recently focused on the synthesis and characterization of tin oxides with nanometric dimensions, and the effect of the size on the vibrational spectra were studied as well: among the observed effects there were the lowering

Table 3.1: Character table for the D_{4h} point group. From [5].

D_{4h}	E	$2C_4$	C_{2z}	$2C_2$	$2C_2^{'}$	i	$2S_4$
A_{1g}	1	1	1	1	1	1	1
A_{1u}	1	1	1	1	1	−1	−1
A_{2g}	1	1	1	−1	−1	1	1
A_{2u}	1	1	1	−1	−1	−1	−1
B_{1g}	1	−1	1	1	−1	1	−1
B_{1u}	1	−1	1	1	−1	−1	1
B_{2g}	1	−1	1	−1	1	1	−1
B_{2u}	1	−1	1	−1	1	−1	1
E_g	2	0	−2	0	0	2	0
E_u	2	0	−2	0	0	−2	0

D_{4h}	o_h	$2o_v$	$2o_d$		
A_{1g}	1	1	1		$\alpha_{xx} + \alpha_{yy}$, α_{zz}
A_{1u}	−1	−1	−1		
A_{2g}	1	−1	−1	R_z	
A_{2u}	−1	1	1	T_z	
B_{1g}	1	1	−1		α_{xx} - α_{yy}
B_{1u}	−1	−1	1		
B_{2g}	1	−1	1		α_{xy}
B_{2u}	−1	1	−1		
E_g	−2	0	0	(R_x,R_y)	(α_{xz},α_{yz})
E_u	2	0	0	(T_x,T_y)	

of the vibrational energy [9], the presence of symmetry forbidden peaks (for example IR active peaks can also appear in Raman spectra [10]), the broadening of the peaks and additional broad structures due to amorphous phases or surface phonon modes [11].

3.2 Nafion vibrational properties

The theoretical calculation of the Nafion active modes is almost impossible due to the difficulty in defining the polymer symmetry. Due to this, all the studied performed on Nafion vibrational properties try an interpretation of the experimental data based on the knowledge of Teflon spectra, for the backbone chain, and of simplified molecule spectra for the sidechains.
Teflon has been widely studied with Raman and IR in the past because of its wide technological importance. Under atmospheric pressure it possess a helicoidal structure whose pitch depends on the temperature: at room temperature the repeat units contains 15 CF_2. This chain configuration belongs

to the $D_{14\pi/15}$ space group, meaning 4 A_1 Raman active modes, 3 A_2 IR active modes, 8 two-fold degenerate E_1 IR and Raman active modes and 9 two-fold degenerate E_2 Raman active modes [12].
All the Raman peaks of Teflon were observed in the Nafion spectrum with almost no energy shift, while the exact positions for the IR peaks of Nafion is more difficult to determine due to significant broader peaks compared to the Teflon ones, especially in the 1100-1300 cm^{-1} region, where different peaks are overlapped and not clearly separable. Due to this, the attribution of the corresponding backchain vibrational mode to each of the IR peaks is still controversial, and different interpretations are given in literature. Notwithstanding the attribution differences, all the IR studies reported two main peaks in the range from 1100 to 1300 cm^{-1} composed by the convolution of different vibrational modes, prevalently CF_2 vibrations: with ATR technique and dry membrane, one is at 1153 cm^{-1}, and the second at 1211 cm^{-1} [13].
The remaining Nafion peaks, not present in the Teflon spectrum, have to be-

Table 3.2: Assignments of the Raman and IR (200 - 1400 cm^{-1}) peaks of Nafion, from [14] (only the peaks with an assigned mode are reported)

Raman (cm^{-1})	IR (cm^{-1})	Symmetry class	Assignment
292		A_1	t(CF_2)
310		E_2	t(CF_2)
385		A_1	δ(CF_2)
390	511	E_2	δ(CF_2)
	557	A_2	t(CF_2)
574		E_1	δ(CF_2)
	626	A_2	ω(CF_2)
	641	A_2	ω(CF_2)
731	719	A_1	ν_s(CF_2)
741	780	E_2	ν_s(CF_2)
805	805		ν(CS)
971	970		ν_s(COC)
1060	1058		$\nu s(SO_3^-)$
	1130		$\nu_{as}(SO_3^-)$
	1148	E_1	ν_{as} (CF_2)
	1204	A_2	ν_{as} (CF_2), $\nu_{as}(SO_3^-)$
1216	1216	E_1	$\nu_{as}(CF_2)$
1297	1300	E_2	ν(CC)
1377		A_1	ν_s(CC)

long to the sidechain vibrations. At about 1058 cm^{-1} (both in Raman and IR) the symmetric stretching vibration of the SO_3^- group is recognized, in agreement with the study on polystyrene- and on trifluoromethane-sulfonic acid

[15, 16]. This vibration provides fundamental informations about the effect of the environment on the exchange properties of the membrane, and has a clear energy shift depending on the SO_3^- surrounding environment, like the local hydration level. The corresponding asymmetric vibration, expected in the IR in a range from 1100 to 1400 cm^{-1}, is unfortunately hidden by the more intense CF_2 stretching vibrations, and can not be located precisely. However, a sure proof of the presence of this peaks under the main CF_2 ones is the shift, in IR, of the maxima of the peaks at 1153 and 1212 cm^{-1} with different membrane hydration, in tune with the behaviour of the SO_3^- symmetric vibration. A peak at 970 cm^{-1} is observed in both Raman and IR, and was attributed by all authors to the C-O-C symmetric stretching. A second band, whose attribution is more controversial, appears in IR at around 983 cm^{-1}: while there is accordance that it is due to a vibration of the C-O-C groups, some authors assign it to the ν_s mode of C-O-C groups embedded in the ionic clusters [17] while others attribute it to the anti-symmetric ν_{as} mode of C-O-C [18]. Finally, the IR and Raman feature at 805 cm^{-1} were assigned to the symmetric C-S stretching vibration.
A summary of the proposed attributions is presented in Table 3.2 [14].

3.3 Materials synthesis

SnO_2 and S-SnO_2 powders were obtained in the form of highly hydrated nanosized particles by a wet chemistry synthesis, already described in [[19]]. $SnCl_4$ was dissolved in water and therefore a 30% NH_3 water solution was added dropwise. The obtained white soft $Sn(OH)_4$ colloid has been carefully washed with de-ionised water to remove all the contaminants. The final white gel was dried under dynamic vacuum overnight at 110 °C and then hand grinded to obtain the SnO_2 powder. For the S-SnO_2 preparation, SnO_2 was suspended in deionised water and stirred continuously to enhance the water adsorption. After 24 h of vigorous stirring, the water suspension was treated with H_2SO_4 (final concentration 0.5 M) for 30 minutes under stirring. After decantation, the material was filtered and then annealed in air for 3 h at 500 °C.
Both doped and undoped Nafion membranes were prepared following a solution casting procedure. The commercial Nafion solution (5 wt% in water/alcohol, Ion Power Inc. E.W. 1100) was treated with N,N-dimethylacetamide at 80 °C to replace the solvents. When required, inorganic filler powders were added to the Nafion solution and stirred to homogenise the suspension. An optimal additive loading of 5 % with respect to the Nafion polymer weight was chosen for the investigations, in agreement with previous results

obtained by Chen et al., where Nafion membranes with a 5 wt % of sulfated tin oxide showed an optimized proton conductivity with respect to 10 wt %-added and not sulfated SnO_2 membranes [20]. The mixtures were casted on a Petri dish and dry membranes were obtained by solvent evaporation at 90 °C. The casted polymer membrane were successively hot-pressed at 175 °C for 15 min at 10 tons to improve robustness and finally activated and purified by subsequent immersions in boiling hydrogen peroxide (3 vol.%), sulphuric acid (0.5 M) and water. All the investigated membranes have a similar thickness of about 90 μm.

Table 3.3: List of the analysed samples

Sample	Name
SnO_2	F110
Sulfated SnO_2	F110S
Nafion recast	Nafion
Nafion + SnO_2	N-F110
Nafion + sulfated SnO_2	N-F110S

3.4 Experimental methods

3.4.1 Raman spectroscopy

Raman spectra at standard ambient conditions were carried out in backscattering geometry by means of a single monocromator micro-sampling set-up (Horiba-Jobin Yvon, model LabRam HR), or a triple axis monocromator setup (Horiba-Jobin Yvon T64000), both described in chapter 2. All the spectra recorded by the T64000 instrument were excited by the 514.5 nm laser line. The best Raman spectra were obtained by focusing the laser beam through the lens of a long-working distance 50X objective, onto a spot of about 2 μm in size, while the power on the sample surface was kept below 3 mW, in particular for the powders spectra, where an optical filter with OD=1 was used. Due to low laser irradiance power and poor Raman cross-section efficiency of the samples, long integration time was mandatory to obtain spectra with a reasonable signal-to-noise ratio (S/N). In some cases, cyclic scans were carried out from the same sample micro-region and then averaged to improve the S/N. All the spectra were calibrated in frequency using the emission lines of an Ar spectral lamp. Repeated micro-Raman spectra were carried out under the same experimental conditions from different micro regions of the investigated sample to verify their reproducibility over the surface. The recorded

spectra were processed to remove artefacts due to cosmic rays, while the luminescence background was subtracted before starting the analysis of the experimental data.
Spectra at controlled ambient relative humidities (RH) were collected at room temperature with the LABRAM HR instrument. Prior to the measurement, samples were stored in close containers in presence of a saturated salt solution at least for 24 h. The used salts and the corresponding RH values are enlisted in Table 3.4. Samples were then collected from the storage box and quickly moved to an home made sealed measuring chamber (Figure 3.2) in which the same salt solution was present in order to keep the desired RH condition also during the spectra acquisition. All the spectra were

Figure 3.2: Home-made sample holder for Raman measurements at controlled relative humidity condition. The sample spectra were collected trough a thin quartz glass that isolates the sample from the outer atmosphere. A hole under the sample ensured the membrane equilibrium with the inner environment, whose relative humidity is controlled by a saturated salt solution (water in the image).

recorded at least one hour after the sample movement, to allow an eventual re-equilibration of the sample with the environment. For these measurements

Table 3.4: Summary of saturated salt solutions used for the samples conditioning at different RH. Relative humidity values were taken from [21, 22]

Saturated salt solution	RH (%)
LiCl	11
$MgCl_2$	33
$Mg(NO_3)_2$	53
NaCl	75
KNO_3	94
pure H_2O	100

a high precision on the evolution of the peaks position was necessary: to assure this the Raman peaks were fitted with Lorentzian curves and a complex procedure for the calibration of the peaks positions was adopted. In fact,

the low signal intensity did not allow the use of the 1800 lines/mm diffraction grating (with the ulterior signal decrease due to this grating the measurements would last very long) while the 600 lines/mm grating has not the sufficient resolution to define the position of narrow peaks like the Ar lamp emissions with an error under 1 cm^{-1} because the peak width in this case is lower than the instrument resolution.
The solution was to divide the evaluation of the peaks position in two separate steps: previously the absolute position of the 731 cm^{-1} peak of Nafion (the one with the highest intensity) was calibrated with the 1800 lines/mm grating in presence of the Ar lamp for the three samples (no differences were found with filler inclusion and different RH), then the effective Raman spectra were collected with the 600 lines/mm grating. In these last spectra the 731 cm^{-1} peak was fitted and its position was used as an internal reference. Controls were done to be sure that the exposure to the laser beam did not affect the membranes inner humidity: at 100 % RH, the condition more sensible to an eventual dehydration, a set of 5 spectra were subsequently recorded after an exposure time to the laser beam of 40 seconds and then followed by the collection of two spectra lasting 20 minutes (the real measurements time). The SO_3^- peak position, very sensible to the inner humidity, was monitored to detect any eventual change. In this way a control of dehydration process was performed on both short and long irradiation time scales.

3.4.2 Water uptake

The membranes water content at different ambient relative humidities was derived using a room temperature gravimetric method. Samples were kept in close containers in presence of different saturated salt solutions at least for 12 h (for longer conditioning time no weight difference was observed). The salts used are enlisted in Table 3.4. To obtain the dry weight the samples were kept in vacuum overnight. After the conditioning, the membranes were transferred to the balance in a close vessel for the weighing procedure. Multiple spectra were collected for each sample at each RH value in order to verify the procedures repeatability. Water uptake (WU) was calculated according to the following equation:

$$WU = \frac{w_{hum} - w_{dry}}{w_{dry}} \cdot 100$$

where w_{hum} is the membrane weight at the desired RH and w_{dry} is the dry membrane weight.

3.4.3 FT-IR spectroscopy

FT-IR spectra were obtained at room temperature in ATR configuration in the spectral range between 4000 cm^{-1} and 900 cm^1 using a JASCO spectrometer mod. FT/IR-660 plus, described in chapter 2. During the measurements the samples were kept in contact with the flat surface of a Ge crystal. The choice of this material was due to the high refractive index of the SnO_2 powder. The IR spectra were recorded with a resolution of 4 cm^{-1}, using a polystyrene film as a reference. The number of scans for each spectrum were chosen to ensure an optimal signal-to-noise ratio. A proper baseline has been systematically subtracted from all the spectra to get more significant comparison among them.

3.5 Results: SnO_2 and SnO_2-S powders

3.5.1 Raman spectra

The spectral properties of the synthesised nanopowders were compared with a commercially available nano-sized powder, nominally in rutile phase (Sigma-Aldrich, product n.549657) taken as reference, using both Raman instruments to cover a wavenumber range from 80 to over 1500 cm^{-1} (spectra recorded by LABRAM in Fig.3.3 and by T64000 in Fig.3.4). Focusing on Fig. 3.3, in the commercial powder spectrum (botton panel) are clearly visible all the three rutile modes expected in this wavenumber range, at 474, 636 and 774 cm^{-1}, together with a broader band with relatively low intensity, peaked at about 560 cm^1, observed in literature [24] and ascribed to the combination of various modes such as an amorphous SnO_2 mode and an amorphous tin (IV) hydrous oxide Raman band.
The spectra of the F110 and F110S samples, reported in the middle and upper panels of Figure 3.3, show only two of the characteristic bands of the tetragonal rutile SnO_2 (at 474 cm^{-1} and 632 cm^{-1}). These are overimposed to a band centred at about 560 cm^{-1}, much stronger than in the commercial powder, which probably hides the missing SnO_2 peak at 774 cm^{-1} and suggests the presence of a larger amount of amorphous phase. In addition, the two spectra display other common bands of unknown origin at about 310 cm^{-1}, 698 cm^{-1}, 752 cm^{-1} and 1000 cm^{-1}, probably originated by the presence of impurities in the F110 powder.
Finally, the sulfated sample also displays three additional peaks at about 978 cm^{-1}, 1039 cm^{-1} and 1131 cm^{-1}, which are characteristic vibrational modes of the sulphate (SO_4^{2-}) group [16]. In particular, the peak at 978 cm^{-1} is due to the SO_4^{2-} intramolecular normal mode ν_1 (symmetric stretching), while

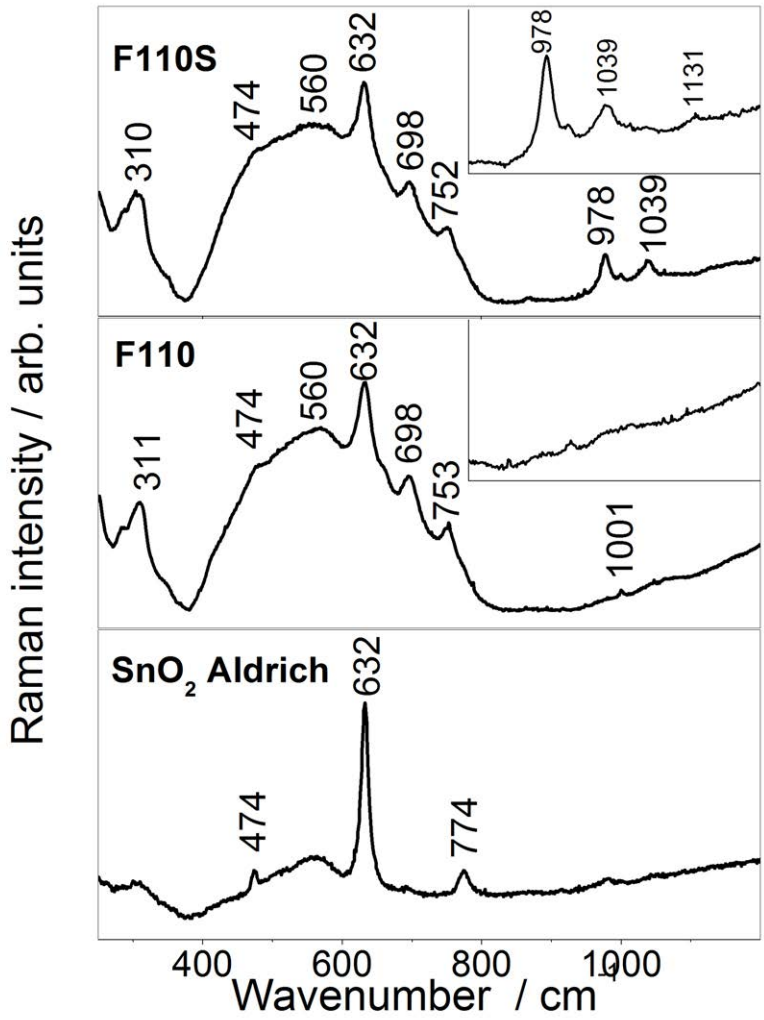

Figure 3.3: Unpolarised micro-Raman spectra recorded from the commercial SnO_2 powder (bottom panel), and from the samples F110 (mid panel) and F110S (top panel). From [23]

the two peaks at 1039 cm^{-1} and 1131 cm^{-1} are due to the splitting of the ν_3 mode (asymmetric stretching) [25]. The ν_3 mode splitting into two different peaks suggests a sulfate monodentate coordination, even if a confirmation is needed by IR spectroscopy, a technique where these peaks are more visible.

In the low wavenumbers region (Fig 3.4) the comparison between the commercial powder and the F110 and F110S samples reveals another difference: two additional peaks are present in the laboratory-synthesized samples, at 112 and 211 cm^{-1}, highlighting a SnO phase inside the SnO_2 powder. In Fig 3.4 the spectrum of commercial SnO powder has been added as a comparison. In the calcined sample (F110S) the SnO presence is lower, as it is expected

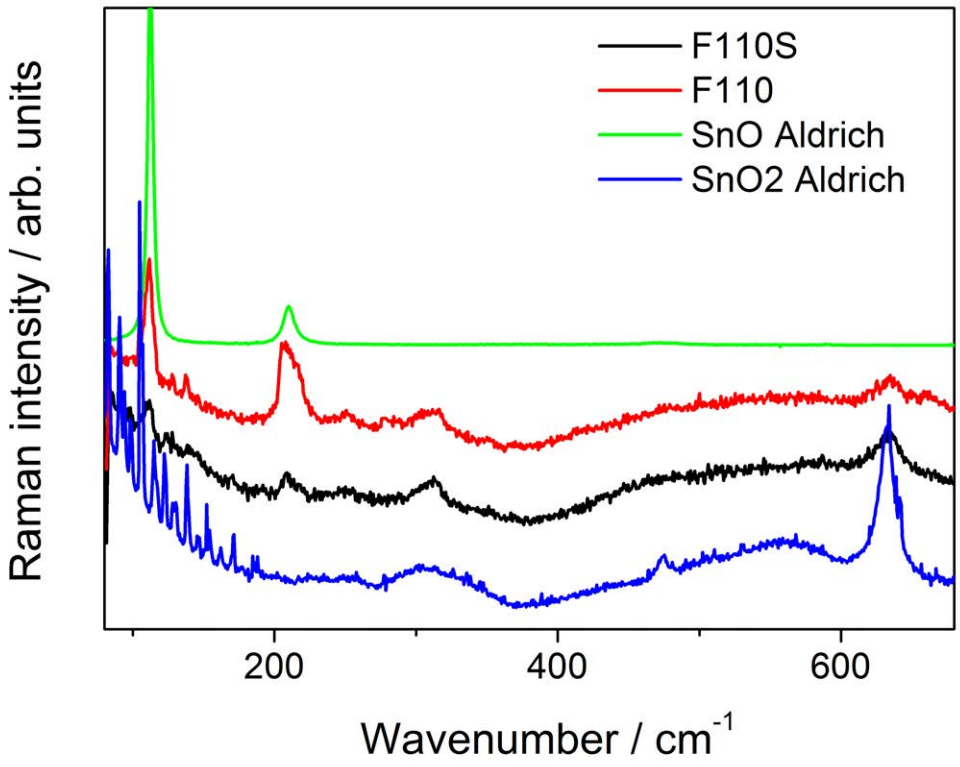

Figure 3.4: Raman spectra at low wavenumbers of F100 (red) and F100S (black) samples, compared to commercial SnO_2 (blue) and SnO (green) powders.The narrow lines under 200 cm^1 in the commercial SnO_2 are due to air vibrations.

being the SnO_2 phase the one stabilized at high temperature.
To investigate a possible SnO source a control was done on the precursor materials. As described in the material synthesis section the powder was obtained from $SnCl_4$: if this was not pure, but contained also $SnCl_2$, this could have caused the SnO formation. In Fig 3.5 the spectrum of the $SnCl_4$ precursor (in red) was compared with the spectrum of a commercial $SnCl_2$: the former shows all the principal peaks listed in literature [26], and none of the $SnCl_2$ peaks, thus confirming the substance purity. It is evident that the SnO presence shoud not be attributed to the precursor, but to another, and still not defined, source.

3.5.2 Infrared spectra

FT-IR spectra of F110 and F110S samples are reported in Fig 3.6 together with the one of a commercial SnO_2. Due to the use of the ATR technique with a Ge crystal, the lower measurable wavenumber is around 900 cm^{-1} (Germanium adsorbs too much radiation below this wavenumber value). This did not al-

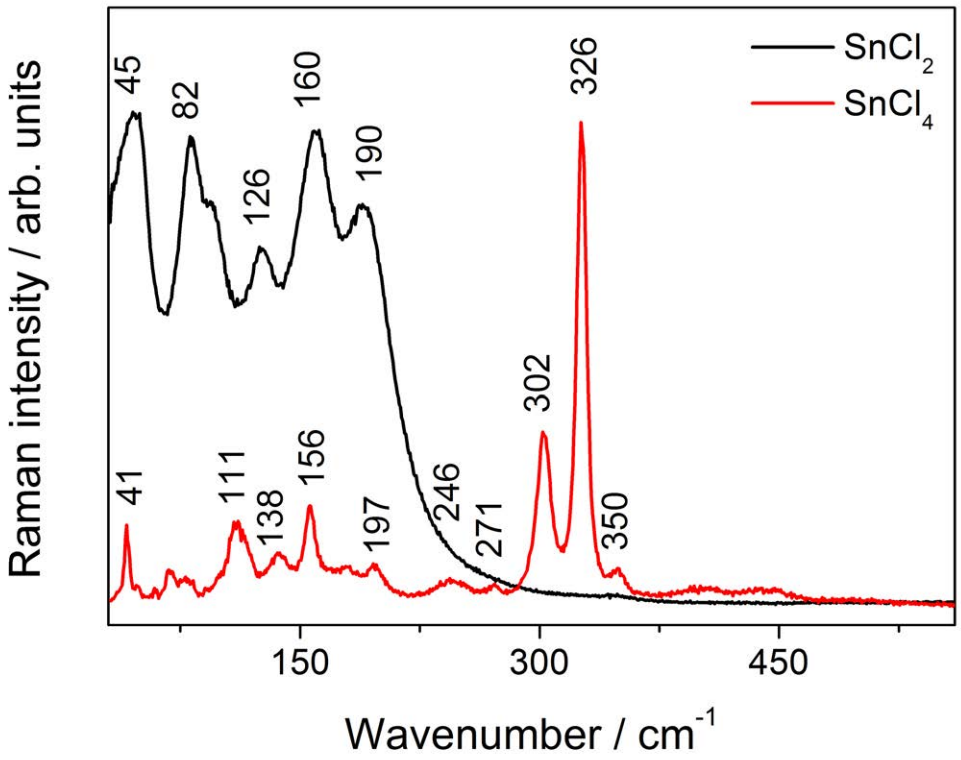

Figure 3.5: Raman spectrum of the $SnCl_4$ precursor (red) compared to the spectrum of $SnCl_2$ (black).

low the direct observation of the SnO_2 peaks, but the analysis of the sulfate vibrations region was still possible.
The obtained spectra confirm the Raman results: as expected no peaks are observed in the analysed zone for the pure SnO_2 powders (both commercial and laboratory-synthesized) while three peaks are present in the sulfated sample. The confirmed presence of the 1135 cm^{-1} peak and the absence of a fourth one confirmed that the ν_3 mode is doubly split, implying the monodentate coordination of the sulfate. For a better understanding of the role of the sulfate coordination on the ν_3 splitting a list of the ν_1 and ν_3 infrared peaks is presented in Table 3.5 for all the sulfate possible coordinations. In particular, the isolated SO_4^{2-} ion has a T_d symmetry, and only one peak, threefold degenerate, at about 1100 cm^{-1} while the monodentate coordination change the ion symmetry, that became C_{3v}, thus causing the occurrence of one peak at about 1040 cm^{-1} and one twofold degenerate peak at about 1135 cm^{-1}, as in the present study. If the coordination is bidentate the symmetry change again to C_{2v}, giving raise to three different peaks (not degenerate) for the ν_3 modes.

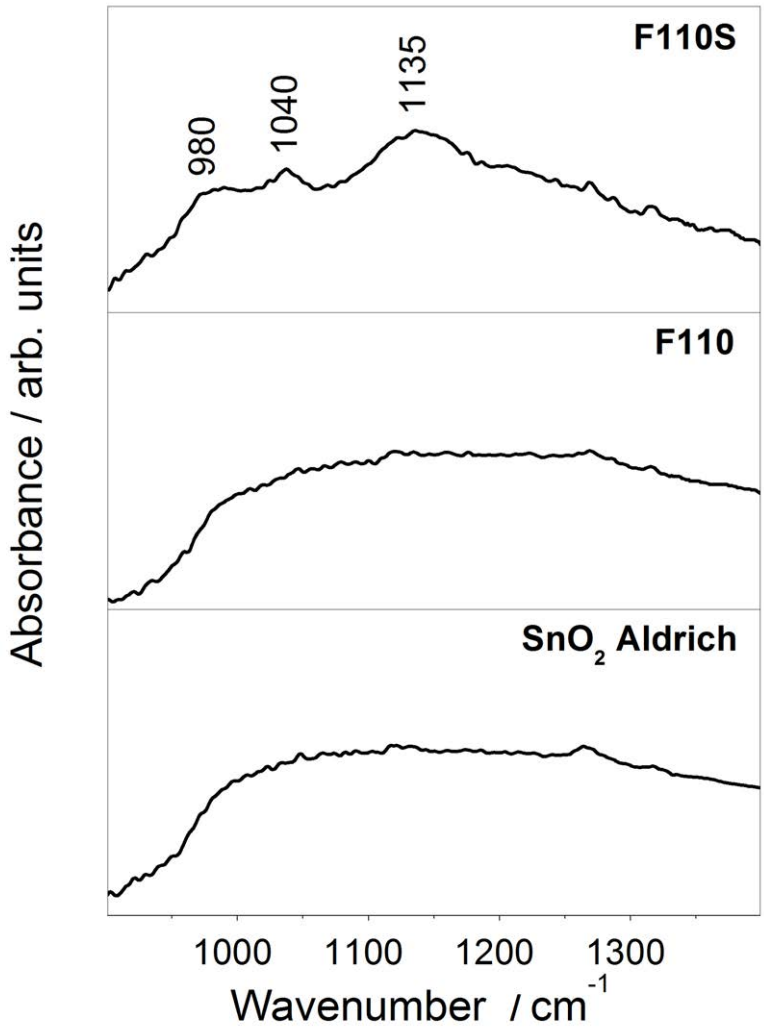

Figure 3.6: ATR spectra recorded in the spectral range between 900 cm^1 and 1400 cm^1 from the commercial SnO_2 powder (bottom panel) and from the samples F110 (mid panel) and F110S (top panel) [23].

3.6 Results: composite membranes

3.6.1 Raman spectra

As obtained Nafion membranes, both pure and composite, showed a high luminescence that resulted in a difficult acquisition of the Raman signal. Due to this, all the membranes were preliminary subjected to the so-called re-activation process, that consisted in a subsequent immersion in boiling hydrogen peroxide (3%), sulphuric acid (0.5 M) and water for about 30 minutes each step. After this treatment the luminescence, though still present, was

Table 3.5: Sulfate ion modes splitting with different coordination, (Co(III) composites). From [27]

	Symmetry	ν_1 frequency	ν_3 frequency
free SO_4^{2-} ion	Td	not visible	1100
monodentate	C_{3v}	970	1032-1044 1117-1143
bidentate	C_{2v}	995	1050 - 1060 1170 1105

quenched to acceptable levels.

In Figure 3.7 the Raman spectra of pure Nafion membrane (Nafion recast), Nafion with F110 (N-F110) and Nafion with F110S (N-F110S) are shown, recorded at standard ambient conditions. All the characteristic bands of Nafion expected in the measured wavenumbers range can be observed for all the samples: at about 292 cm^{-1} [t(CF_2)], 310 cm^{-1} [t(CF_2)], 385 cm^{-1} [δ(CF_2)], 570 cm^{-1} [δ(CF_2)], 730 cm^{-1} [v_s(CF_2)], 805 cm^{-1} [v(CS)], 970 cm^{-1} [v_s(CS)], 1058 cm^{-1} [$v_s(SO_3^-)$], 1210 cm^{-1} [v_{as}(CF_2)], 1297 cm^{-1} [v(CC)] and 1380 cm^{-1} [v_s (CC)].

Both N-F110 and N-F110S show a more complex spectrum with respect to recast Nafion resulting from the superposition of the Nafion membrane spectrum with that of the nanosized SnO_2 powder. The presence of tetragonal rutile SnO_2 in the two composite samples, both in crystalline and in amorphous phases, is confirmed by the two peaks at 632 cm^{-1} and 474 cm^{-1} (this last hardly observable) overlapping the broad band at about 560 cm^{-1}. Apparently no new Raman mode is observed, which could suggest a chemical interaction between the filler and the host matrix. Spectra collected from different points in N-F110 and N-F110S samples revealed that the intensity of the SnO_2 peak at 632 cm^{-1} is on average slightly higher for the sulfate sample, implying a probably higher filler concentration.

The low wavenumber spectra (Figure 3.8) evidence the presence of the impurity peaks (at 696 and 750 cm^{-1}) also after the F110 and F110S inclusion into the membrane, and the persistence of the SnO phase (111 and 209 cm^{-1} peaks).

Surprisingly, no evidence of spectral features related to the sulphate group is found in N-F110S. In order to understand if the absence of the sulfate peaks in the N-F110S sample was due to a low Raman signal or to an effective absence of sulfate group after the powder inclusion, an ulterior analysis was done by means of Energy Dispersive X-Ray technique (EDX). The relative ra-

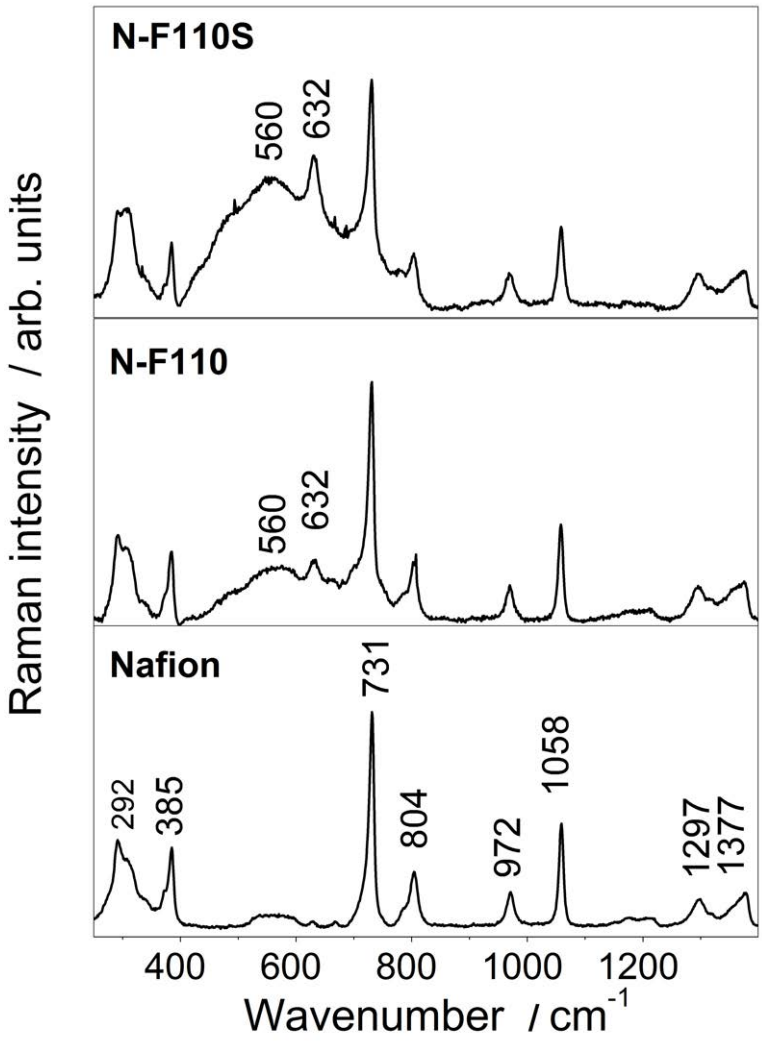

Figure 3.7: Raman spectra of pure Nafion (lower panel), N-F110 (middle panel) and N-F110S (upper panel) measured with the LABRAM instrument.

tios between sulfur (always presents in Nafion and, for N-F110S, in the filler) and fluorine (presents only in Nafion) for the three analysed membrane are shown in Table 3.6. The obtained values evidence that no excess sulfur is

Table 3.6: Sulfur to Fluorine ratio, from EDX data

Sample	S/F ratio
Pure Nafion	0.025
N-F110	0.025
N-F110S	0.023

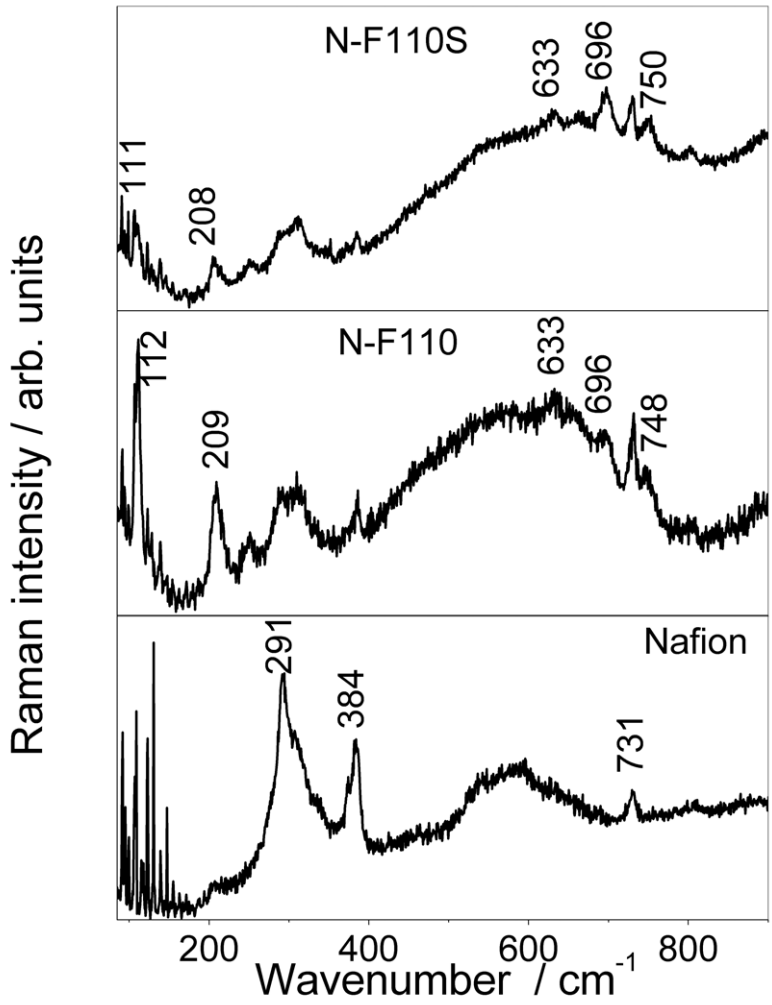

Figure 3.8: Raman spectra of pure Nafion (lower panel), N-F110 (middle panel) and N-F110S (upper panel) measured with the T64000 instrument in the low wavenumbers range.

found in the membrane with sulfated tin oxide: this mean that when the sulfated powder is included into the membrane almost all the functionalization is lost, and what remains is almost only tin oxide. Moreover, the EDX analysis confirm the slightly higher Sn concentration in the N-F110s sample (relative to the fluorine percentage, the exact absolute concentration is unknown due to the lack of a standard for the Sn), as already observed with Raman spectroscopy. Up to now, no other effort were made to obtain a membrane with a more stable sulfate functionalization. Even if the powder functionalization in N-F110S is mainly lost, the N-F110 and N-F110S electrical properties are not the same. Both show better ex-situ conductions and fuel cell performances than pure Nafion, but the formally sulfated sample is the best. Two proba-

ble explanations can be given: the powder retains a small amount of sulfate groups, not detectable with EDX or Raman but still effective for the membrane conduction improvement, or the slightly higher SnO_2 content in this sample is better for the membrane performances (the 5 % loading was chosen because gave better results than 10% in [20], but no intermediate value has been investigated yet).

3.6.1.1 Raman spectra at different ambient relative humidity

As already explained, one of the more critical properties of a Nafion membrane, composite or not, is the water retention capacity, especially at low RH. As a matter of fact, the main point in the inclusion of a metal oxide is the increasing of this capacity. Due to this, the investigation of the membranes behaviour at various ambient relative humidity is of extreme interest.
With Raman spectroscopy the main difference observed in pure Nafion spectrum changing the RH (established that the direct observation of the water bands is not always possible for their weak Raman intensities), were the energy and the intensity of the peak attributed to the SO_3^- vibration at about 1058 cm^{-1}. In particular, an increase in the peak energy and a lower peak area were detected with decreasing humidity [28]. These changes were explained with the different environment in the proximity of the SO_3^- groups at different water content: in dry conditions the S-O dipole is strongly polarized by the electrostatic field of the H^+ counter ion, while with increasing relative humidity the growing number of water molecules shield the SO_3^- ion [29, 30]. The interaction with the bare H^+ change also the dipole polarizability, and thus the Raman peak area.
Raman spectroscopy is therefore an important tool to analyse the effective environment present near the Nafion side chain at various RH, and an interesting question is: what happen to the SO_3^- peak (and thus to the SO_3^- environment) in presence of a filler?
To the best of our knowledge a similar study, here presented, has never been done before. For this analysis the Raman spectra were obtained from at least four different points on the membranes surface for each RH value. The powder spectral contribution was then subtracted from the composite membrane spectra (the subtraction effect is shown in Figure 3.9) to allow a better estimation of the peak position and intensity. All the remaining peaks were fitted with Lorentzian curves and the calibration procedure described in the experimental section was applied. The SO_3^- peak of the three membranes at 11, 53, 75 and 100 % RH are presented in Figure 3.10, while the resume of the peak positions at all the explored RH is shown in Figure 3.11. The error bars in Figure 3.11 and 3.12 represent the calculated standard deviations.

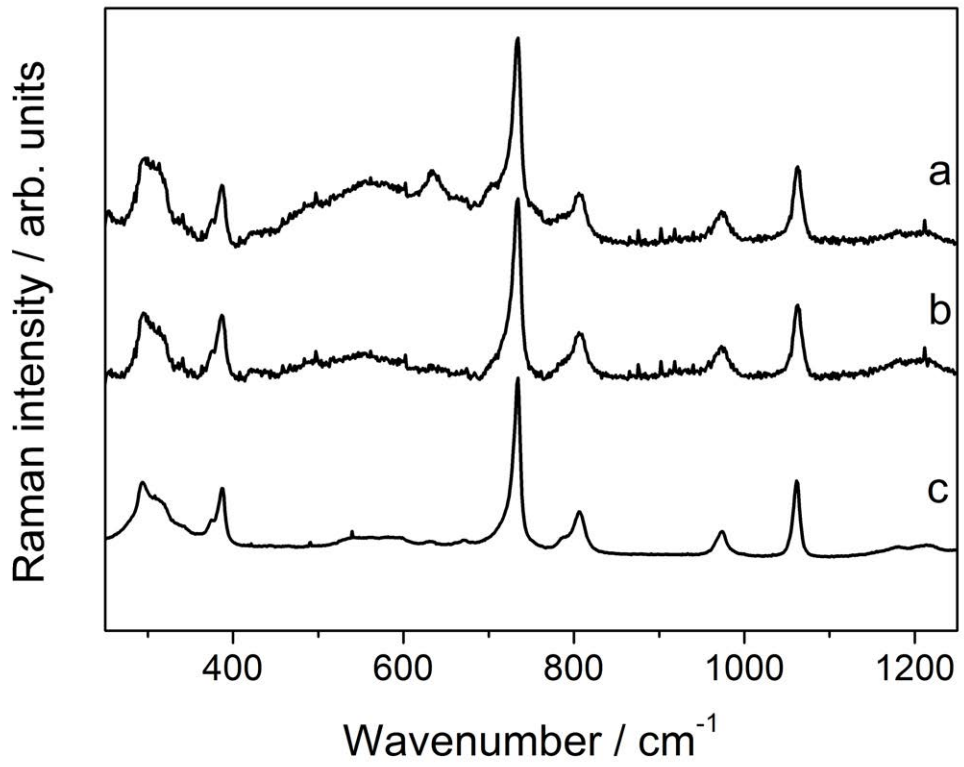

Figure 3.9: Spectrum of N-F110S sample before (a) and after (b) the F110S spectrum subtraction, compared to c) pure Nafion

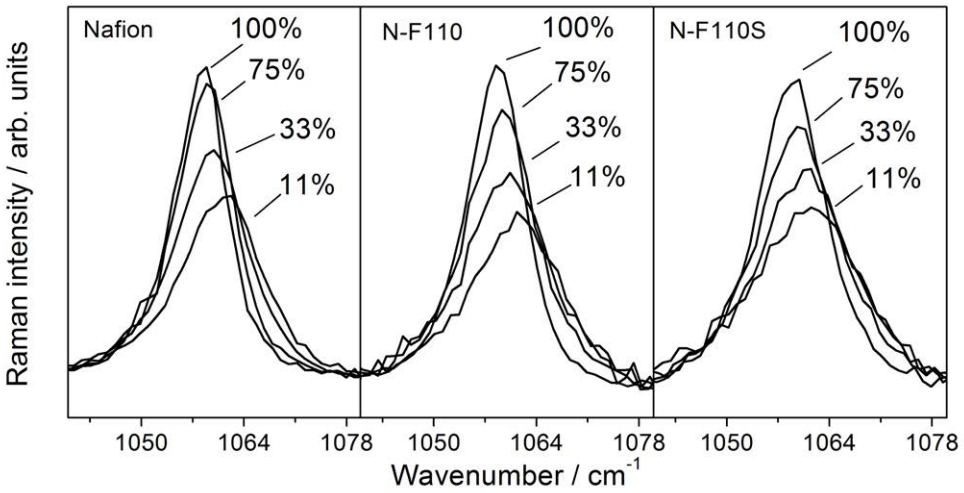

Figure 3.10: SO_3^- peak at 11, 53, 75 and 100 % RH for the three samples analysed.

The trend in the peak shift for pure Nafion is similar to the one already reported in literature: a greater shift in the peak position is observed at low RH

than at high RH for an equal change in relative humidity. The behaviour is different for the composite membranes. In particular, N-F110 has peak positions similar to the pure Nafion at low RH but shows a divergence at high RH: the peak energy seems to reach a stable value, higher than in pure Nafion, until an abrupt shift toward lower energies occurred near 100 % RH. The same is observed for N-F110S, even if amplified: the peak position diverges from the Nafion one already at 33 % RH.

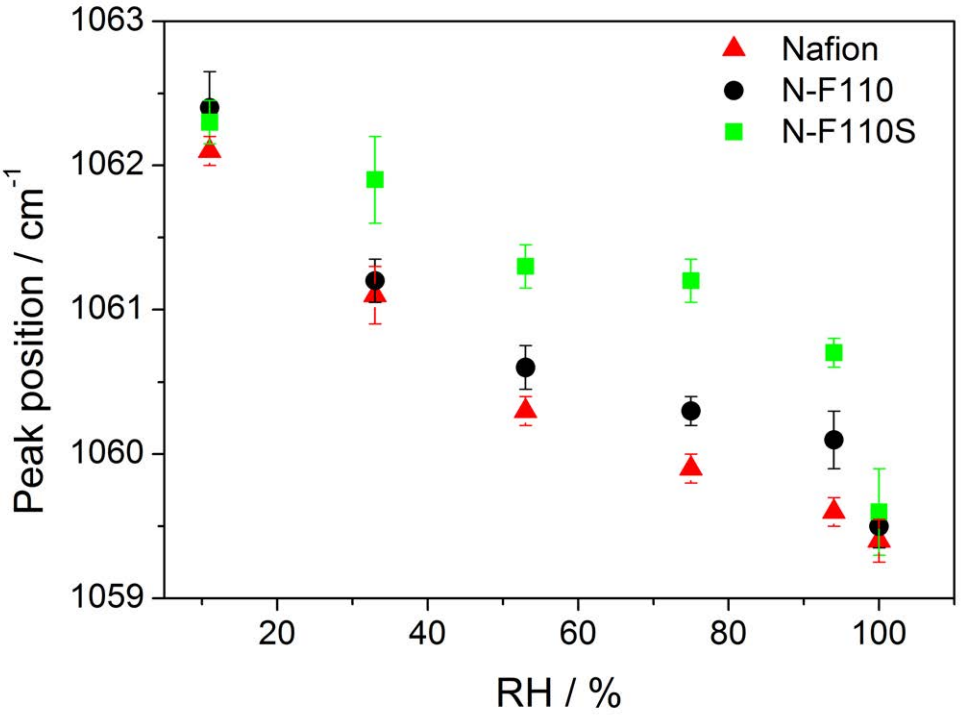

Figure 3.11: SO_3^- peak positions vs ambient relative humidity for pure Nafion (red), N-F110 (black) and N-F110S (green).

As explained before, the peak energy directly depends on the S-O dipole electrostatic interaction with the counterions, and a change in the position at equal RH means a difference in the SO_3^- perturbation, that can occurs in two way: a different water content, that results in a different shielding effect, or a direct modification of the electric charge responsible for the SO_3^- perturbation. This latter motivation was given in literature to explain the modification in the SO_3^- peak position observed in ion-exchanged Nafion: if the H^+ was substituted with a heavier cation (Li^+, Na^+, K^+ and Rb^+) the peak energy at low RH was found at lower value then in Nafion - H^+ (with values progressively more similar to the free SO_3^- for heavier cations), while no particular differences were observed at high RH [30]. The difference in

the SO_3^- perturbation at low RH was imputed to the lower net charge of the bigger cations compared with the smaller H^+, while at high RH the water molecules shielded the cation both in the Nafion - H^+ and in the Nafion-exchanged, erasing the differences. An important point here is that similar energy value at high RH does not always mean equal quantity of shielding water. In fact, if the SO_3^- is less perturbed, like in the Nafion-exchanged case, potentially less water is needed to shield the lower electrostatic field present and obtain an almost free SO_3^-. This is precisely what happened: water uptake measurements revealed that Nafion exchanged with heavier cations adsorb less water [31], but clearly this water is sufficient to completely shield the S-O dipole and have vibrational energy at high RH similar to the pure Nafion one.

Returning to the N-F110 and N-F110S samples, the position identical to the

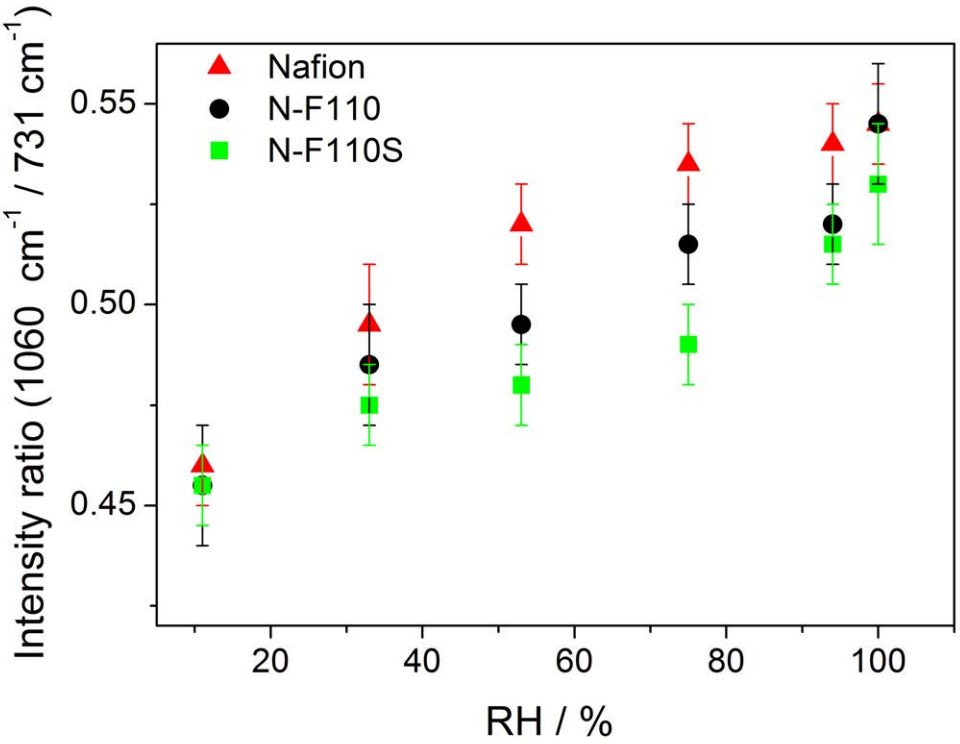

Figure 3.12: SO_3^- peak intensity vs ambient relative humidity for pure Nafion (red), N-F110 (black) and N-F110S (green).

pure Nafion case observed at low relative humidity suggests that the electrostatic field responsible for the SO_3^- perturbation is the same in the three samples, and the filler presence does not change the net charge experienced by the sulfonic groups. If the net perturbation is the same at low RH, where the effect of an eventual charge difference has to be maximum, it is reason-

ably to expect the same at higher RH, where additional shielding water is present. Due to this, the differences observed in the composite samples at high RH can only be attributed to a lower water quantity, that less screen the SO_3^- from the counterions field with respect to the pure Nafion. A question now arises: is the lower water content global or just local? Water uptake measurements were made to answer to this question.
As regards the more pronounced deviation occurring in N-F110S, the explanation can be the retention of a small amount of sulfate groups on the nanopowder surface that also interacts with the surrounding water, or the slightly higher SnO_2 content found in this sample.
A confirmation of the trend observed in the peak positions come from the peak intensities (Figure 3.12), calculated as ratio between the SO_3^- peak and the Nafion peak at 731 cm^{-1}. In this case the pure Nafion peak intensity, as assessed in literature, has a behaviour that is somehow opposite to the peak position one: the area increases with the RH value, but the greater changes are still in the low RH range. Again, the composite membranes show a different trend, especially at high RH, similar to the one observed for the peak energy. The area is strongly dependent on the chosen background and to the powder spectrum subtraction, while the position is dependent on the calibration procedure: obtaining the same trend with both is an important check for the correctness of the spectra analysis.

3.6.2 Water uptake

In general, the water sorption of pure Nafion as a function of the ambient relative humidity shows two different behaviour: at low RH the plot is characterized by a small increase in water uptake until a value of about 5 to 6 H_2O per SO_3H, above which the increase is considerably greater and the membranes start to swell. This results can be explained in terms of a condition of tightly bound, SO_3H-associated water in the initial stage of hydration followed by the addition of more loosely bound water in the latter stage [32, 33, 34].
The Nafion water uptake curve measured in this study (Figure 3.13) perfectly resembles the curves obtained in literature. Comparing the values for Nafion, N-F110 and N-F110S samples no great difference catches the eye and only slightly higher values were found for the N-F110 at high RH, but inside the measurement errors. What are clearly not present are the differences observed for the SO_3^- peak with Raman spectroscopy at high RH. These have in theory to be even more visible, not occurring in a plateaux zone, like in Raman, but in the zone of major curve slope.
From this absence, it is possible to say that the difference in shielding water found with Raman spectroscopy does not depends on a lower general water

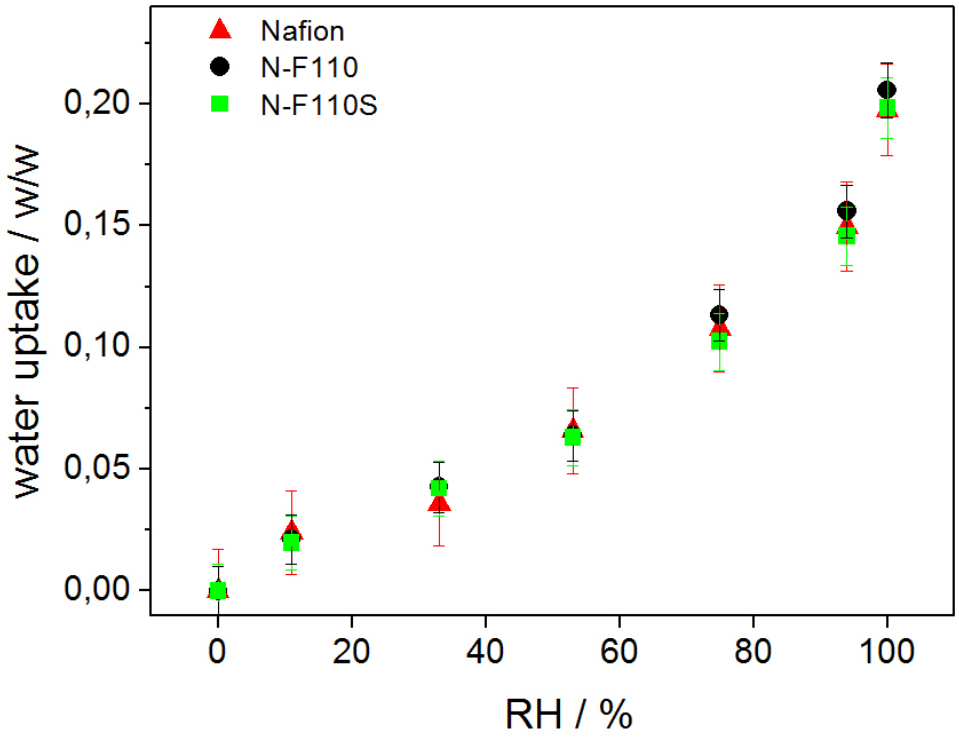

Figure 3.13: Water uptake vs ambient relative humidity for pure Nafion (red), N-F110 (black) and N-F110S (green).

content, but on a not homogeneous water distribution inside the membrane, with a lower water amount only in the proximity of the sulfonate ions, and necessarily a higher water amount (compared to pure Nafion) in the proximity of the powder. In fact, having the composite membrane a SO_3^- density necessarily inferior than pure Nafion due to the presence inside the polymer matrix of the nanopowder, an homogeneous water distribution and an equal quantity of water at a given RH have to mean a number of water molecule for each SO_3^- even higher for the composite membrane that in pure Nafion, in complete disagreement with the Raman results, that can thus only be explained by a not homogeneous water distribution.

3.6.3 Infrared spectra

Infrared analysis of the samples were also carried out. The analysis of the composite membranes was not easy to perform: the relative high thickness of the membranes does not allow the use of the transmission technique, forcing the use of ATR. Moreover, due to the high samples refractive index, it was possible to use only the Ge crystal, with a strong limitation on the light

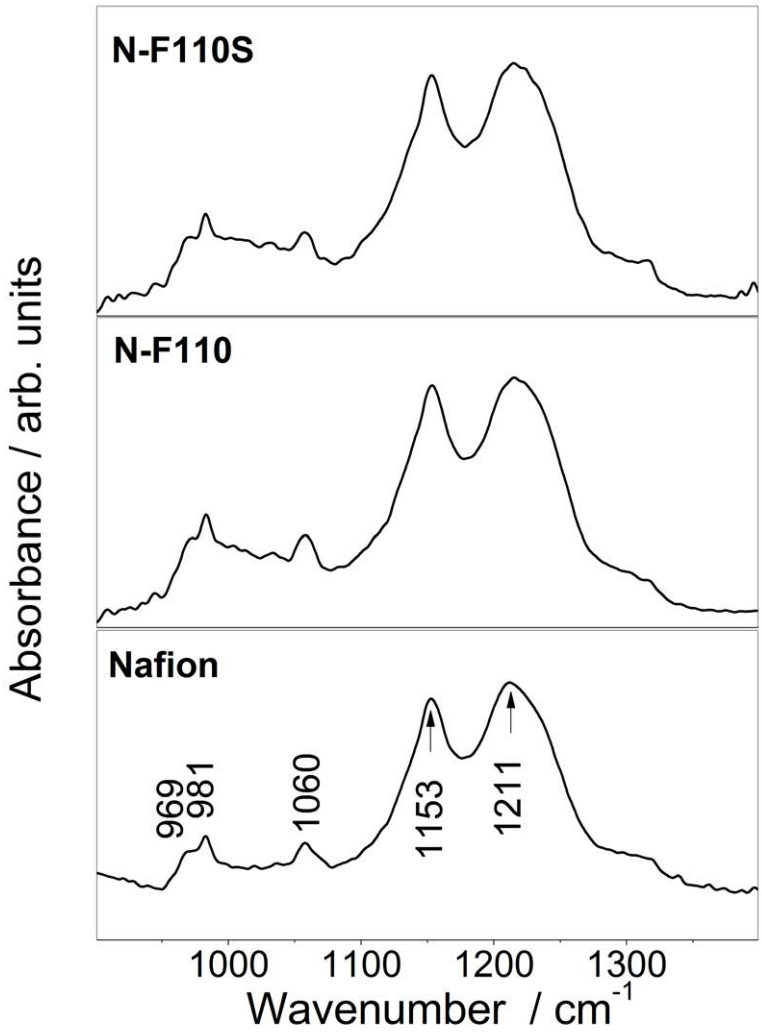

Figure 3.14: FT-IR ATR spectra of pure Nafion (lower panel), N-F110 (middle panel) and N-F110S (upper panel).

penetration inside the membranes and a consequent very low light absorption. The signal was even lower if the membranes were not completely wet, probably for a beneficial effect of the water on the sample adhesion on the crystal. However, FT-IR spectra of the three samples were made with membranes fully hydrated: the expected vibrational peaks were found in the pure Nafion spectrum (at 969, 981, 1060, 1153 and 1211 cm^{-1}), and no differences were observed for the composite samples, confirming the low interaction between the filler and the Nafion matrix as assessed by Raman spectroscopy. The presence of sulfate groups in N-F110S could not be investigated with this technique, because of the more intense C-F_2 peaks in the same region that would hide eventual sulfate vibration peaks.

Infrared spectroscopy has a great potential for the study of the water state inside a polymer at different RH due to the high intensity of the water bands, but such a study was not possible, due to the already mentioned low signal of the membranes. For the same reason, the study of the SO_3^- position at various ambient relative humidity, complementary to the Raman one, was also not possible.

3.7 Conclusion

A complementary study with both Raman and FT-IR spectroscopy was performed on bare F110 and F110S fillers and on composite Nafion membranes. As regard the Raman spectra of the fillers, the characteristic SnO_2 peaks were observed in both F110 and F110S alongside with peaks corresponding to an SnO phase and a broad band centred at 560 cm^{-1} due to the presence of an amorphous phase. In F110S sample the functionalization with sulfated groups was confirmed by the observation of the SO_4^{2-} vibrational peaks in the spectral range between 970 and 1135 cm^{-1}. FT-IR spectroscopy confirmed the presence of three peaks in this range and thus the monodentate coordination of the SO_4^{2-} groups. The composite membranes spectra obtained with Raman technique showed all the unmodified Nafion peaks with the addition of the filler features, even if no sign of the sulfate peaks were found in the N-F110S sample. An additional analysis by means of EDX technique displayed that no significant increase in the amount of sulfur was present in this sample, suggesting a possible detachment of the functionalization from the powder during the inclusion in Nafion. A detailed Raman analysis at different ambient relative humidity on the SO_3^- peak position and intensity revealed important divergences between pure Nafion and composite membranes, and in combination with water uptake measurements highlighted a different water distribution inside the membrane due to the filler presence.
This results underline how the prevision of the effects of a metal oxide inclusion like SnO_2 inside the Nafion matrix is not straight forward. SnO_2 was included basically to increase the membrane water uptake, but what happen in reality is more complicated: no great changes were observed at low RH, while at high RH an effective increase in the water content near the powder is counterbalanced by a lower hydration near the sulfonate ions. Only at really high RH (close to 100%) the SO_3^- peak position returns to similar value for all the three samples. The reason of this behaviour, probably due to a saturation of the filler that allows the last adsorbed water to hydrate the SO_3^- zone, has still to be investigated.

Bibliography

[1] K. Momma and F. Izumi, "Vesta 3 for three-dimensional visualization of crystal, volumetric and morphology data," *J. Appl. Crystallogr.*, vol. 44, pp. 1272–1276, 2011.

[2] P. Merle, J. Pascual, J. Camassel, and H. Mathieu, "Uniaxial-stress dependence of the first-order raman spectrum of rutile. i. experiments," no. 21, pp. 1617–1626, 1980.

[3] R. Katiyar, P. Dawson, M. Hargreaves, and G. Wilkinson, "Dynamics of the rutile structure. iii. lattice dynamics, infrared and raman spectra of SnO_2," no. 4, pp. 2421–2431, 1971.

[4] R. Summitt, "Infrared absorption in single-crystal stannic oxide: Optical lattice-vibration modes," no. 39, pp. 3762–3767, 1968.

[5] D. Rousseau, R. Bauman, and S. Porto, "Normal mode determination in crystals," no. 10, pp. 253–290, 1981.

[6] J. Geurts, S. Rau, W. Richter, and F. Scmitte, "SnO films and their oxidation to SnO_2: Raman scattering, ir reflectivity and x-ray diffraction studies," no. 121, pp. 217–225, 1984.

[7] Y. Li, Y. Li, L. Zhang, Y. Ma, and G. Zou, "The pressure-induced phase transition in SnO: a first-principles study," no. 19, p. 425230, 2007.

[8] X. Wang, F. Zhang, I. Loa, K. Syassen, M. Hanfland, and Y. Mathis, "Structural properties, infrared reflectivity, and raman modes of SnO at high pressure," no. 241, pp. 3168–3178, 2004.

[9] I. Gontia, M. Baibarac, and I. Baltog, "Photoluminescence and raman studies on tin dioxide powder and tin dioxide/single-walled carbon-nanotube composites," no. 248, pp. 1494–1498, 2011.

[10] S. Sun, G. Meng, G. Zhang, T. Gao, B. Geng, L. Zhang, and J. Zuo, "Raman scattering study of rutile SnO_2 nanobelts synthesized by thermal evaporation of sn powders," no. 376, pp. 103–107, 2003.

[11] K. Vijayarangamuthu and S. Rath, "Nanoparticle size, oxidation state, and sensing response of tin oxide nanopowders using raman spectroscopy," no. 610, pp. 706–712, 2014.

[12] G. Zerbi and M. Sacchi, "Dynamics of polymers as structurally disordered systems. vibrational spectrum and structure of poly(tetrafluoroethy1ene)," no. 6, pp. 692–699, 1973.

[13] K. Kunimatsu, B. Bae, K. Miyatake, H. Uchida, and M. Watanabe, "Atr-ftir study of water in Nafion membrane combined with proton conductivity measurements during hydration/dehydration cycle," no. 115, pp. 4315–4321, 2011.

[14] A. Gruger, A. Rgis, T. Schmatko, and P. Colomban, "Nanostructure of Nafion membranes at different states of hydration: An ir and raman study," no. 26, p. 215225, 2001.

[15] G. Zundel, *Hydration and Intermolecular Interaction*. 1969.

[16] M. Leuchs and G. Zundel, "Easily polarizable hydrogen bonds in aqueous solutions of acids. perchloric acid and trifluoromethane sulphonic acid," no. 74, pp. 2256–2267, 1978.

[17] M. Falk, "An infrared study of water in perfluorosulfonate (Nafion) membranes," no. 58, pp. 1496–1501, 1980.

[18] C. Heitner-Wirguin, "Infrared spectra of perfluorinated cation-exchanged membranes," no. 20, pp. 371–377, 1979.

[19] R. Scipioni, D.Gazzoli, F.Teocoli, O. P. A. Paolone, N. I. S. Brutti, and M. Navarra, "Preparation and characterization of nanocomposite polymer membranes containingfunctionalized SnO_2 additives," no. 4, pp. 123–142, 2014.

[20] F.Chen, B. Mecheri, A. D'Epifanio, E. Traversa, and S. Licoccia, "Development of Nafion/tin oxide composite mea for dmfc applications," no. 10, pp. 790–797, 2010.

[21] L. Greenspan, "Humidity fixed points of binary saturated aqueous solutions," no. 81A, pp. 89–95, 1977.

[22] A. Schneider, "Neue diagramme zur bestimmung der relativen luftfeuchtigkeit über gesättigten wässerigen salzlösungen und wässerigen schwefelsäurelösungen bei verschiedenen temperaturen," no. 18, pp. 269–272, 1960.

[23] S. Brutti, R. Scipioni, M. Navarra, S. Panero, V. Allodi, M. Giarola, and G. Mariotto, "SnO_2-Nafion nanocomposite polymer electrolytes for fuel cell applications," no. 11, pp. 882–896, 2014.

[24] K. Vijayarangamuthu and S. Rath, "Nanoparticle size, oxidation state, and sensing response of tin oxide nanopowders using raman spectroscopy," no. 610, pp. 706–712, 2014.

[25] D. Stoilova and V. Koleva, "Structural distortion of matrix-isolated SO_4^{2-} guest ions in selenate crystal hydrates $MeSeO_4$ nH_2O (me = Mg, Mn, Co, Ni, Cu, Zn, n = 6, 5, 4)," no. 613, pp. 137–144, 2002.

[26] A. Shihada, A. S. Abushamleh, and F. Weller, "Crystal structures and Raman spectra of cis-$SnCl_4(H_2O)_2 \cdot 2H_2O$, cis-$(SnCl_4(H_2O)_2) \cdot 3H_2O$, $(Sn_2Cl_6(OH)_2(H_2O)_2) \cdot 4H_2O$, and (hl)$(SnCl_5(H_2O)) \cdot 2{,}5H_2O$(l=3-acetyl-5-benzyl-1-phenyl-4,5-dihydro-1,2,4-triazine-6-one oxime, $C_{18}H_{18}N_4O_2$)," no. 630, pp. 841–847, 2004.

[27] K. Nakamoto, *Infrared and Raman Spectra of Inorganic and Coordination Compounds*. 1986.

[28] M. Hara, J. Inukai, K. Miyatake, H. Uchida, and M. Watanabe, "Temperature dependence of the water distribution inside a Nafion membrane in an operating polymer electrolyte fuel cell. a micro-raman study," no. 58, p. 449455, 2011.

[29] K. Kunimatzu, B. Bae, K. Miyatake, and M. W. H. Uchida, "Atr-ftir study of water in Nafion membrane combined with proton conductivity measurements during hydration/dehydration cycle," no. 115, pp. 4315–4321, 2011.

[30] M. Falk, "Infraredspectra of perfluorosulfonated polymer and of water in perfluorosulfonated polymer," in *Perfluorinated Ionomer Membranes* (A. E. et al, ed.), pp. 139–170, American Chemical Society, 1982.

[31] N. Jalani and R. Datta, "The effect of equivalent weight, temperature, cationic forms, sorbates, and nanoinorganic additives on the sorption behavior of Nafion," no. 264, pp. 167–175, 2005.

[32] K. A. Mauritz and R. B. Moore, "State of understanding of Nafion," no. 104, pp. 4535–4585, 2004.

[33] R. Duplessix, M. Escoubes, B. Rodmacq, F. Volino, E. Roche, A. Eisenberg, and M. Pineri, "Water absorption in acid Nafion membranes," in *Water in Polymers* (S. P. Rowland, ed.), pp. 469–486, American Chemical Society, 1980.

[34] T. A. Z. Jr., M. Neeman, L. O. Sillerud, and S. Gottesfeld, "Determination of water diffusion coefficients in perfluorosulfonate ionomeric membranes," no. 95, pp. 6040–6044, 1991.

Chapter 4

Composite Nafion with S-TiO_2 as filler

4.1 Titanium dioxides vibrational properties

TiO_2 vibrational spectrum depends on the type of titania polymorph: each one in fact has a different crystal symmetry or number of molecules per unit cell, thus meaning a different number of vibrational active modes for each structure. In this section, only the four main titania polymorphs will be analysed: anatase, rutile, brookite and TiO_2-B, with crystal structures shown in Figure 4.1.
Rutile crystal has a D_{14}^{4h} symmetry (same as tin dioxide), with two formula units per cell. The two Titanium atoms are in D'_{2h} symmetry sites, while the four O atoms are in C'_{2v} sites (Wyckoff 2a and 4f sites, respectively). The sites occupation is identical to SnO_2 and thus the irreducible representations of the vibrational modes are the same: 1 A_{1g} + 1 A_{2g} + 2 A_{2u} + 1 B_{1g} + 1 B_{2g} + 2 B_{1u} + 1 E_g + 4 E_u. Among the vibrational modes, five are Raman active (A_{1g}, B_{1g}, B_{2g} and one twofold degenerate E_g) and seven are IR active (A_{2u} and three twofold degenerate E_u) [2]. The corresponding vibrational energy are, for Raman, 143 cm^{-1} (B_{1g}), 447 cm^{-1} (E_g), 612 (A_{1g}) and 826 cm^{-1}(B_{1g}), while with infrared spectroscopy are at 183 (E_u), 388 (E_u), 500 (E_u) and 167 cm^{-1} (A_{2u}).
Differently from rutile, the anatase crystal structure belongs to the D_{19}^{4h} space group, with two molecules per cell. The atoms are in sites with D_{2d} (Ti) and C_{2v}^{v} symmetry (O), corresponding to 4a and 8e Wyckoff's sites respectively. With these features, the irreducible representation of the vibrational modes are A_{1g} + $2A_{1g}$ + $2B_{1g}$ + B_{1g} + $3E_g$ +$3E_u$. According to the character table already reported for the D^{14} point group (Tab 3.1), A_{2u} and E_g are acustic modes, 1 A_{1g}, 2 B_{1g} and 3 E_g are the effective Raman active modes, while 1 A_{2u} mode and 2 E_u are IR active. In the past years different studies on the

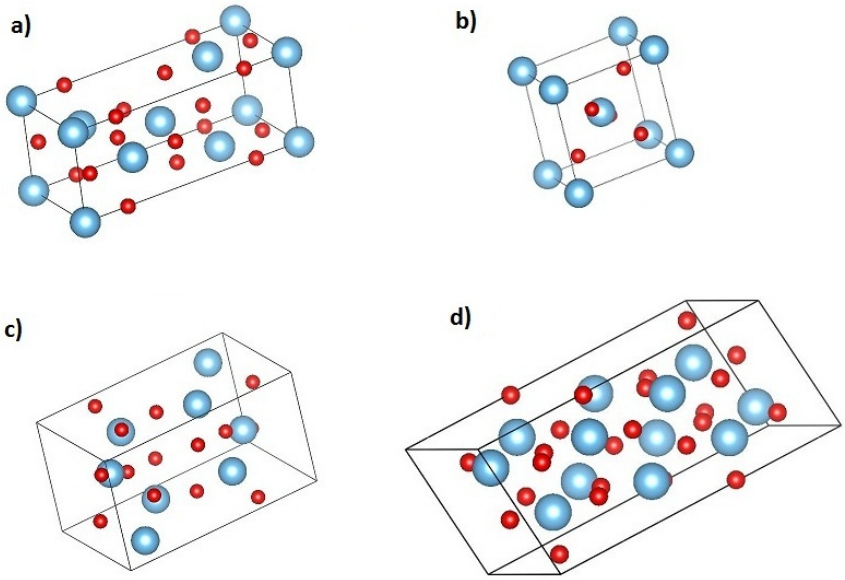

Figure 4.1: The four natural polymorphs of TiO_2: a) anatase, b) rutile, c) brookite and d) TiO_2-B. Titanium atoms are colored in light blue while oxygens are in red. Figures obtained with the program VESTA [1]

Raman vibrational frequencies of anatase crystal have been published with contradictory results on the peaks attribution. The existing ambiguities were definitely overcame by Giarola et al. [3], which through a careful polarized Raman analysis assigned the peaks at 143, 198 and 639 cm^{-1} to the three E_g modes, the one at 518 cm^{-1} to the A_{1g} mode and the two at 395 and 512 cm^{-1} to the two B_{1g} modes. As regards the infrared peaks, in trasmission mode the anatase monocrystals exhibits the A_{2u} mode at 367 cm^{-1} and the two E_u modes at 262 and 435 cm^{-1}.
The vibrational spectrum of Brookite is far more complicated: this phase has a lattice structure with a D_{2h}^{15} symmetry and eight molecules per unit cell, thus meaning a total of 72 vibrational modes. Both Ti and O atoms are in sites with C_1 symmetry (Wychoff site 8c) and, according to the group theory, the irreducible representation at the Γ point of the Brillouen zone are 9 A_g + 9 B_{1g} + 9 B_{2g} + 9 B_{3g} +9 A_{1u} + 9B_{1u} + 9 B_{2u} + 9 B_{3u}. Looking at the character table for the D_{2h} point group (see Table 4.1), 9 A_g + 9 B_{1g} + 9 B_{2g} + 9 B_{3g} are Raman active, while, after the subtraction of the acustic modes (one B_{1u}, one B_{2u} and one B_{3u}), the infrared active modes are 8 B_{1u} + 8 B_{2u} + 8 B_{3u} [4]. All the A_g Raman modes have been identified (Iliev et al.) at 125, 152, 194, 246, 324, 412, 492, 545 and 640 cm^{-1}) through a polarization analysis and the comparison

with the values obtained with DFT calculation, while not all the B mode were clearly detected. In fact, only seven of the nine B_{1g} modes were seen (at 169, 212, 283, 327, 381, 449 and 622 cm^{-1}), and also the B_{2g} modes were not completely identified (only seven, at 160, 254, 325, 366, 391, 460 and 584 cm^{-1}). Also some B_{3g} modes are still missing, as only five have been recognized until now (at 132, 212, 318, 416, 500 cm^{-1}) [5]. The symmetry attribution of the observed infrared peaks was not so straight forward: a greater discrepance was found between the calculated wavenumber values and the experimental ones. However, all the eight B_{1u} modes, six of the B_{2u} modes and seven of the B_{3u} modes have been assigned, all in the range from 168 to 587 cm^{-1}.

Table 4.1: Character table for the D_{2h} point group, from [6]

D_{2h}	E	C_2^z	C_2^y	C_2^x	i		
A_g	1	1	1	1	1		
A_u	1	1	1	1	−1		
B_{1g}	1	1	−1	−1	1		
B_{1u}	1	1	−1	−1	−1		
B_{2g}	1	−1	1	−1	1		
B_{2u}	1	−1	1	−1	−1		
B_{3g}	1	−1	−1	1	1		
B_{3u}	1	−1	−1	1	−1		
D_{2h}	o^{xy}	o^{xz}	o^{yz}				
A_g	1	1	1		$\alpha_{xx}, \alpha_{yy}, \alpha_{zz}$		
A_u	−1	−1	−1				
B_{1g}	1	−1	−1	R_z	α_{xy}		
B_{1u}	−1	1	1	T_z			
B_{2g}	−1	1	−1	R_y	α_{xz}		
B_{2u}	1	−1	1	T_y			
B_{3g}	−1	−1	1	R_x	α_{yz}		
B_{3u}	1	1	−1	T_x			

TiO_2-B has been widely studied in the last years, mainly because of the discovery of the promising behaviour of this polymorph as lithium-ion battery negative electrode [7]. The primitive cell of TiO_2-B is less symmetric compared to the cells of the three TiO_2 phases already presented, and belong to the monoclinic system, with a C_{2h}^3 symmetry and four formula units. Due to this a total of 36 vibrational modes are present. All the atoms are in sites with C_s symmetry (Wickoff 4i sites), and the calculated irreducible representations are 12 A_g + 6 A_u + 6 B_g + 12 B_u. Among these the 12 A_g + 6 B_g modes are Raman active, and 5 A_u + 10 B_u are infrared active (the acustic modes are one A_u and 2 B_u, see Table 4.2). The Raman modes are expected at 123 (B_g),

145 (A_g), 161 (A_g), 172 (A_g), 196 cm^{-1} (B_g) [7, 8] and at 237 (B_g), 251 (B_g), 292(A_g), 365 (A_g), 408 (A_g), 430 (A_g), 465 (A_g), 550 (A_g), 633 (B_g), 651 (A_g), 856 cm^{-1} (A_g) [9]

Table 4.2: Character table for the C_{2h} point group, from [6]

C_{2h}	E	C_2^z	i	o_h		
A_g	1	1	1	1	R_z	α_{xx},α_{yy},α_{zz},α_{xy}
A_u	1	1	−1	−1	T_z	
B_g	1	−1	1	−1	R_x,R_y	α_{xz},α_{yz}
B_u	1	−1	−1	1	T_x,T_y	

4.2 Materials synthesis

Sulfated titania (S-TiO_2) was obtained through a 1-step sol-gel procedure, a process never used before for the synthesis of nanopowder used as Nafion filler. In this procedure a solution of titanium isopropoxide in 2-propanol (Sigma-Aldrich) is used as Ti source and an aqueous sulfuric acid solution (0.5M) is adopted for both hydrolysis and sulfating processes. After 2 h of vigorous stirring, the final solution is filtered and calcined for 3 h at 400 °C [28]. Plain and composite Nafion membranes were prepared according to a solvent-casting procedure [7]. A commercial Nafion dispersion (5 wt% in water/alcohol, E.W. 1100, Ion Power, GmbH) was treated with N,N-dimethylacetamide at 80 °C to replace the solvents. For composite membranes, the inorganic powder was added to the final Nafion solution and stirred to homogenize the dispersion. 2%, 5% and 7% of filler concentrations with respect to Nafion content were chosen. Each mixture was casted on a Petri dish and dried at 100 °C to obtain self-standing membranes. Dry membranes were then hot-pressed at 175 °C at 50 atm for 15 minute and were finally activated by immersion in boiling hydrogen peroxide (3%), sulfuric acid (0.5 M) and water. Table 4.3 summarizes the samples investigated in the present work. All of the membrane samples were stored in distilled water after preparation.

4.3 Experimental methods

4.3.1 Raman spectroscopy

Micro-Raman spectroscopy measurements were carried out in backscattering geometry using the two different Horiba-Jobin Yvon spectrometers already.

Table 4.3: List of the analysed samples

Sample	Name
Sulfated TiO_2	S-TiO2
Nafion recast	M0
Nafion + 2% sulfated TiO_2	M2
Nafion + 5% sulfated TiO_2	M5
Nafion + 7% sulfated TiO_2	M2

In particular, the LABRAM equipment was used for the measurements extended to high wavenumber region while the T64000 instrument (with 647.1 nm or 514.5 nm laser excitation lines) was employed to probe the spectral region below 200 cm^{-1} down to few wavenumbers far from the laser excitation line. Independently of the spectrometer used to carry out the Raman measurements, the spectra were obtained by focusing the laser beam onto a spot of about 2 μm in size through the lens of a long-working distance 50X objective. The laser power at the samples surface was kept below 5 mW. Contrary to the SnO_2 sample, no optical filter was needed during the measurement. The spectra were calibrated in wavenumber using the emission lines of an Ar spectral lamp. As for SnO_2 and Nafion + SnO_2 samples, all the recorded spectra were processed to remove artifacts due to cosmic rays and the luminescence background.
Spectra at controlled ambient relative humidities (RH) were collected at room temperature and at 60 °C with the LABRAM HR instrument. At room temperature, the sample storage and the measurement procedure were the same already described in chapter 3. To store the samples at 60 °C at variable relative humidity condition, the sample and the desired saturated salt solution were kept in close boxes, sealed with Teflon tape, into a water bath at 60 °C. In this way an homogeneous temperature distribution was reached inside the boxes. Due to the different temperature, other salt solutions were used and different RH points were analysed with respect to the room temperature measurements (see Table 4.4 for the summary of the RH values and salts employed). Conditioning time of at least 24 h were necessary to reach stable condition. Moreover, a modification in the measuring chamber was necessary. In fact, in the configuration adopted for the room temperature spectra, a problem rose due to water condensation on the upper part of the cell (in particular on the quartz glass), indicating a non homogeneous temperature distribution inside the chamber. To avoid this problem and assure the same temperature in the whole chamber an additional pillar of copper was added at the centre of the cell to connect the bottom part of the chamber (directly in

Table 4.4: Summary of saturated salt solutions used for the samples conditioning at different RH at 60 °C. Relative humidity values were collected from [10, 11]

Saturated salt solution	RH (%)
LiCl	11
$MgCl_2$	30
$Mg(NO_3)_2$	40
KI	63
NaCl	75
K_2SO_4	96

contact with a Peltier heater) to the sample and the quartz glass above. With this modification, no more condensation was observed. All the modifications are visible in Figure 4.2.

Figure 4.2: Home-made sample holder for Raman measurements at controlled relative humidity condition and 60 °C. The sample spectra was collected trough a thin quartz glass that isolates the sample from the outer atmosphere. A column of copper provided a correct heat distribution, ensuring that the sample temperature was the same as the bottom part of the chamber, directly heated by a Peltier cell.

The same calibration procedure as described for Nafion + SnO_2 samples was used: the absolute position of the 731 cm^{-1} peak of Nafion was measured with the 1800 lines/mm grating and the Ar lamp, then the effective Raman spectra were collected with the 600 lines/mm grating and the peak were fitted with Lorentzian curves to obtain their precise position in relation to the 731 cm^{-1} peak, used as an internal reference. Also for this set of samples controls were done to be sure that no changes in the samples inner humidity were caused by the laser beam during the Raman measurement.

4.3.2 Water uptake

The procedure used for the measurement of the membranes water uptake at room temperature was the same as described in chapter 3 for the Nafion

+ SnO_2 samples. As regards the weighing at 60 °C, the samples conditioning was the same used for the Raman measurements, using the saturated salt solutions enlisted in Table 4.4 and a water bath to ensure a uniform temperature distribution. Samples were taken out from the conditioning box in closed vials and rapidly measured. The conditioning time was at least 24 h, as to carry out Raman measurements. The dry sample weight at 60 °C was measured after a storage time of at least 4 hours in vacuum.

4.3.3 FT-IR spectroscopy

FT-IR spectra were obtained at room temperature using a JASCO spectrometer mod. FT/IR-660 plus, as described in chapter 2. ATR configuration or transmission technique were used, respectively in the spectral range between 4000 cm^{-1} and 900 cm^{-1} and between 4000 cm^{-1} and 500 cm^{-1}. A Ge crystal is mandatory for the ATR measurements due to the high refractive index of the TiO_2 powder, while KBr pellets were used to record the powders spectra in transmission mode. All the IR spectra were recorded with a resolution of 4 cm^{-1}. Membranes spectra at 33 % RH, 11 % RH and in vacuum were recorded in transmission mode with 64 acquisitions, putting the salt listed in Chapter 3 (table 3.4) in the sample chamber to reach the proper humidity conditions. At least 24 hours were necessary to reach stable conditions, while the humidity value was monitored with an hygrometer. Samples were not moved from their positions between the spectra in order to probe always the same sample region. Reference spectra were recorded without the samples at the same RH conditions to eliminate the water vapour contribution, and proper baselines were subtracted from the spectra before the data analysis.

4.4 Results: S-TiO_2 powder

4.4.1 Raman spectra

The Raman spectrum of the S-TiO_2 powder carried out at the low wavenumber region is shown in Figure 4.3a. From the spectral features it appears that the sample consists of a predominant anatase phase plus a minor TiO_2-B component. All the anatase vibrational modes are present in the spectrum (the peak at about 512 cm^{-1} is hidden by the more intense one peaked at 518 cm^{-1}), although slightly shifted in wavenumbers with respect to the value enlisted in the previous section, probably for the nanocrystalline character of the powder. In addition to the anatase peaks, two TiO_2-B modes are unequivocally observed in the powder spectrum, respectively at about 250 cm^{-1} and 365 cm^{-1} (Figure 4.3a, quoted in red). As for the others peaks of this phase,

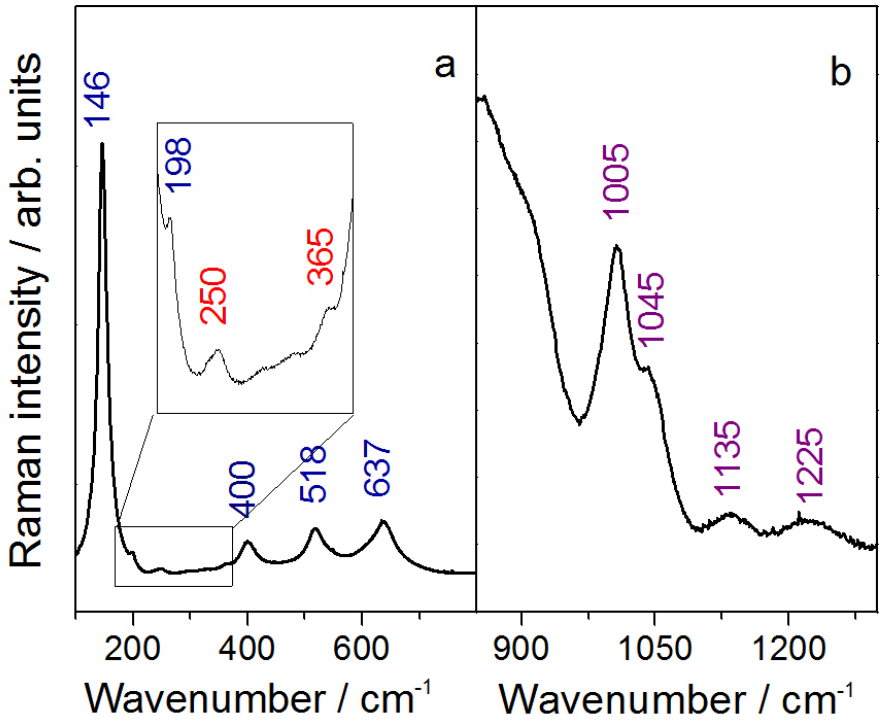

Figure 4.3: a) low wavenumbers Raman spectrum of S- TiO_2, anatase peaks in blue, TiO_2-B peaks in red b) high wavenumbers Raman spectrum of S- TiO_2, sulfate peaks in purple.

they are probably hidden under the much stonger ones due to anatase. Figure 4.3b shows the S-TiO_2 Raman spectrum recorded in the higher wavenumber region, where the spectral features related to the sulphate functionalization are expected. Here four peaks can be attributed to the sulfate vibrational modes: the peak at about 1005 cm^{-1} is assigned to the normal mode ν_1 of the SO_4^{2-} group, while the three other peaks (one at about 1045 cm^{-1} and two weaker at about 1135 and 1225 cm^{-1}) are associated to the splitting of the ν_3 vibrational mode of the SO_4^{2-} functionalization. Due to the really low intensities of the last two listed peaks, a further verification with infrared spectroscopy is needed in order to confirm the effective number of ν_3 peaks, that is directly correlated to the type of sulfate coordination.

4.4.2 Infrared spectra

The S-TiO_2 infrared spectrum was recorded by means of both transmission and ATR techniques. The KBr pellets for the transmission spectrum were made with a sufficient quantity of powder to assure the clear observation of the sulfate vibrational modes, even if in this way the titania modes were too

intense to be seen. Figure 4.4a shows the infrared spectrum obtained in transmission mode while in figure 4.4b the ATR one is presented. In both spectra it is visible the ν_1 vibrational mode at about 1000 cm^{-1} and the presence of three ν_3 modes at about 1045, 1136 and 1220 cm^{-1} is confirmed. The number and position of these modes are in agreement with the Raman results, confirming the ν_3 splitting into three different peaks. This is caused by a lowering of the SO_4^{2-} anion symmetry due to a bidentate coordination at the titania surface. The same coordination was already found in sulfate titania obtained via two different two-step synthesis routes by Sakai et al. [12, 13]

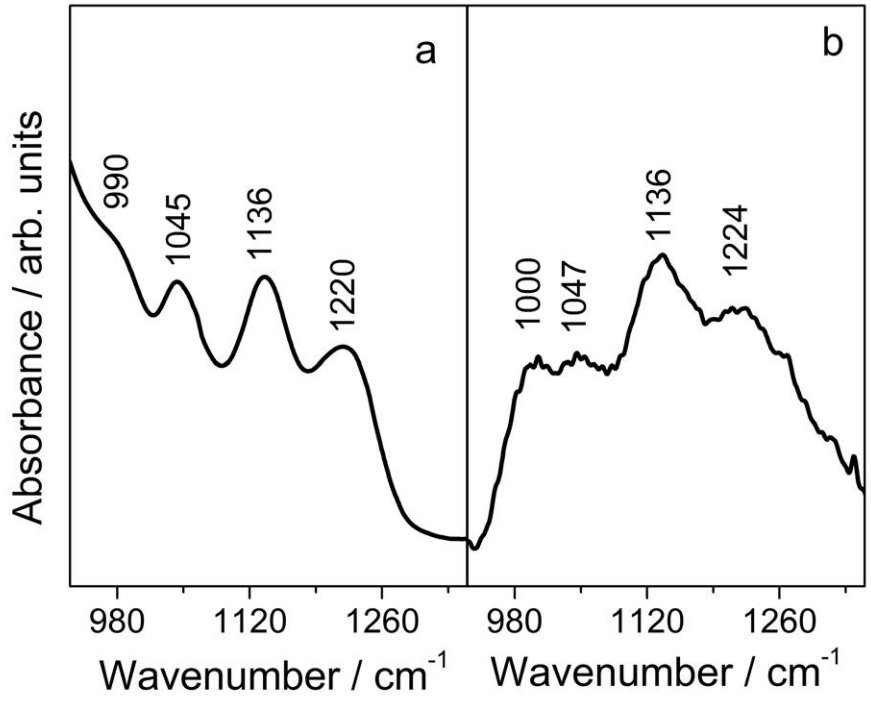

Figure 4.4: a) S-TiO $_2$ FTIR spectrum collected in transmission mode, KBr pellet$_2$ b) S-TiO_2 FTIR spectrum collected in ATR mode, Ge crystal

4.4.3 Effect of an high relative humidity environment on S-TiO_2

To investigate the nanopowder interaction with water, in order to understand the effect on S-TiO_2 caused by the inclusion in a high humidity environment like the Nafion membrane in a working fuel cell, the same powder sample measured with FTIR-ATR technique at standard ambient condition was stored in a high relative humidity (RH) environment (close to 100% RH) for at least 12 hours. ATR mode was choose for this study to avoid the use of the

hygroscopic KBr powder and eventual artifacts. The FTIR spectrum recorded after the exposure to moisture, in Figure 4.5, evidences remarkable changes of the spectral features with regard to both their number and relative intensity. In particular the disappearance of the mode at about 1224 cm^{-1} indicates a different bonding of the SO_4^{2-} groups to the titanium dioxide, with a change from a bidentate coordination to a monodentate one (Table 4.5). This modification in sulfate coordination suggests an interaction mechanism of S-TiO_2 with water molecules similar to the one proposed by Bolis et al. for sulfated ZnO_2 [14]. Similar changes on powders exposed to high relative humidity

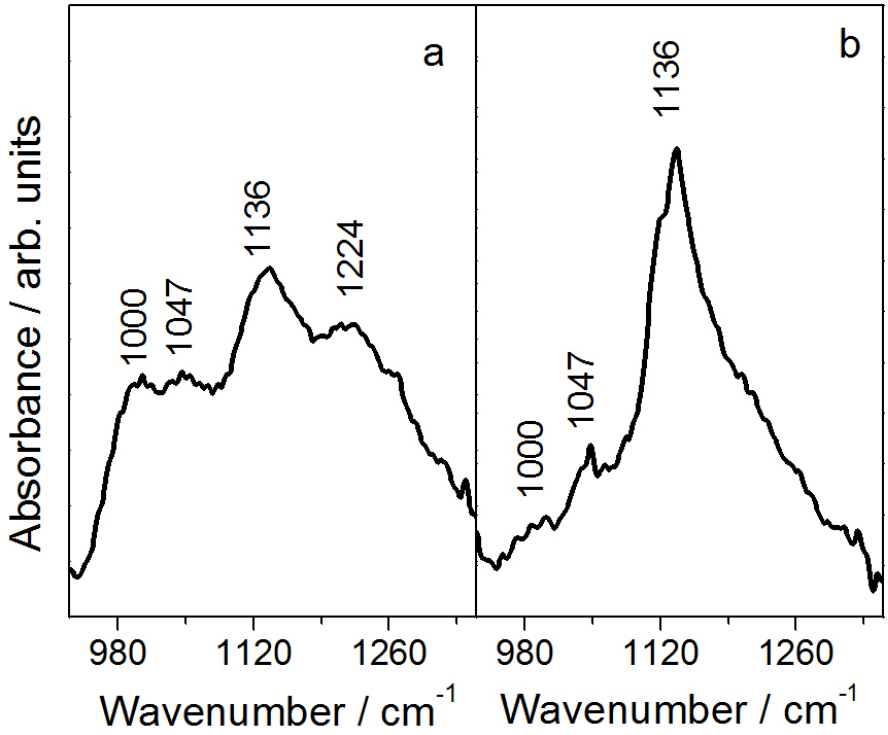

Figure 4.5: a) S-TiO_2 FTIR in ATR mode, Ge crystal, ambient humidity b) S-TiO_2 FTIR in ATR mode, Ge crystal, 100 % relative humidity

were observed by Raman spectroscopy. This technique in addition reveals the presence of an extra peak at 981 cm^{-1}, attributed to the vibration of a quasi-isolated SO_4^{2-} ion [16], not detectable for symmetry reason by IR spectroscopy. S-TiO_2 powders were also subjected to an hydrolysis treatment and thermo gravimetric analysis were carried out before and after this procedure to evaluate the loss of sulfate groups after the exposure to water, revealing that a part of the functionalization remains also afterwards, but about the 60 % of the sulfate are lost. The appearance of the isolated SO_4^{2-} peak in the Raman spectrum is in accordance with this result: the lost sulfate are the ones that show an isolated SO_4^{2-} spectrum while the sulfate ions remaining on the

Table 4.5: Sulfate ion modes splitting with different coordination, (Co(III) composites). From [15]

	Symmetry	ν_1 frequency	ν_3 frequency
free SO_4^{2-} ion	Td	not visible	1100
monodentate	C_{3v}	970	1032-1044 1117-1143
bidentate	C_{2v}	995	1050 - 1060 1170 1105

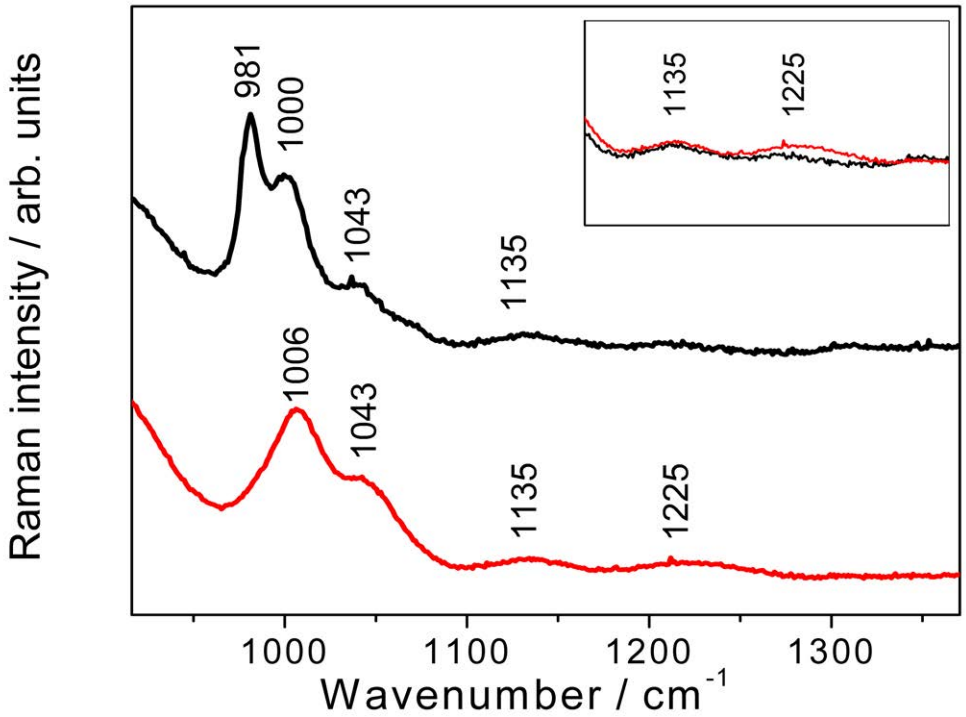

Figure 4.6: Raman spectra of S-TiO_2 powder before (red) and after (black) the exposure to a high relative humidity environment.

titania surface are the one displaying a monodentate coordination in high humidity environment.

4.5 Results: composite membranes

4.5.1 Raman spectra

As already experimented with Nafion + SnO_2 samples, the membranes reactivation treatment (immersion in boiling hydrogen peroxide, sulphuric acid and water for about 30 minutes each step) was necessary to reduce the fluorescence signal of the as received membranes to acceptable values. The Raman spectra of Nafion membranes (pure and with the three different amounts of filler) collected in the wavenumber region above 380 cm^{-1} with the LABRAM instrument are visible in Figure 4.7. A spatial inhomogeneity in the S-TiO_2 distribution over the scale of 10 μm was observed for all the nanocomposite samples and the spectra reported here should be considered as the representative for each sample.

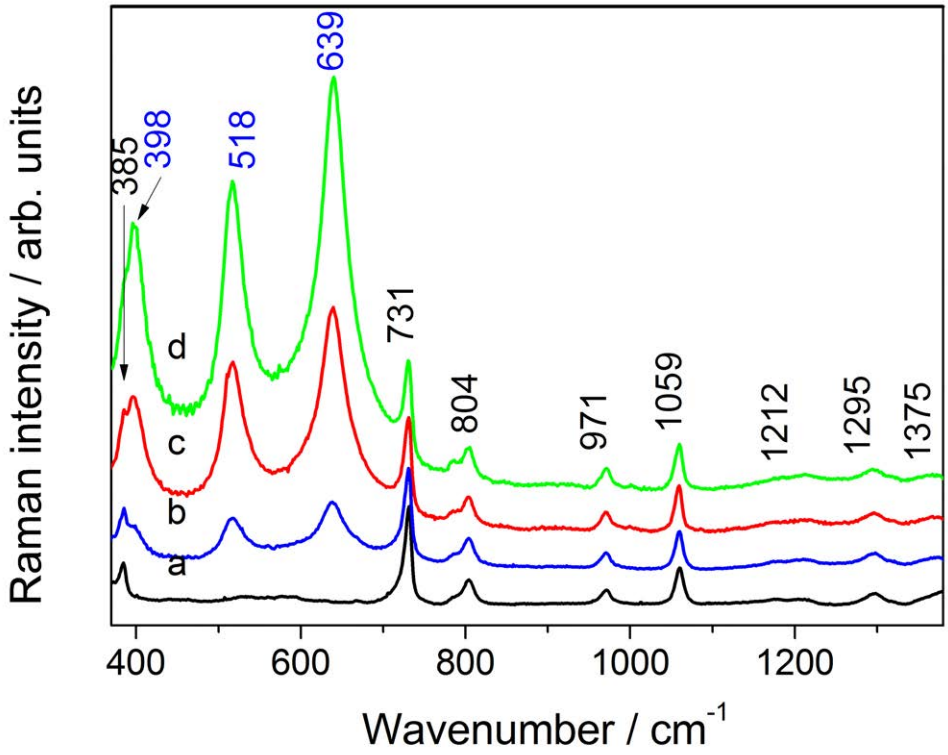

Figure 4.7: Raman spectra of M0 (black), M2 (blue), M5 (red) and M7 (green) samples, collected with the LABRAM instrument

All the spectra showed the characteristic bands of Nafion at about 385 cm^{-1}, 570 cm^{-1}, 731 cm^{-1}, 804 cm^{-1}, 971 cm^{-1}, 1059 cm^{-1}, 1212 cm^{-1}, 1295 cm^{-1} and 1375 cm^{-1} (see Table 3.2 and ref. [17] for the peaks attribution). No significant change of the Nafion peaks position was observed in com-

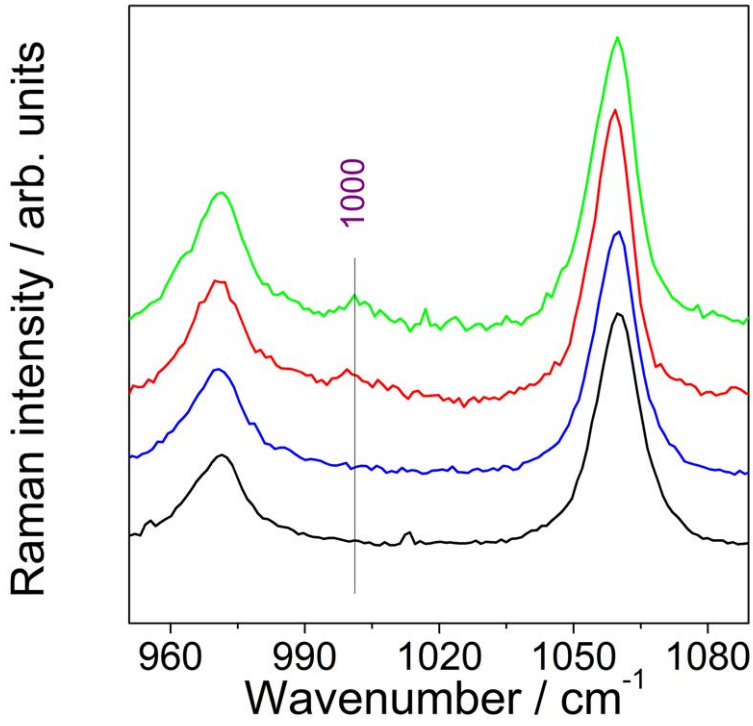

Figure 4.8: Particular of Figure 4.7 in the range 950 - 1090 cm^{-1}.

posite membranes with respect to pure one. Likewise, the peaks of TiO_2 anatase component within the composite membranes spectra occur at the same wavenumbers as in the S-TiO_2 powder. Moreover, a weak peak at about 1000 cm^{-1} is clearly detected in the composite membranes heavily loaded by S-TiO_2 (i.e. with 5% and 7% w/w, see Figure 4.8), confirming the persistence of sulphate groups also after the powder incorporation. Looking at the spectra collected in the low wavenumber region with the T64000 instrument (in Figure 4.9) is possible to observe the occurrence of an important phase rearrangement of the TiO_2 component incorporated into the Nafion membrane. In fact, comparing the vibrational features of the composite membranes with the bare powder ones in Figure 4.3 a relevant decrease of the TiO_2-B phase can be inferred.

4.5.1.1 Filler distribution

Optical microscopy images revealed a non-homogeneous surface in the composite membranes. This inhomogeneity, on the micrometric scale, was not observed in pure Nafion and neither in the previously studied SnO_2-added membranes.

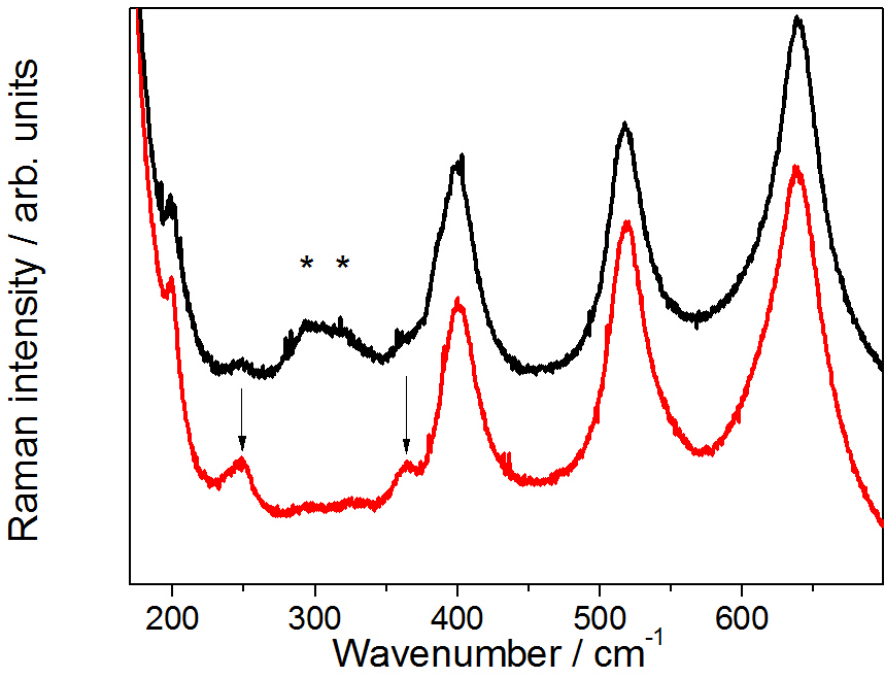

Figure 4.9: Raman spectra of M7 sample and S-TiO_2 powder in the low wavenumbers region. The stars indicate the Nafion's peaks, the arrows indicate the TiO_2-B peaks.

Raman micro-spectroscopy was used to study the possible correlation between the non-homogeneous morphology and the filler distribution: in fact the possibility to collect vibrational spectra from different micro-region of the membranes surface can be exploited to test the S-TiO_2 distribution. The results confirmed that the filler amount inside the Nafion membranes was not uniform, independently on the nominally incorporated titania amount, causing morphologically unlike regions inside the polymer matrix. To perform this study, Raman spectra were carried out from points with different morphology, moving step-by-step along straight line on the surface of the three composite samples. The optical microscopy images of the three samples surfaces are respectively in the top panel of Figure 4.10, Figure 4.11 and Figure 4.12. The Raman spectra, displayed in the three middle panels, were collected from the regions serially numbered in the top panels. To quantify the filler amount in each of the measured point a fitting procedure with Lorentzian curves was performed in order to estimate the weight of each spectral component. In particular, the intensity (I) ratios between the membrane peak at about 731 cm^{-1} and two of the S-TiO_2 peaks (at about 639 cm^{-1} and 518 cm^{-1}) were determined. The motivation for the use of two S-TiO_2 peaks, and not only one, was to obtain two independent checks of the fitting validity. This

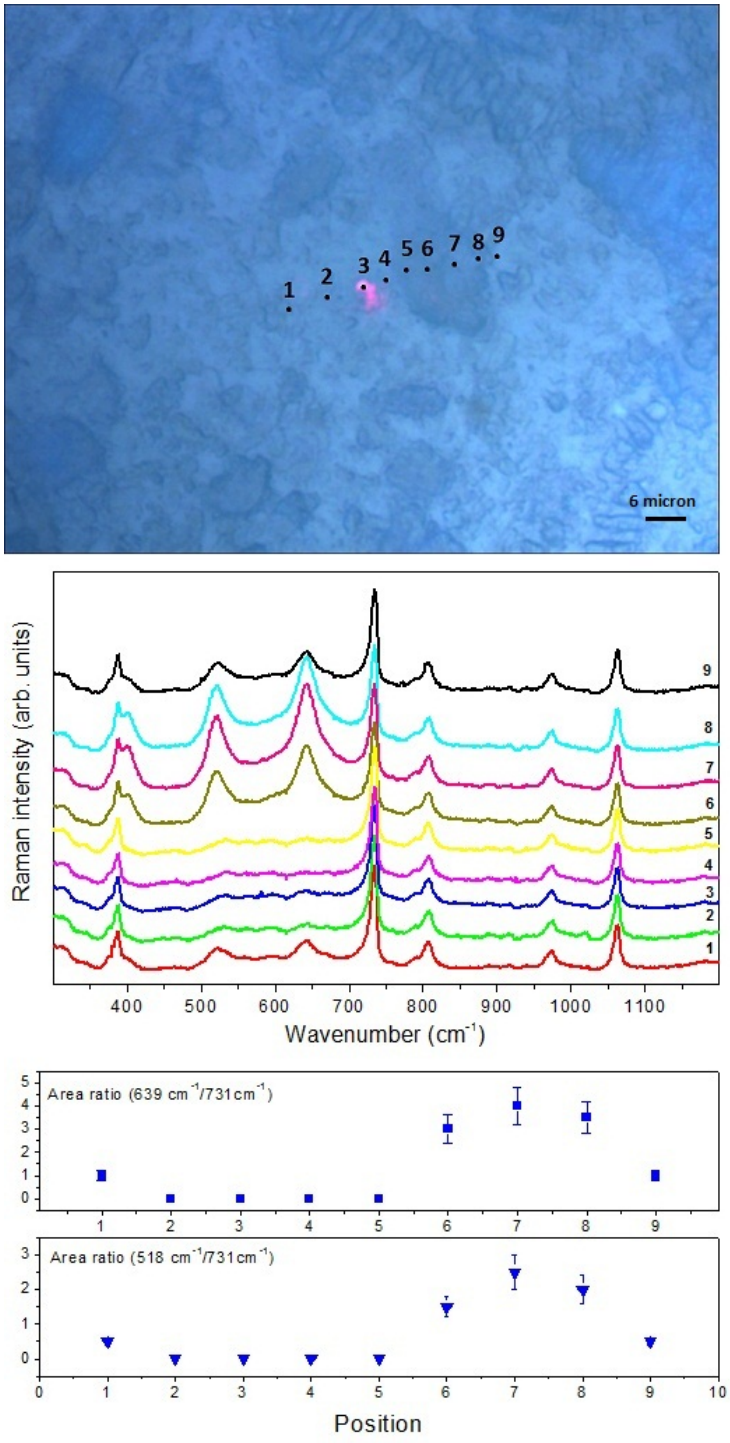

Figure 4.10: Measured points on the M2 sample surface as seen with optical microscopy (upper panel),the correspondent Raman spectra (middle panel) and the peaks area ratio (lower panel).

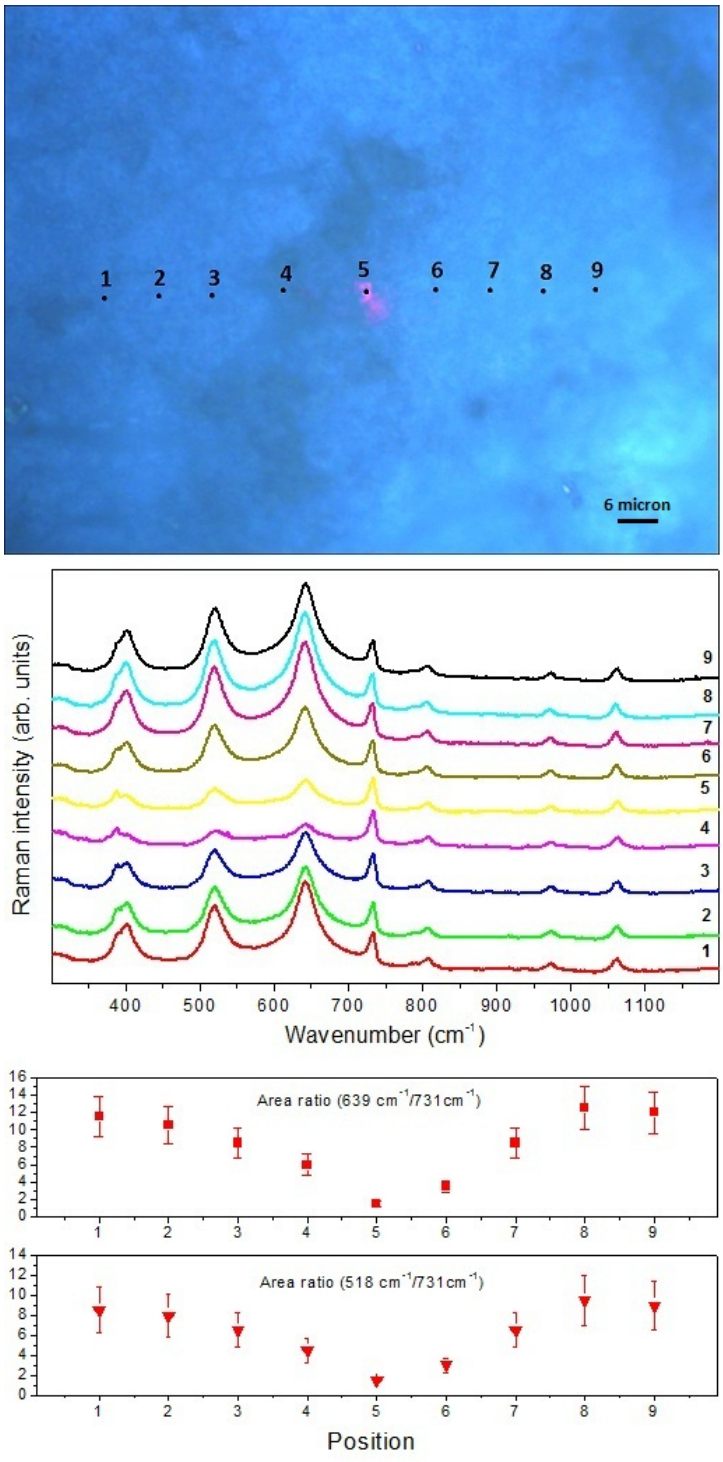

Figure 4.11: Measured points on the M5 sample surface as seen with optical microscopy (upper panel),the correspondent Raman spectra (middle panel) and the peaks area ratio (lower panel).

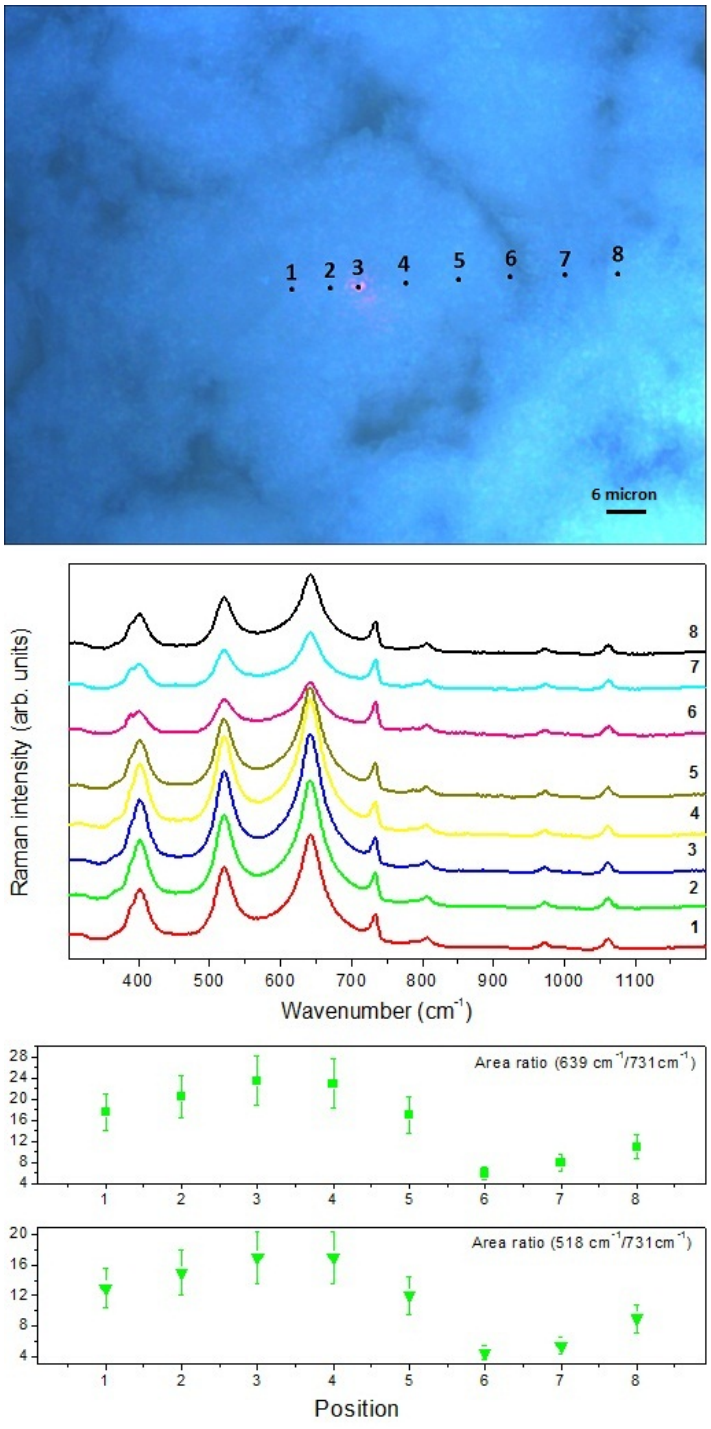

Figure 4.12: Measured points on the M7 sample surface as seen with optical microscopy (upper panel),the correspondent Raman spectra (middle panel) and the peaks area ratio (lower panel).

double check is important considering the difficulties in the subtraction of a proper baseline from the spectra, due to the presence of a high fluorescence background not clearly determinable. A relative error of about 10% on the intensities ratio was estimated to take in account also the error in the peaks intensities deriving from a not perfect baseline subtraction. Even considering these errors, the results of this study (displayed in Figure 4.10, Figure 4.11 and Figure 4.12) revealed an undoubted correspondence between the morphology characteristics of the composite membranes and their S-TiO_2 content, with the confirmation of the analysis validity by the observation of the same behaviour in both the intensity ratios I(639)/I(731) and I(518)/I(731).
In particular, the two samples with higher filler content (5% and 7%) showed brighter circular zones that turned out to be richer in S-TiO_2, while the surrounding areas have a lower filler amount. In contrast, the membrane loaded with 2% of filler have filler dense regions that look darker, probably for a different image contrast. A very interesting outcome of this study is the observation that in the case of the M2 sample a part of the membrane is almost filler free, while for higher S-TiO_2 percentage the filler is present over all the membrane surface, even if not homogeneously distributed. The existence of 'island' of filler separated by pure Nafion zones is an obstacle to the creation of proton percolation paths, that relies on a continuous filler presence in the whole membrane, and can have a negative affect on the membrane protons conduction, especially if the proton percolation is the main conduction mechanism.

4.5.1.2 Raman spectra at different ambient relative humidity

Raman spectra at different relative humidity conditions were collected for a better understanding of the effect of the filler inclusion on the membrane at a microscopic level, with particular attention at the membranes inner environment at different ambient conditions. The RH values explored at room temperature were the same used for the N-110 and N-F110S samples, enlisted in Table 4.4. In addition, in order to analyse the membrane inner environment at a temperature closer to the real fuel cell working condition, a study at 60 °C was performed, at the RH value listed in Table 4.4. For both temperatures, at least three different sample points were measured for each RH value. 100 % relative humidity condition was not explored at 60 °C because even the really short time requested to move the sample from the conditioning box to the measuring chamber caused water condensation on the sample surface, with a change in the measuring condition (Nafion water content in saturated vapour condition and with immersion in water are not the same, [18]). To be sure that all the spectral changes observed for a sample were imputable

only to the change in humidity conditions, and not to a different local filler content (due to the membranes non-homogeneous S-TiO_2 distribution), the TiO_2 peaks intensity, relative to the Nafion peaks intensity, was monitored to assure a similar filler value for each sample point.
To obtain an accurate estimation of the peaks position, all the peaks presented in the spectra were fitted with Lorentzian curves and the calibration procedure already described in the experimental section was applied. In contrast to the analysis procedure carried out for Nafion + SnO_2 samples, a prior subtraction of the powder contribution from the composite membrane spectra did not turn out as an improvement for the subsequent fitting. In this case in fact a problematic baseline subtraction, joined to the changes observed in the powder phase after the inclusion in membrane and the high intensities of the titania peaks, caused errors in the powder spectrum subtraction too big to assure a reliable procedure, being reflected in a great divergence in the fitted parameters (in particular of the peak intensities) following small changes in the adopted baseline or estimated titania contribution. Anyhow, with or without the powder subtraction, the errors on the fitted intensities were greater that the actual changes observed caused by the different humidity condition. Due to this, the analysis was limited to the peaks positions, that were almost independent on the baseline or initial fitting parameters chosen.
As expected (since already observed for the SnO_2-added Nafion), the main difference recorded by changing RH conditions was the energy position of the peak attributed to the SO_3^- vibration (whose trend for the four analysed samples is visible in Figure 4.13). Again, the shift for pure Nafion was in good agreement with the behavior reported in literature [19]. On the contrary, the behavior of the nanocomposite membranes, in particular M5 and M7 samples, was very different from that of pure Nafion, and a deviation in the peak position was observed at both low and high relative humidities. As already explained in chapter 3, the SO_3^- peak energy directly depends on the S-O dipole electrostatic interaction with the H^+ counterions, and thus a deviation in the peak energy at equal RH means a difference in the SO_3^- perturbation.
It is shown in Figure 4.13 that in a low humidity environment the samples with 5% and 7% of filler have a lower vibration energy compared to pure Nafion. Two possible situations can explain this behaviour: a higher quantity of water near the sulfonic groups compared to the pure Nafion values, that result in a greater shielding from the H^+ ions, or an interaction with the filler resulting in a lower net charge perceived by the SO_3^- groups (for example, H^+ ions can interact with the filler and less perturb the sulfonic group vibration). Raman spectroscopy does not provide clear evidences to support one theory or the other but, as explained in the next section, infrared spec-

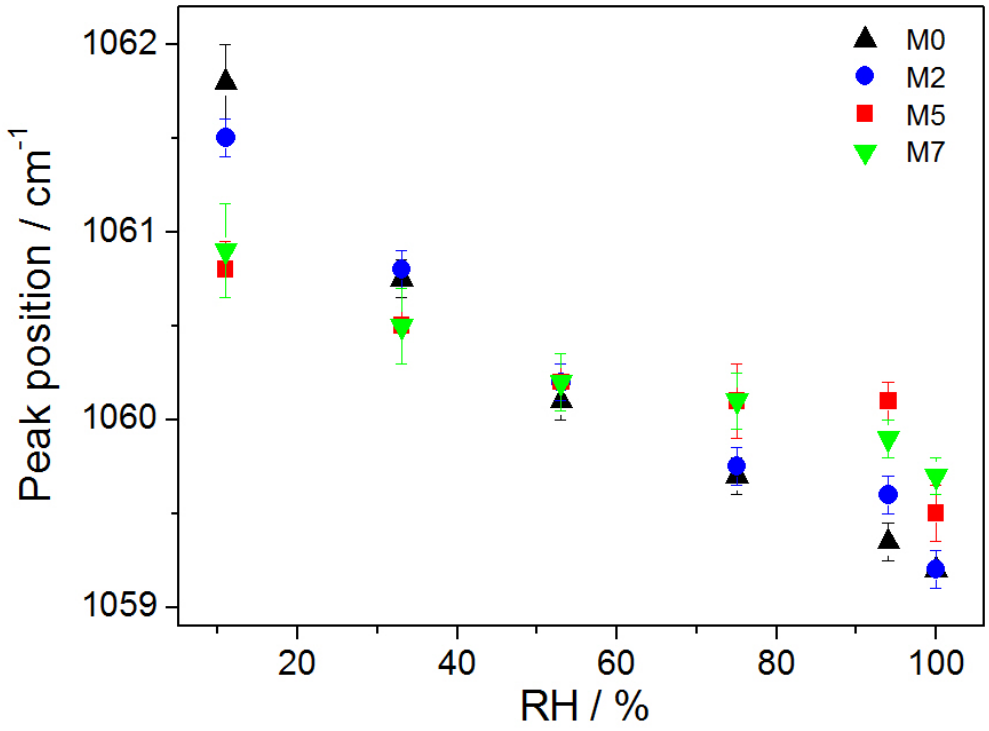

Figure 4.13: SO_3^- peak positions vs ambient relative humidity at 25 degree for pure Nafion (black), M2 (blue), M5 (red) and M7 (green).

troscopy can shed light on the situation.
At high relative humidities, on the other hand, composite samples show a higher vibrational energy compared to pure Nafion, with a behaviour similar to the one already observed for Nafion + SnO_2 samples. In this case, however, the vibrational energy for M5 and M7 samples did not completely return to values equal to pure Nafion at 100 % RH.
This trend can be explained in terms of an interaction effect between filler and membrane that increases the net charge experienced by the sulfonate ions (note that this interaction has to be opposite in effect to the one postulated for the low RH range) or with a lower water content (local or total) in the composite membranes. Analysis performed with DSC on the temperature and entalpy of the endothermic transition centered for pure Nafion at 145 °C, attributed to an order-disorder transition of ionic cluster caused by the loss of water, confirmed the presence of a lower amount of water in contact with the sulfonate ions with increasing filler quantity at high RH.

Interesting results were obtained from the measurements carried out at 60 °C. At low RH the vibrational energy of sulfonate ions in pure Nafion greatly increased with respect to room temperature values, as observed in literature [19], while M2, M5 and M7 energies are much closer to the room

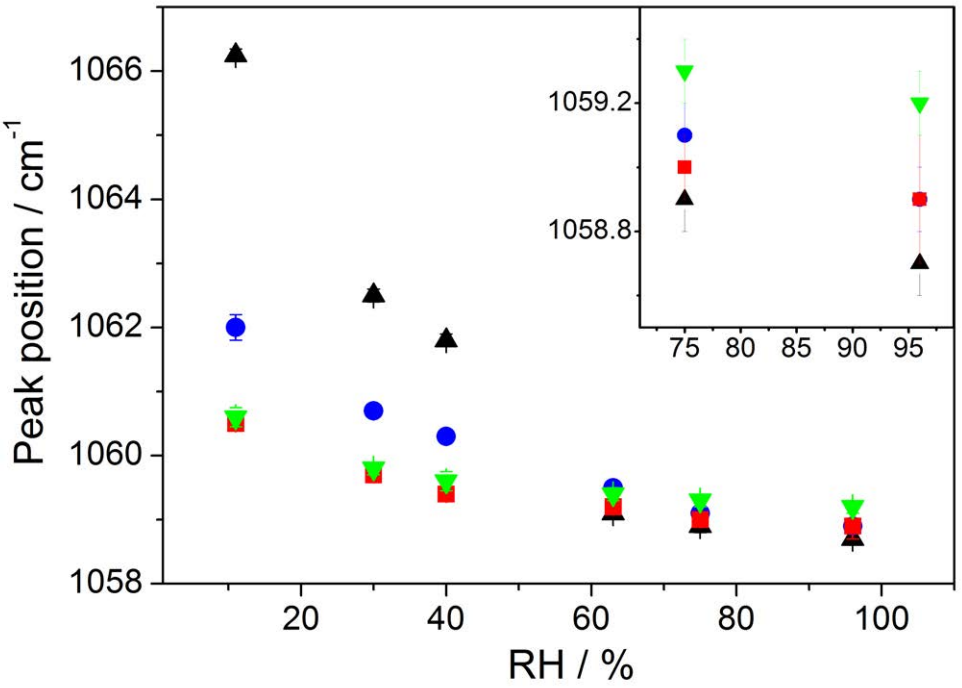

Figure 4.14: SO_3^- peak positions vs ambient relative humidity at 60 degree for pure Nafion (black), M2 (blue), M5 (red) and M7 (green).

temperature values. Due to this the energy differences of the SO_3^- ions peak observed between the composite membranes and pure Nafion at 60 °C are much greater, going from a 1 cm^{-1} difference at room temperature to more than 5 cm^{-1} at 60 °C in a 11 % RH environment. On the other hand, at high RH the energy differences with respect to pure Nafion were almost null for samples M2 and M5, while they remained almost the at the same value as at room temperature for M7 sample. Furthermore, no appreciable difference was detected at low humidity between the 5 % and the 7% samples at both room temperature and 60 °C. This is in accordance with the hypothesis, based on results obtained from DTGA and AFM analysis, that at the highest filler inclusion a part of the powder is included into the Nafion hydrophobic zones, thus not interacting with the polymer side chains.

4.5.2 Water uptake

The samples water uptake trend showed a BET type isotherm, typical of a multilayered water adsorption mechanism, with tightly bound water in the initial stage of hydration followed by loosely bound water in the latter stage, as already reported for pure Nafion in literature [20, 21, 22]. Even if all the

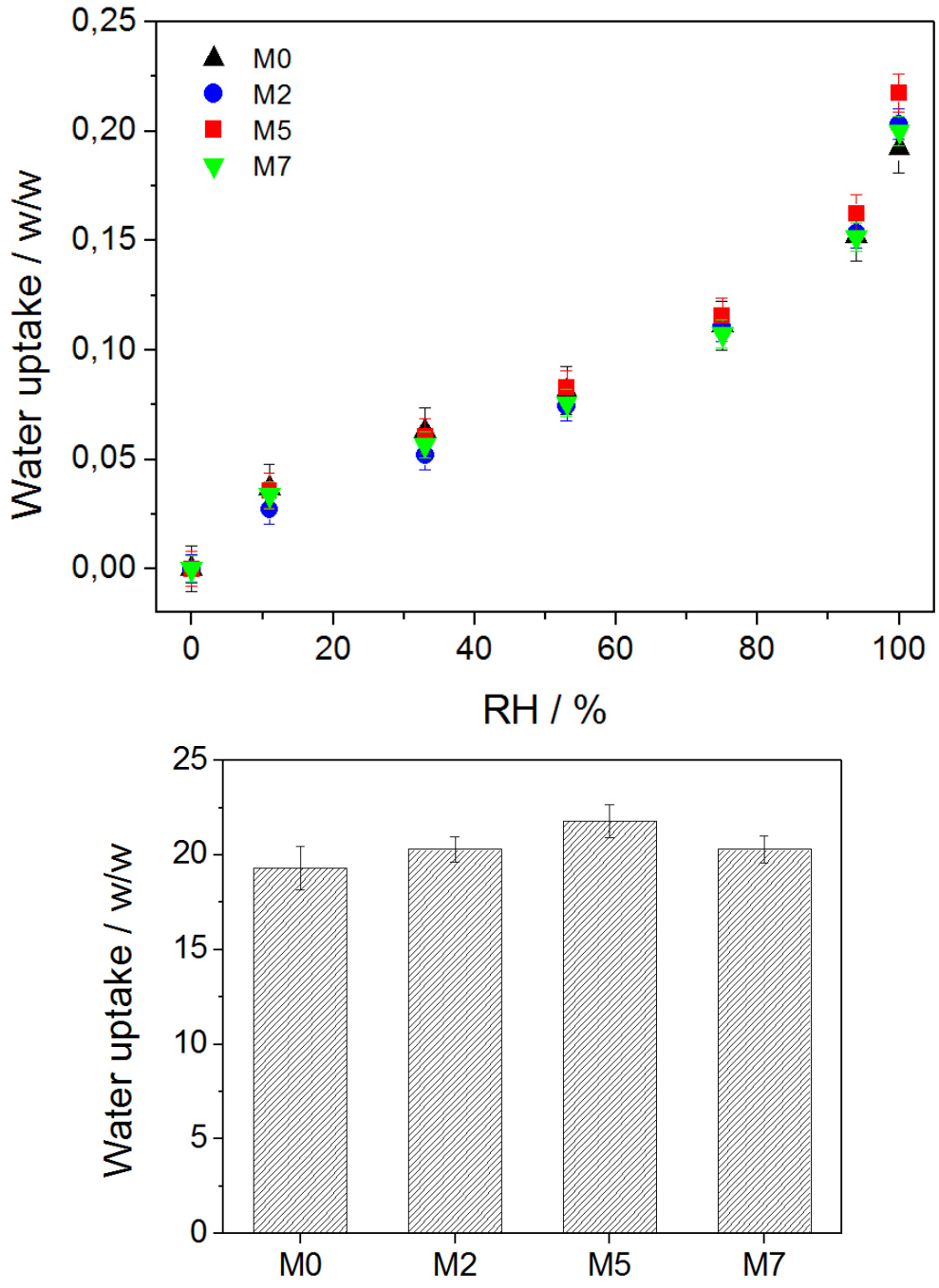

Figure 4.15: Water uptake vs ambient relative humidity at 25 °C for pure Nafion (black), M2 (blue), M5 (red) and M7 (green).

membranes present a similar behaviour, some difference can still be noted. At room temperature M0 and M2 had indistinguishable trend, thus suggesting that a concentration of 2 % w/w of filler is not enough to highlight any diver-

gence in water uptake capacity. 5 %-added sample is the one that achieved the highest hydration at high RH values, showing the effect of the hygroscopic properties of the filler. To better appreciate the differences at 100 % relative humidity a separate panel has been added to the Figure 4.15. Surprisingly, a further addition of filler, like in the M7 sample, caused a decrease in the membrane hydration capability. Again, like in Nafion + SnO_2 samples, no evidence was found in the water uptake behaviour of the different trend observed with Raman spectroscopy at high RH in the composite membranes with respect to pure Nafion. This mean that the lower water content at high RH suggested by Raman and DSC measurements is not a characteristic of the whole membrane, but it is located only in the proximity of the sulfonate ions. Due to this, it is possible to conclude that at high humidity the filler is in competition with the membrane for the hydration, as already observed for Nafion + SnO_2 samples.
As for the low RH region, no substantial divergences were observed between the samples, thus the hypothesis that the differences in vibrational energy observed with Raman were due to an overall higher water content is ruled out. However, the hypothesis of an interaction effect or a local higher water content are still valid.

A different situation occurs at 60 °C: all the uptake values measured were lower than at 25 °C in line with literature [23], but this time is the M2 sample that showed the higher water uptakeat high RH, while M5 and M7 values were similar to the M0 sample. According to this is possible to say that the dissimilarity observed at high RH between M5 and M7 samples are not caused by different overall water contents. However, other analysis are needed in order to explain the Raman and water uptake data, like measurements at an intermediate temperature (i.e. 40 °C) to confirm the observed trends.

4.5.3 Infrared spectra

The FT-IR ATR spectra of pure and composite Nafion is characterized by five main peaks (Figure 4.17), all related to Nafion membrane, at about 965, 983, 1060, 1153 and 1212 cm^{-1}, respectively, in accordance with the literature values [17]. A small, but systematic spectral difference was observed for all the loaded samples at about 1220 cm^{-1}. The spectra were collected after drying each sample in vacuum for 30 minutes to be sure that the observed spectral variation were not due to a different hydration between the samples. Having excluded this, the origin of the observed variation might be related either to a rearrangement of the Nafion structure due to the powder incorporation (causing a change in the membrane vibrational properties), or to the S-TiO_2

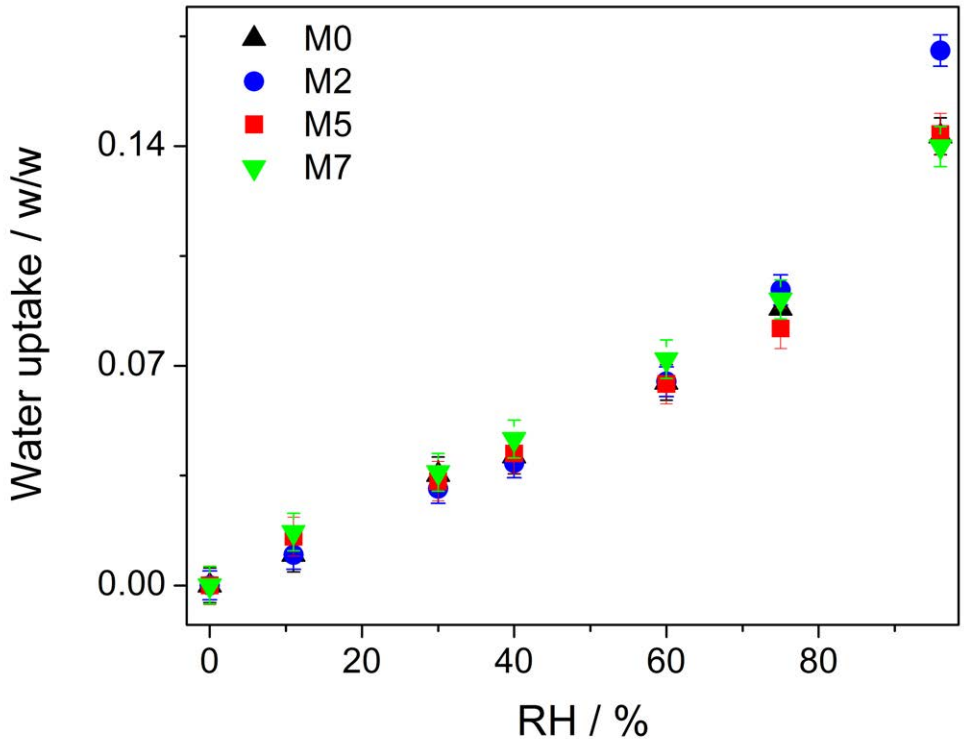

Figure 4.16: Water uptake vs ambient relative humidity at 60 °C for pure Nafion (black), M2 (blue), M5 (red) and M7 (green).

sulfate peak at around 1224 cm^{-1}. In the latter case, however, at least an additional peak near 1136 cm^{-1} would be also expected in the composite membrane, due to the highest of the sulfate peaks observed in S-TiO_2 powder spectrum (see Figure 4.5). This is not the case, and the spectral change is likewise due to a modification in the Nafion local structure, suggesting an interaction between the filler and the host polymeric network.

As described out in the previous sections, difference in the SO_3^- vibrational energies at low relative humidity were observed with Raman spectroscopy for the composite membrane, but no clear evidences were found that could explain the reasons. FT-IR spectroscopy has proven to be an helpful technique to resolve this problem, since it give the possibility to directly study the water bands associated with the bending of the water molecules inside the membranes. Notwithstanding the great disagreement on bands deconvolution and attribution found in literature in the pure Nafion case, usually three main bands are reported in the water bending region (between 1500 and 2000 cm^{-1}): one at about 1630 cm^{-1}, due to almost free water molecules, and two at higher wavenumbers, due to water associated with protons [24, 25, 26], that together form an asymmetric bands usually peaked

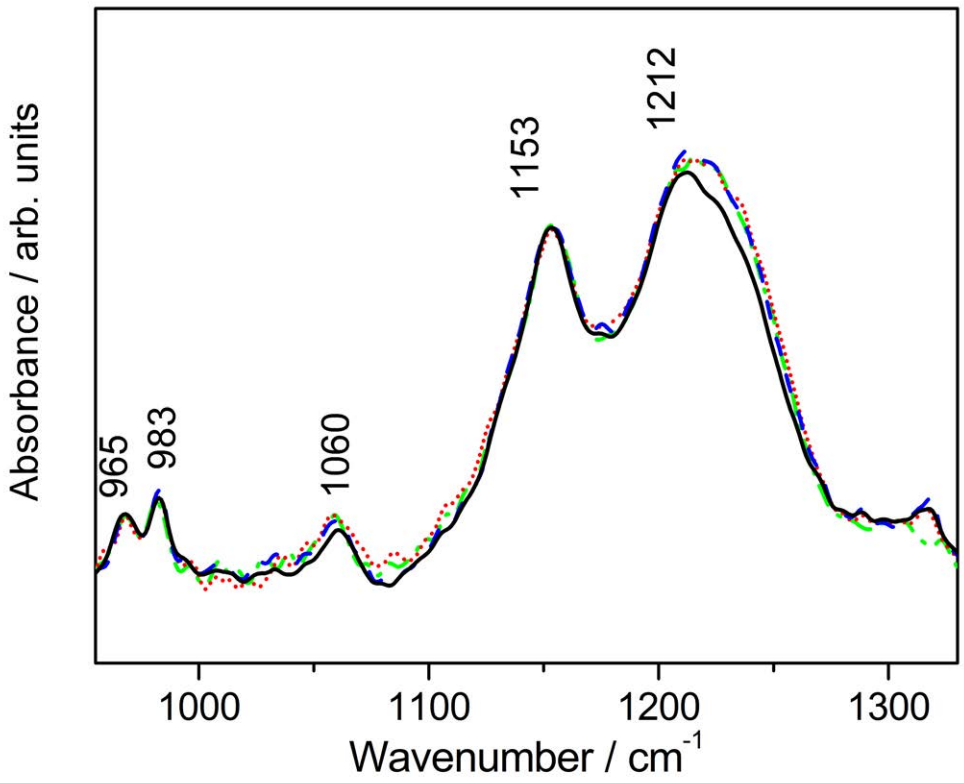

Figure 4.17: FT-IR ATR spectra of M0 (black), M2(blue), M5 (red) and M7 (green) samples.

at about 1740 cm^{-1}. Kunimatsu et al. [24] recorded (with ATR technique) the Nafion IR spectra during hydration and dehydration cycles, showing that, after the subtraction of the membrane spectrum in dry condition, the asymmetric band at 1740 cm^{-1} can be deconvoluted in two sub-bands centred at about 1730 and 1840 cm^{-1}, with peaks positions dependent on the membrane hydration. Moreover, the researchers found a linear relationship between the total area of the composite band at 1740 cm^{-1} and the SO_3^- vibrational energy, at least at low relative humidities. The explanation of this finding was that the dissociation of the SO_3^- - H^+ groups, while causing the shift of the SO_3^- vibrational frequency, also cause an increase of the number of hydrated protons, and thus the increase of the 1740 cm^{-1} band area.
A similar analysis was performed also during this thesis work. First of all, the spectrum of the pure filler, detected with diffuse reflectance technique, was recorded at different environmental humidities, with particular attention to the water bending region. In this way it was possible to study the vibrational bands due solely to the water molecules interacting with the filler. The resulting spectra, at 11 7% RH and 33% RH, are visible in figure 4.18. As can

be seen, two different Gaussian bands can fit the spectra: one at around 1640 cm^{-1}m and the second at around 1700 cm^{-1}. No other water bands appear in this region, and thus no bands caused by the filler presence are expected in the composite membrane far from 1640 and 1700 cm^{-1}. This means that, reasonably, the interesting zone corresponding to the 1740 cm^{-1} Nafion composite peak is not overlapped by filler contributions in the composite membrane.

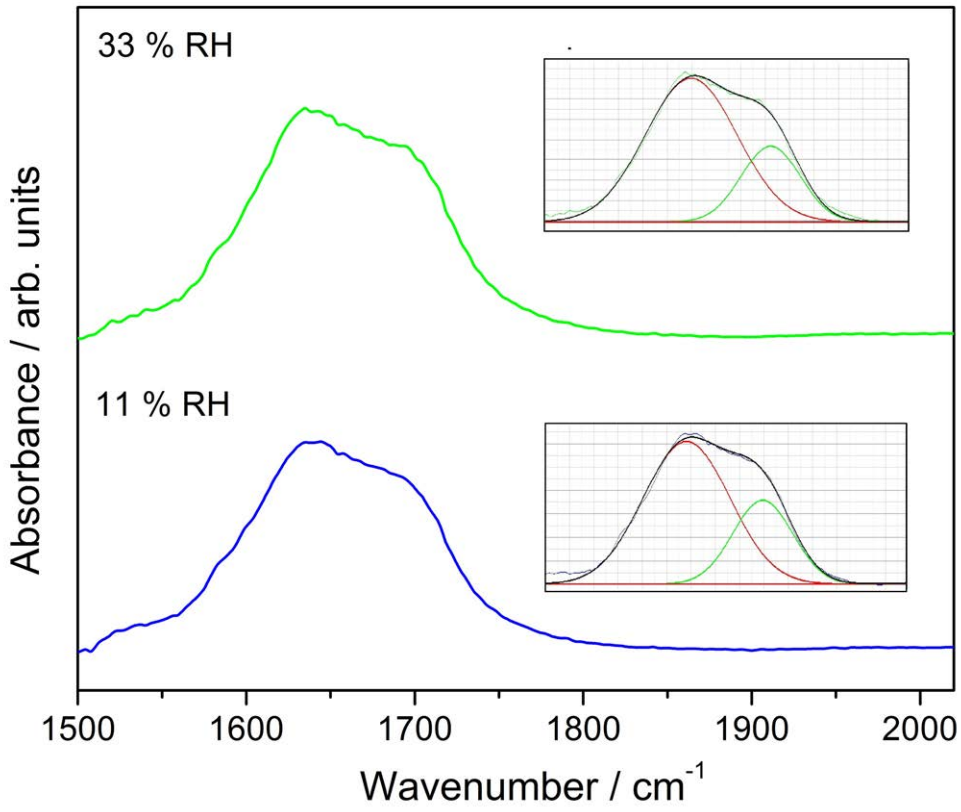

Figure 4.18: FT-IR spectra collected with diffuse reflectance technique of S-TiO_2 powder at 11 % and 33 % relative humidity. Inset: fitting with Gaussian curves.

As regards the membranes spectra, unfortunately it was possible to measure only two of the four samples: the pure Nafion (M0) and the heaviest loaded sample (M7). In fact the membranes spectra collected with ATR technique resulted in a absorbance signal too low to allow a proper data analysis of the water bands, and only these two sample, slightly thinner that the others, could be measured in transmission mode avoiding the detector saturation. However, the higher absorbance value due to the selected measurement technique did not allow the simultaneusly study of the SO_3^- vibrational peak, to compare infrared and Raman results. The infrared spectra were collected at

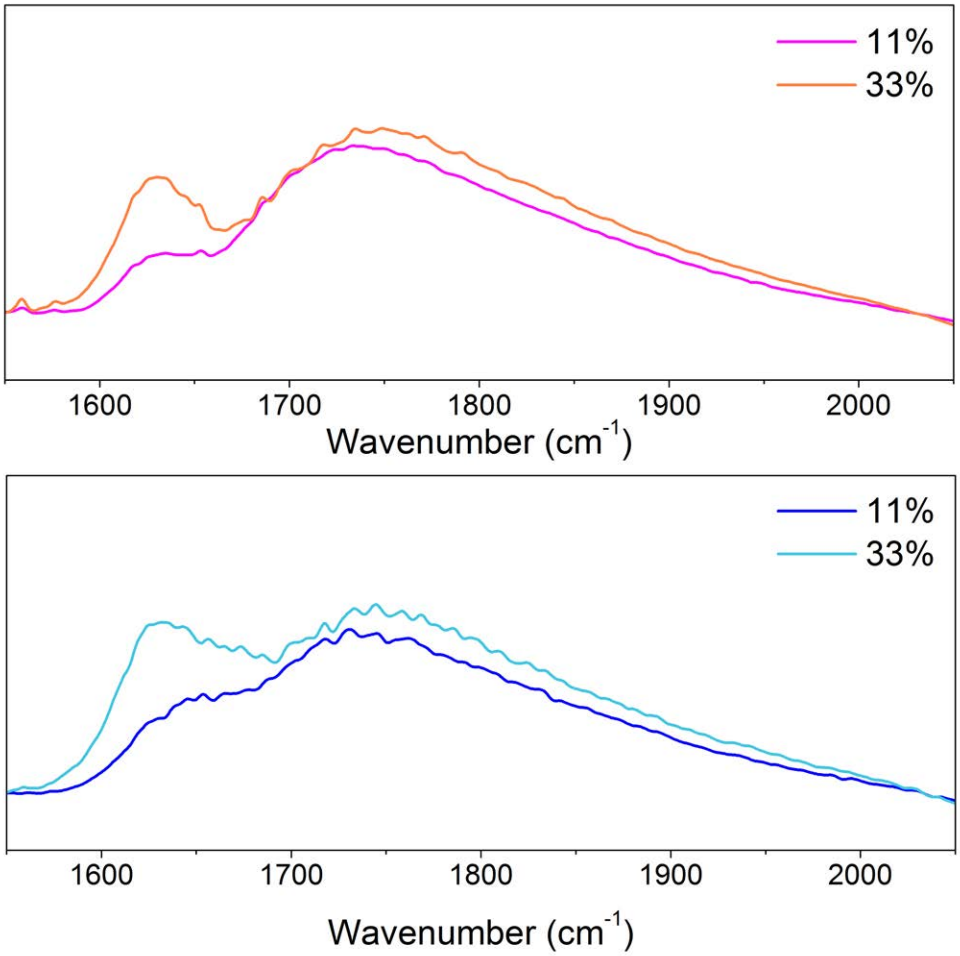

Figure 4.19: FT-IR spectra collected in transmission mode of M0 sample at 11 % (pink) and 33 % (red) relative humidities, and M7 at 11 % (blue) and 33 % (light blue) relative humidity, after the vacuum spectrum subtraction.

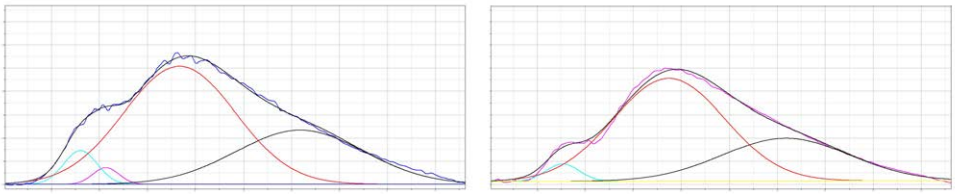

Figure 4.20: Gaussian fitting of M0 (right) and M7 (left) spectra at 11% RH.

33 % RH, 11 % RH and under vacuum (used as reference). The water vapour peaks, usually present in the water bending range, have been subtracted by taking reference spectra at the same relative humidity conditions without the

Table 4.6: Gaussian fItting results

M0 11 % RH	
1740 cm^{-1} total area	49,5
1630 cm^{-1} area	1,7
M0 33 % RH	
1740 cm^{-1} total area	58
1630 cm^{-1} area	7,5
area variation 1740 cm^{-1}	17 %
M7 11 % RH	
1740 cm^{-1} total area	59
1630 cm^{-1} area	3,3
1660 cm^{-1} area	1,3
M7 33 % RH	
1740 cm^{-1} total area	69
1630 cm^{-1} area	11
1660 cm^{-1} area	3,8
area variation at 1740 cm^{-1}	17 %

samples. The results, after the subtraction of the vacuum background, are visible in Figure 4.19, in the wavenumber range 1500-2020 cm^{-1}. A fitting procedure was then performed in order to separate the different bands contributions and analyse the changes in the bands area. Three different Gaussian water bands were supposed to exist in the pure Nafion case, with starting positions (before the optimization procedure) at 1630, 1730 and 1840 cm^{-1}. The full width half maximum (fwhm) of the bands obtained in the pure Nafion case at 33% RH were keep fixed for all the other fittings. In the M7 case, an additional Gaussian band has to be added caused by the filler presence, and from the fitting procedure its centre resulted at about 1660 cm^{-1}, with a significant shift from the pure filler case. The second band due to the water-filler interaction, found at 1640 cm^{-1} in the pure filler, was considered included in the main band at 1630 cm^{-1} and not added. The comparison of the experimental results and the fitted curves at 11% RH are depicted in Figure 4.20.
In Table 4.6 the fitting final values are shown. Particularly interesting are the results of the total area of the composite band at 1740 cm^{-1}: changing the environmental humidity from 11 % to 33 %, the same trend is observed for M0 and M7 samples, with an area variation around 17 %. Instead, with Raman spectroscopy, a variation in the SO_3^- vibrational energy of about 1 cm^{-1} was recorded for the pure Nafion, while for the M7 sample the measured varia-

tion was the half. If the observed changes were caused by a different trend in SO_3^- hydration between the two sample, meaning a different number of dissociated proton, also the 1740 cm^{-1} total area variation was expected to be the half for the M7 sample. This is not the case, and is possible to conclude that the SO_3^- different vibrational energies are probably due to a filler - Nafion interaction, that causes a lower perturbing net-charge. The presence of an interaction between filler and polymer is usually beneficial for the membrane conduction because additional hopping paths involving both Nafion and filler acidic sites are created, fundamental for the proton conduction especially at critical conditions, i. e. low RH and high temperatures. This beneficial effect was confirmed by the M5 and M0 resistivity values in situ: at low humidity environment (30 % RH) M5 sample showed a better proton conduction, with a bigger difference from the M0 values for higher temperature.

4.6 Conclusion

Raman spectroscopy measurements carried out on S-TiO_2 samples revealed the presence of two titania polymorphs: a prevalent anatase phase and a TiO_2-B phase. The sulfate functionalization was confirmed by the results of both Raman and infrared measurements, and a sulfate bidentate coordination was revealed. After the exposure to a high relative humidity environment, however, a change in the powder vibrational spectrum was detected, caused by a partial detachment of the sulfate ions from the oxide surface and the modification of the coordination of the remaining sulfate from bidentate to monodentate.
The filler inclusion in the composite membranes was confirmed, even if an inhomogeneous filler distribution was found. This inhomogeneity was common to all the different filler percentage explored (2, 5 and 7%), but while in M5 and M7 samples the filler was still present in all the membrane surface, for the M2 sample filler free zones were detected, that could interrupt possible protons percolation paths. Due to this a lower membrane conduction is expected for the M2 sample, if the percolation is the main membrane conduction mechanism.
Differently from the Nafion + SnO_2 samples, the sulfate groups of the filler remained also after the inclusion in membrane (or at least a part of them), as revealed by a peak at around 1000 cm^{-1} in the Raman spectrum for the highly doped membranes. Moreover, a lowering of the TiO_2-B phase amount was observed after the filler inclusion. With Infrared spectroscopy a difference in the composite membranes spectra with respect to the pure Nafion was de-

tected and attributed to a modification in the Nafion local structure, caused by a polymer - filler interaction. A detailed Raman analysis carried out at room temperature and different relative humidities with particular attention on the SO_3^- peak position revealed differences in the M5 and M7 inner environment at both high and low relative humidity with respect to pure Nafion. For the high RH range, the Raman measurements, together with DSC and water uptake, confirmed also in this case, as for Nafion + SnO_2, there is a competition between filler and membrane for the hydration. Again, the effect of the filler inclusion was not the expected one, and the higher water content in the filler proximity are counterbalanced by a lower hydration near the sulfonic groups. As for the lower humidities range, subsequent FT-IR measurements on the M0 and M7 samples revealed that the origin of the different SO_3^- vibrational energy is probably due to a filler - membrane interaction, that results in a lower net charge perceived by the sulfonate ions. The same Raman analysis was repeated also at 60 °C, to explore a temperature closer to the real fuel cell working conditions. At low relative humidities the difference between pure Nafion and composite membranes were in this case much greater, while at high RH the SO_3^- peak energy values were similar to the pure Nafion one for M2 and M5 samples and still higher for the M7 sample. Looking at the water uptake in high RH condition was possible to conclude that is not a higher overall water content the reason of the M5 diversity from the M7 sample: both M5 and M7 showed the same water uptake values, but different Raman behaviour. Further analysis are necessary, also at an intermediate temperature, for a better understanding of these differences.

Bibliography

[1] K. Momma and F. Izumi, "Vesta 3 for three-dimensional visualization of crystal, volumetric and morphology data," *J. Appl. Crystallogr.*, vol. 44, pp. 1272–1276, 2011.

[2] S. Porto, P. A. Fleury, and T. C. Damen, "Raman spectra of TiO_2, Mgf_2, Znf_2, Fef_2 and Mnf_2," *Physical review*, vol. 154, pp. 522–526, 1967.

[3] M. Giarola, A. Sanson, F. Monti, G. Mariotto, M. Bettinelli, A. Speghini, and G. Salviulo, "Vibrational dynamics of anatase TiO_2: Polarized raman spectroscopy and ab initio calculations," *Physical review B*, vol. 81, p. 174305, 2010.

[4] Z. Li, S. Cong, and Y. Xu, "Brookite vs anatase TiO_2 in the photocatalytic activity for organic degradation in water," *ACS Catal.*, vol. 4, pp. 3273–3280, 2014.

[5] M. Iliev, V. Hadjiev, and A. Litvinchuk, "Raman and infrared spectra of brookite (TiO_2): Experiment and theory," *Vibrational spectroscopy*, vol. 64, p. 148152, 2013.

[6] D. Rousseau, R. Bauman, and S. Porto, "Normal mode determination in crystals," *Journal of Raman spectroscopy*, no. 10, pp. 253–290, 1981.

[7] T. Beuvier, M. Richard-Plouet, and L. Brohan, "Accurate methods for quantifying the relative ratio of anatase and TiO_2(b) nanoparticles," *J. Phys. Chem. C*, vol. 113, pp. 13703–13706, 2009.

[8] M. B. Yahia, F. Lemoigno, T. Beuvier, J.-S. Filhol, M. Richard-Plouet, L. Brohan, and M. Doublet, "Updated references for the structural, electronic, and vibrational properties of TiO_2b bulk using first-principles density functional theory calculations," *J. Chem. Phys.*, vol. 130, p. 204501, 2009.

[9] V. Aravindan, N. Shubha, Y. L. Cheah, R. Prasanth, W. Chuiling, R. R. Prabhakara, and S. Madhavi, "Extraordinary long-term cycleability of TiO_2 - b nanorods as anodes in full-cell assembly with electrospun pvdf - hfp membranes," *J. Mater. Chem. A*, vol. 1, pp. 308–316, 2013.

[10] L. Greenspan, "Humidity fixed points of binary saturated aqueous solutions," *Journal of Research of the National Bureau of Standards-A. Physics and Chemistry*, no. 81A, pp. 89–95, 1977.

[11] A. Schneider, "Neue diagramme zur bestimmung der relativen luftfeuchtigkeit über gesättigten wässerigen salzlösungen und wässerigen

schwefelsäurelösungen bei verschiedenen temperaturen," *Zeitschrift HOLZ als Roh- und Werkstoff*, no. 18, pp. 269–272, 1960.

[12] T.Sakai, S. Kajitani, S. Kim, J. Hamagami, H. Oda, M. Matsuka, H. Matsumoto, and T. Ishihara, "Proton conduction properties of hydrous sulfated nano-titania synthesized by hydrolysis of titanyl sulfate," *Solid State Ionics*, vol. 181, p. 17461749, 2010.

[13] T.Sakai, S. Kajitani, S. Kim, J. Hamagami, H. Oda, M. Matsuka, H. Matsumoto, and T. Ishihara, "Proton conduction properties of nano-titania modified by sulfuric acid impregnation," *J Solid State Electrochem.*, vol. 16, pp. 2055–2059, 2012.

[14] V. Bolis, G. Magnavacca, G. Cerrato, and C. Morterra, "Microcalorimetric characterization of structural and chemical heterogeneity of superacid SO_4/ZrO_2 systems," *Langmuir*, vol. 13, pp. 888–894, 1997.

[15] K. Nakamoto, *Infrared and Raman Spectra of Inorganic and Coordination Compounds*. 1986.

[16] C. E. L. Myhre, D. H. Christensen, F. M. Nicolaisen, and C. J. Nielsen, "Spectroscopic study of aqueous H_2SO_4 at different temperatures and compositions: Variations in dissociation and optical properties," *J. Phys. Chem. A*, vol. 107, pp. 1979–1991, 2003.

[17] A. Gruger, A. Rgis, T. Schmatko, and P. Colomban, "Nanostructure of Nafion membranes at different states of hydration: An ir and raman study," *Vibrational Spectroscopy*, no. 26, p. 215225, 2001.

[18] T. Z. T. et al., "A comparative study of water uptake by and transport through ionomeric fuel cell membranes," *J Electrochem Soc*, no. 140, pp. 1981–1985, 1993.

[19] M. Hara, J. Inukai, K. Miyatake, H. Uchida, and M. Watanabe, "Temperature dependence of the water distribution inside a Nafion membrane in an operating polymer electrolyte fuel cell. a micro-raman study," *Electrochimica Acta*, no. 58, p. 449455, 2011.

[20] K. A. Mauritz and R. B. Moore, "State of understanding of Nafion," *Chem. Rev*, no. 104, pp. 4535–4585, 2004.

[21] R. Duplessix, M. Escoubes, B. Rodmacq, F. Volino, E. Roche, A. Eisenberg, and M. Pineri, "Water absorption in acid Nafion membranes," in *Water in Polymers* (S. P. Rowland, ed.), pp. 469–486, American Chemical Society, 1980.

[22] T. A. Z. Jr., M. Neeman, L. O. Sillerud, and S. Gottesfeld, "Determination of water diffusion coefficients in perfluorosulfonate ionomeric membranes," *J. Phys. Chem.*, no. 95, pp. 6040–6044, 1991.

[23] K. Broka and P. Ekdunge, "oxygen and hydrogen permeation properties and water uptake of Nafion 117 membrane and recast film for pem fuel cell," *J. Appl. Electrochem. A*, vol. 27, pp. 117–123, 1997.

[24] K. Kunimatsu, B. Bae, K. Miyatake, H. Uchida, and M. Watanabe, "Atr-ftir study of water in Nafion membrane combined with proton conductivity measurements during hydration/dehydration cycle," *J. Phys. Chem. B*, no. 115, pp. 4315–4321, 2011.

[25] K. Kunimatsu, K. Yagi, B. Bae, K. Miyatake, H. Uchida, and M. Watanabe, "Atr-ftir analysis of the state of water in a sulfonated block poly(arylene ether sulfone ketone) membrane and proton conductivity measurement during the hydration / dehydration cycle," *J. Phys. Chem. C*, no. 117, pp. 3762–3771, 2013.

[26] V. D. Noto, R. Gliubizzi, E. Negro, M. Vittadello, and G. Pace, "Hybrid inorganic-organic proton conducting membranes based on Nafion and 5 wt. of mxOy (m = Ti, Zr, Hf,Ta and W) part i. synthesis, properties and vibrational studies," *Electrochimica Acta*, no. 53, pp. 1618–1627, 2007.

Chapter 5

Composite SPEEK with TiO_2 and TiO_2SO_3H as filler

5.1 SPEEK vibrational properties

In order to analyse the SPEEK vibrational features, a good starting point is the study of the un-solfonated polymer PEEK. A large number of authors have studied this polymer with IR spectroscopy, and an important study of Chalmers et al. [1] assessed that the relative intensity of some bands is dependent on the sample degree of crystallinity, checked by wide angle X-ray diffraction. In particular, the absorbance ratios between the peaks at 1305 and the one at 1280 cm $^{-1}$ and between the peaks at 970 and 952 cm $^{-1}$ are strongly correlated with the sample crystallinity, with a decrease in both ratios in more amorphous samples.
The Raman analysis of PEEK was strongly limited due to persistent fluorescence. Despite of this, samples of PEEK were studied by Louden [2] with standard Raman spectroscopy, confirming that also with this technique a different crystallinity of the samples is related with spectral changes. Moreover, FT-Raman has proved to be a good alternative for the analysis of PEEK vibrational features, due to the lower energy of the incident laser that causes less sample fluorescence.
After the sulphonation process, PEEK polymer became S-PEEK, and new vibrational peaks confirm the change. In IR, new absorption bands appeared upon sulfonation at about 1080 cm^{-1}, (corresponding to the O-S-O sulphuroxygen symmetric vibration), about 1020 cm^{-1} and about 1255 cm^{-1} [3], with increasing intensities with respect to the backbone carbonyl band at 1651 cm^{-1} as the degree of sulfonation increase. Moreover, the aromatic C-C band visible in IR at 1489 cm^{-1} for PEEK is split due to new ring substitution upon sulfonation [4]. With Raman, only a new peak at about 1025 cm^{-1} is clearly

visible after the sulfonation. A list of the more intense peak visible for SPEEK polymer in IR and Raman is shown in Table 5.1.
Recently the correspondence between the 1305 and 1280 cm $^{-1}$ peak ratio and the polymer crystallinity was confirmed also for the SPEEK polymer, pure and doped with silica, extending this type of FT-IR analysis also to the sulfonated polymer [5].

Table 5.1: Assignments of the Raman and IR peaks of SPEEK (800 - 1700 cm^{-1}), from [6, 3, 7] (only the strongest peaks have been reported)

Raman (cm^{-1})	IR (cm^{-1})	Assignment
812		v C-H
1013	1013	ring mode
1026	1024	v(S=O)
	1082	S=O
1150		vs (C-O-C)
1206		v(C-O)
	1225	C-O-C
1284		ring mode
1305	1308	ring mode
1415	1415	C-O-C
	1471	v(C-C) ring
	1491	v(C-C) ring
1598	1597	vs(C=C)
1609		v(C=C)
1648	1646	v(C=O)

5.2 Material synthesis

Nanometric TiO_2 was synthesized via sol-gel reaction from titanium (IV) isopropoxide calcinated at 450 °C [8]. The synthesis of TiO_2-RSO_3H was carried out following a two-steps synthetic pathway: as first the hydroxyl groups on TiO_2 surface were silylated with MPTMS, obtaining mercaptopropyl - functionalized titania (TiO_2-RSO_3H) and then the thiol groups were oxidated into sulfonic acid groups to obtain propylsulfonic - functionalized titania (TiO_2-RSO_3H) [9]
For the SPEEK synthesis, PEEK powder (20 g, 69 meq) was dissolved in H_2SO_4 96% (1 L) and stirred at 25 °C for hours. The solution was poured in a large excess of ice-cold water under continuous stirring, obtaining a white precipitate. After standing overnight, the precipitate was filtered and washed several times with cold water to neutral pH. The obtained SPEEK polymer

was then dried at 80 °C overnight [10]. Composite membranes with 10 wt.% TiO_2 or TiO_2-RSO_3H content were prepared by a solution casting procedure, in which the SPEEK polymer (250 mg) was dissolved in Dimethilacetamide (DMAc, 20 mL) at 80 °C. The filler (TiO_2 or TiO_2-RSO_3H) was dispersed in DMAc and the resulting mixture was kept under stirring for 4 h at 80 °C, then added to the SPEEK solution. The mixture was heated to 80 °C under stirring until a volume reduction to 5 mL was observed, then cast onto a Petri plate and heated to 80 °C overnight. Pure SPEEK membranes were also prepared and used as references. As for Nafion membranes, before any characterization all the membranes were treated with an activation procedure: firstly they were immersed in a 0.5 M H_2SO_4 solution at 80 °C for 1 h to remove the remaining casting solvent and then in distilled water at 80 °C to remove the residual sulphuric acid.

5.3 Experimental methods

Micro-Raman spectra at standard ambient conditions were carried out in backscattering geometry by means of a single monocromator micro-sampling set-up (Horiba-Jobin Yvon, model LabRam HR), or a triple axis monocromator setup (Horiba-Jobin Yvon T64000), both described in chapter 2. All the spectra collected with the T64000 instrument were obtained with the 514.5 nm laser line. In contrast to the composite-Nafion cases, the re-activation treatment did not reduced the SPEEK sample fluorescence. Due to this, before the membrane measurements, a preliminary irradiation time of about two hours was necessary to partially quench the fluorescence and obtain Raman spectra with a good signal to noise ratio. The remaining luminescence background however limited the measurement range to not less than about 400 cm^{-1}.
FT-IR spectra were obtained at room temperature in ATR configuration for the membranes and in transmission mode (KBr pellet) for the powders, using a JASCO spectrometer mod. FT/IR-660 plus, described in chapter 2. For the ATR measurement, the high refractive index of the samples allowed only the use of Ge crystal. All the membranes were measured in fully hydrated condition after the immersion in liquid water. In this way, a better adhesion was reached between membranes and Ge crystal, causing a higher absorbance signal. The IR spectra were recorded with a resolution of 4 cm^{-1}, using a polystyrene film as a reference.

5.4 Results: TiO_2 and TiO_2RSO_3H powders

The analysed powders were the nominally pure nano-titania and the propylsulfonic - functionalized nano-titania. As described in chapter 1, the main reasons of this titania functionalization are the increasing of the total number of sulfonic groups in the membrane, without the usual swelling problem of highly sulfonated SPEEK, and a more uniform filler dispersion due to the presence of both hydrophobic aliphatic chains and terminal hydrophilic groups.
The vibrational properties of the main polymorphs of titanium dioxide have already been discussed in chapter 4, both for Raman and IR spectroscopy. With Raman spectroscopy, the analysis of titania and sulfonated titania nanopowders revealed that only the anatase phase was present, with no peaks attributable to other titanium dioxide isomorphs, and in particular no peak related to a TiO_2-B phase (Figure 5.4 for the low wavenumber spectrum).

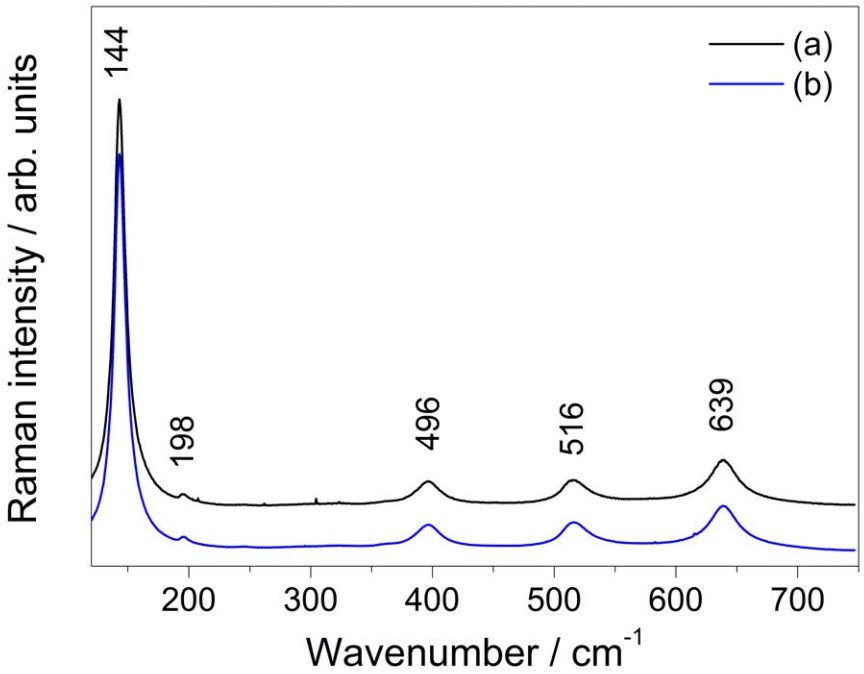

Figure 5.1: Raman spectra of the pure TiO_2 (a) and the TiO_2SOH_3 (b) nanopowders, collected with the T64000 instrument.

Moreover, with the LABRAM instrument, a peak at about 1045 cm^{-1}, due to the symmetric vibration of the sulfonic group, and two peaks at around 2890 and 2935 cm^{-1}, due to the CH_2 stretching, were detected in the functionalized powder, confirming the effectiveness of the functionalization procedure. The symmetric vibrational peak of the sulfonic acid group is visible also with

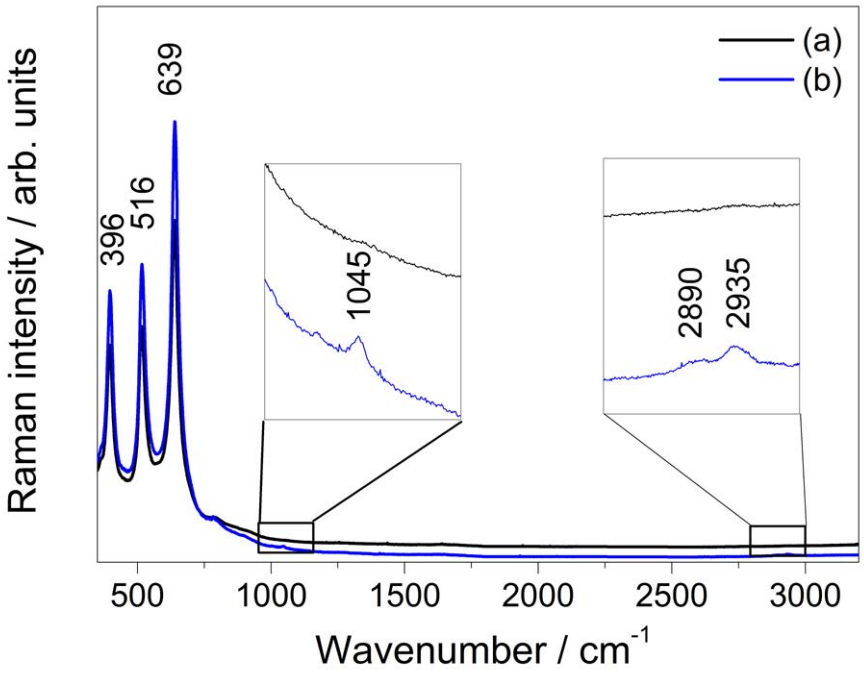

Figure 5.2: Raman spectra of pure TiO_2 (a) and TiO_2SOH_3 (b) nanopowders, collected with the LABRAM instrument.

FT-IR spectroscopy at about 1044 cm^{-1}, together with another at 1140 cm^{-1}, also caused by the sulfonic acid vibrations. The band observed at around 1600 cm^{-1} with IR spectroscopy is due to the bending movement of the water molecules inside the powder pellet, but due to the simultaneous presence in the pellet of the highly hygroscopic KBr no informations can be obtained on the nanopowder-water interaction. The same argument is valid for the broad band peaked at 3500 cm^{-1}: this is formed by the convolution of the water stretching bands (water present both in the filler and in KBr) and of the OH stretching band of the sulfonic group, resulting in a number of sub bands absolutely too high for a detailed analysis.

5.5 Results: composite membranes

The Raman spectra of the SPEEK membranes, both pure and composite, were extremely difficult to record due to the persistent fluorescence. Despite of this, all the three different samples (pure SPEEK and composite SPEEK with TiO_2 and with TiO_2RSO_3H) were finally measured, and their spectra are shown in Figure 5.4. All the spectra presented the characteristic peaks of the SPEEK polymer: the peaks observed at about 557, 812, 1013, 1150, 1206, 1284, 1305,

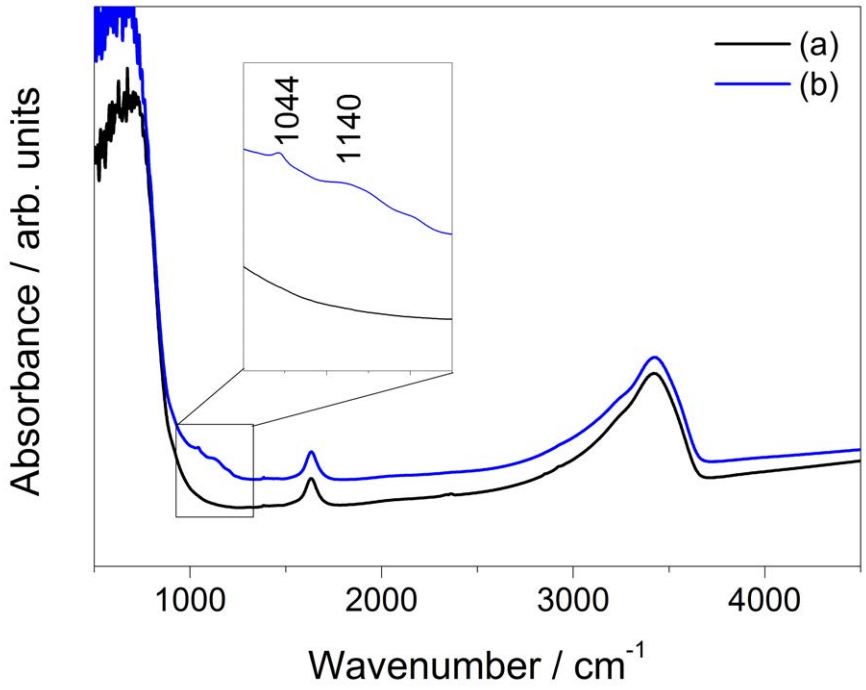

Figure 5.3: Infrared spectra of TiO_2 (a) and TiO_2SOH_3 (b) nanopowders .

1415, 1598, 1609 and 1648 cm^{-1} are due to the PEEK backbone vibrations and the one occurring at at 1026 cm^{-1} is due to the SPEEK sulfonic group vibration. In both the composite membranes, two anatase peaks are detected, at 518 and 639 cm^{-1}, confirming the powder inclusion, but no peaks due to the sulfonic groups were visible in the sample with TiO_2RSO_3H. This result is not surprising: comparing the anatase and the functionalization peaks intensities in the pure powder spectrum (Figure 5.4) a great difference was observed, and the intensity of the anatase peaks in the composite membranes spectra lead to the conclusion that the sulfonic peaks are too low to be seen. Also the CH_2 vibrational peaks at around 2900 cm^{-1} were not seen (spectral region not shown) for the same reason. Apparently a difference in the titania peaks intensity, relatively to the SPEEK ones, is observed between the two composite membranes, but repeated measurements in different samples zones confirmed that this is only due to a disomogeneity in the filler distribution, and not to an higher filler content in the SPEEK + pure TiO_2 sample. Unfortunately, the long exposure time of the sample to the laser needed to partially quench the fluorescence turned out to change the measurement parameters, thus preventing measurements under defined conditions, like the Raman study at different relative humidity. The FT-IR spectra of the membranes were obtained with ATR techniques, because the samples thickness

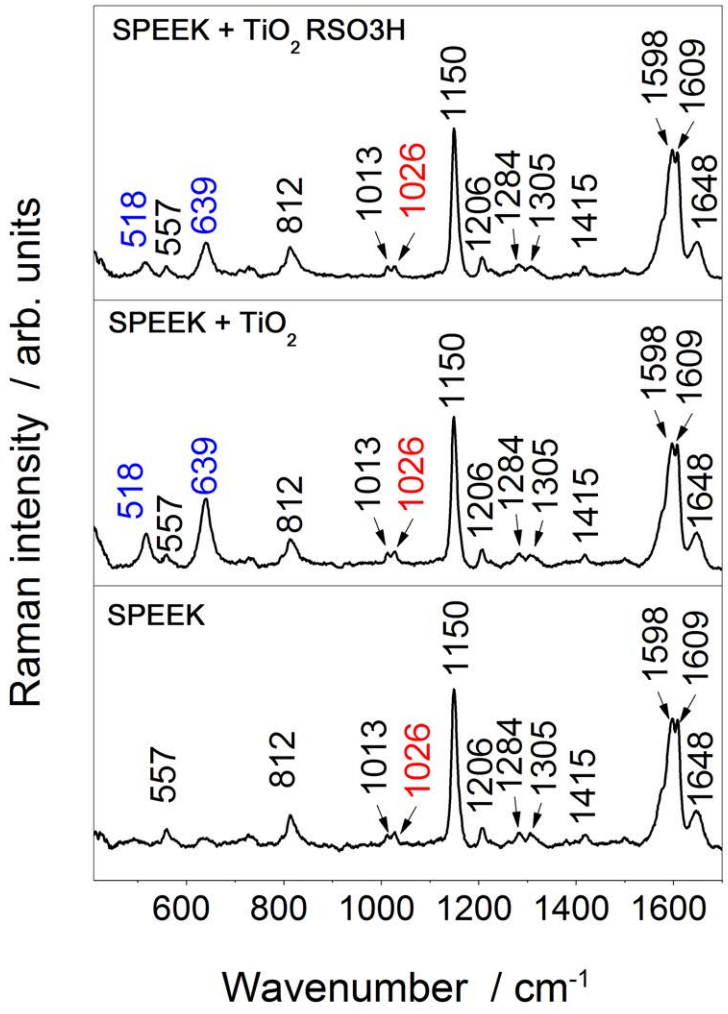

Figure 5.4: Raman spectra of pure SPEEK (lower panel), SPEEK + TiO_2 (middle panel) and SPEEK + TiO_2SOH_3 (upper panel), collected with LABRAM instrument. In blue the titania peaks.

were too high for transmission measurements. All the expected SPEEK peak were detected, the ones due to the PEEK backbone (at 1013, 1225, 1308, 1415, 1597, 1646 cm^{-1}) and the ones that are caused by the polymer sulfonation (at 1024, 1082 and the splitting at 1471 and 1491 cm^{-1}). Due to the used technique, the titania peaks were out of the measurement range, and thus not visible. Also in the IR case, no peaks attributable to the sulfonic groups were seen, but again, this result is not surprising due to their low intensities in the pure powder spectrum (Figure 5.4). An analysis on the membrane crystallinity was performed comparing the intensities of the peak at 1305 cm^{-1} and at 1280 cm^{-1}: as is visible in Figure 5.6, no difference in the peaks inten-

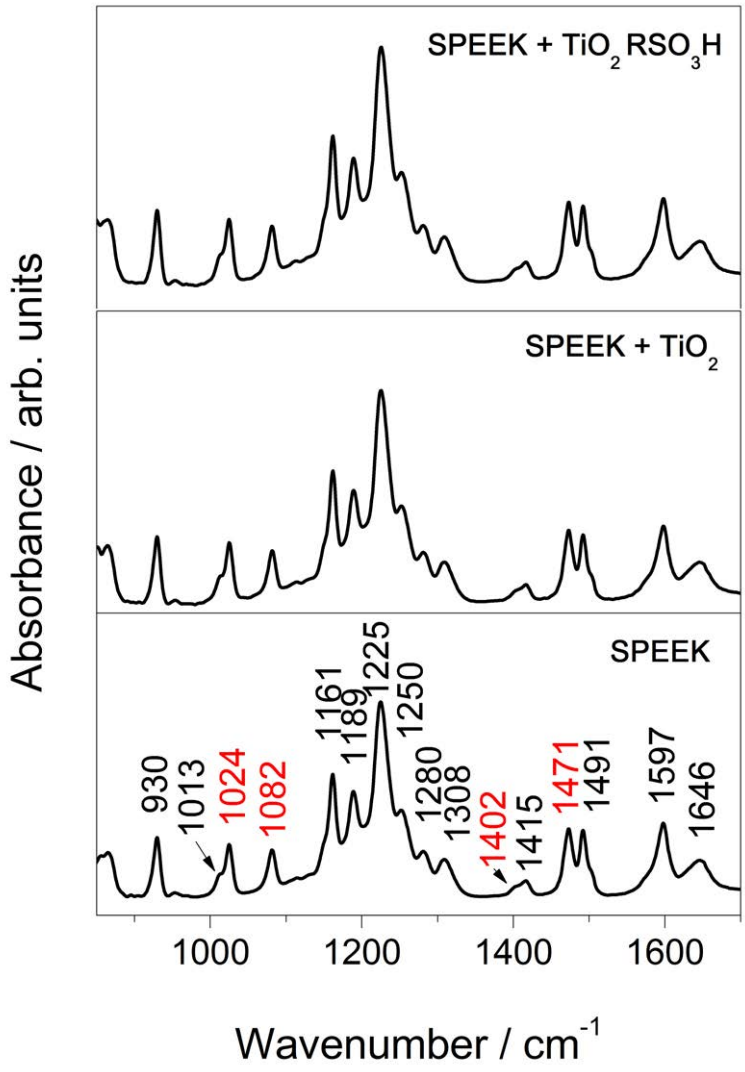

Figure 5.5: Infrared spectra of pure SPEEK (lower panel), SPEEK + TiO_2 (middle panel) and SPEEK + TiO_2SOH_3 (upper panel), collected with LABRAM instrument. In red the peaks due to the PEEK sulfonation.

sities ratio was detectable between the three sample. Moreover, the peak ratio obtained for the pure SPEEK sample revealed that the polymer is prevalently amorphous.

5.6 Conclusion

Pure and propylsulfonic - functionalized nano-titania has been analysed with Raman and Infrared spectroscopy, and the presence of the single anatase

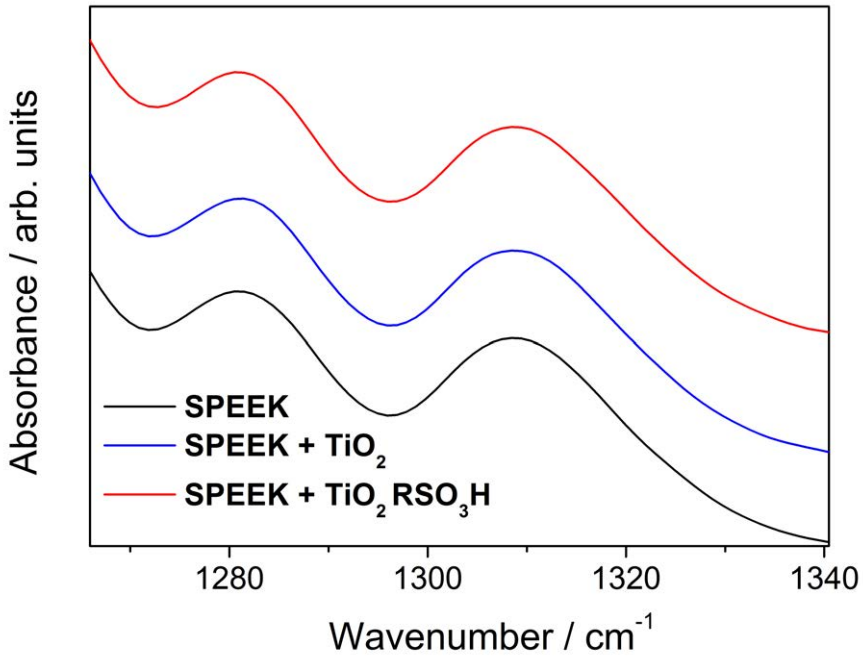

Figure 5.6: The two Chalmer's peak (1280 and 1305 $cm^{-1)}$ for the pure SPEEK (black), SPEEK + TiO_2 (blue) and SPEEK + TiO_2SOH_3 (red)

phase was assessed for both samples. Moreover, the effective functionalization was confirmed with both techniques by the presence of peaks due to sulfonic group vibrations and CH_2 vibrations. As for the SPEEK membrane, all the samples (pure and composite) showed the expected peaks, confirming the PEEK sulfonation. Furthermore, both composite membranes spectra showed the presence of titania. No peak attributable to the titania functionalization was detected, most probably because of the low intensity. A study made with FT-IR spectroscopy on polymer crystallinity revealed that the pure SPEEK is mostly amorphous, and the powder inclusion did not change the polymer crystallinity.

Bibliography

[1] J. M. Chalmers, W. Gasldn, and M. Mackenzie, "Crystallinity in poly(aryi-ether-ketone) plaques studied by multiple internal reflection spectroscopy," *Polymer Bulletin*, vol. 11, pp. 433–435, 1984.

[2] J. Louden *Polym. Commun.*, vol. 27, p. 82, 1986.

[3] K. Chiu and S. Su, "Lithiated and sulphonated poly(ether ether ketone) solid state electrolytefilms for supercapacitors," *Thin Solid Films*, vol. 544, pp. 144–147, 2013.

[4] P. Xing, G. P. Robertson, M. D. Guiver, S. D. Mikhailenko, K. Wang, and S. Kaliaguine, "Synthesis and characterization of sulfonated poly(ether ether ketone) for proton exchange membranes," *Journal of Membrane Science*, vol. 229, pp. 95–106, 2004.

[5] V. Rangasamy, S. Thayumanasundaram, J. W. Seo, and J.-P. Locquet, "Vibrational spectroscopic study of pure and silica-doped sulfonated poly(ether ether ketone) membranes," *Spectrochimica Acta Part A: Molecular and Biomolecular Spectroscopy*, vol. 138, pp. 693–699, 2015.

[6] G. Ellis, M. Naffakh, C. Marco, and P. Hendra, "Fourier transform raman spectroscopy in the study of technological polymers part 1: poly(ary1 ether ketones), their composites and blends," *Spectrochimica Acta Part A*, vol. 53, pp. 2279–2294, 1997.

[7] R. Gosalawit, S. Chirachanchai, S. Shishatskiy, and S. P. Nunes, "Sulfonated montmorillonite/sulfonated poly(ether ether ketone) (smmt/speek) nanocomposite membrane for direct methanol fuel cells (dmfcs)," *Journal of Membrane Science*, vol. 323, pp. 337–346, 2008.

[8] S. Licoccia and E. Traversa, "Increasing the operation temperature of polymer electrolyte membranes for fuel cells: From nanocomposites to hybrids," *Journal of Power Sources*, vol. 159, pp. 12–20, 2006.

[9] D. Cozzi, C. de Bonis, A. DEpifanio, B. Mecheri, A. Tavares, and S. Licoccia, "Organically functionalized titanium oxide/Nafion composite proton exchange membranes for fuel cells applications," *J. Power Sources*, vol. 248, p. 11271132, 2014.

[10] C. de Bonis, A. D'Epifanio, M. L. D. Vona, B. Mecheri, E. Traversa, M. Trombetta, and S. Licoccia, "Proton-conducting electrolytes based on silylated and sulfonated polyetheretherketone: Synthesis and characterization," *Journal of Polymer Science Part A: Polymer Chemistry*, vol. 48, pp. 2178–2186, 2010.

Chapter 6

Conclusions

Different kinds of composite proton exchange membranes, and their relative nano-fillers, have been studied in the present thesis work with Raman and Infrared spectroscopies: SnO_2 with and without sulfate functionalization included in Nafion, sulfated TiO_2 included in Nafion at 2, 5 and 7 weight percentage and pure and propyl sulfonate TiO_2 included in SPEEK.
For all the used fillers, the materials phases and the eventual functionalizations were analysed. As regards the tin oxide powders (F110 and F110S), a mixture of SnO_2 and SnO was found, and the sulfate functionalization of the F110S sample was confirmed, with a monodentate coordination of the sulfate groups to the oxide surface. As for the titanium oxide samples, two different kinds of synthesis and functionalization have been explored: a one-step synthesis and sulfate functionalization for the filler to be included in Nafion membranes (S-TiO_2), and a two step synthesis with a propyl sulfonation for the titania inclusion in SPEEK membranes. Different results were obtained for the two fillers: a prevalent anatase phase with a TiO_2-B component were found in the first filler, an almost pure anatase phase in the second one. However, the functionalizations of both fillers were confirmed and a bidentate sulfate coordination was found in the S-TiO_2 sample. Moreover, for this last filler, a dependence of the sulfate - titania bond on the environmental humidity was recorded, with a partial detachment of the sulfate ions from the oxide surface and a change from bidentate to monodentate coordination of the remaining ones at high relative humidities. However, the persistence of at least a part of the sulfate groups on the powder surface was confirmed, in accordance with TGA results on S-TiO_2 samples subjected to hydrolysis.
As for the composite membranes, all the different PEMs studied presented a high fluorescence signal, but after a regeneration process the composite Nafion samples showed a decreased fluorescence and a good Raman signal to noise ratio. For the SPEEK samples, however, no improvements were ob-

tained with the process, and a long permanence under the laser was necessary before each Raman measurement to partially quench the fluorescence signal and obtain a discrete signal to noise ratio. In this case, unfortunately, the long exposure time of the sample to the laser turned out to change the measurement parameters, thus preventing Raman analysis at defined conditions.
For all the composite membranes the effective filler inclusion was confirmed, and the S-TiO_2 composite membranes showed a trend in the filler peaks intensities in accordance with the different amount of nano-powder included (2, 5 and 7 %). Moreover, for these last samples, a peak at about 1000 cm^{-1} in the Raman spectrum confirmed the persistence of the filler functionalization even after the inclusion into the polymer matrix. The same did not happened for the F110S powder: no sulfate peak was detected in the composite membrane, and EDX measurements confirmed the absence of excess sulfur in the polymer, suggesting a probable detachment of the sulfate groups during the filler incorporation into the Nafion matrix. As for the propyl sulfonate TiO_2, the functionalization presence was not possible to confirm, due to the low intensities of the related peaks. The Nafion + S-TiO2 samples were characterized by an irregular morphology, not present in the pure Nafion and in the tin oxide composite membrane, caused by a not homogeneous filler distribution. This inhomogeneity was common to all the different nano-filler percentage explored (2, 5 and 7%), but with an important difference: while in M5 and M7 samples the filler was present in all the membrane surface, even if not in the same amount, in the M2 sample filler free zones were detected. The presence of these zones could break the protons percolation paths, with a negative impact on the membrane proton conduction.
For both tin and titanium oxide composite Nafion, a detailed Raman analysis, never performed before on composite membranes, was carried out at different ambient relative humidities. The SO_3^- peak position revealed important differences between pure Nafion and the composite membranes and in combination with water uptake measurements this results highlighted a different water distribution inside the composite membrane at high relative humidity due to the fillers presence.
This finding underlines how the prediction of the effects of a metal oxide inclusion inside the Nafion matrix is not straight forward. The fillers in fact were added to increase the membrane water uptake, but what really happen is more complicated: at high RH an effective increase in the water content near the powder is counterbalanced by a lower hydration near the sulfonate ions. Moreover, in the S-TiO_2 membranes case, a different inner environment was found also at low relative humidity with respect to pure Nafion, and subsequent FT-IR measurements revealed that its cause is a probable filler -

membrane interaction, that resulted in a lower net charge perceived by the sulfonate ions. A S-TiO_2 effect on the Nafion structure was revealed also by FT-IR. In general the presence of an interaction between powder and polymer is beneficial for the membrane proton conduction at critical conditions, when, due to the lack of water, the proton movement is strongly depend on the number of possible hopping paths. This beneficial effect is in fact confirmed by the results of membrane resistance obtained in-situ for the M5 sample: compared to pure Nafion, higher conduction values were measured at 30 % RH, in particular at high temperatures.
The peak position of the SO_3^- group at different RH conditions in the Nafion + S-TiO_2 samples was studied also at 60 °C, to explore a temperature closer to the real fuel cell working conditions. At low relative humidities the divergence observed between pure Nafion and composite membranes was even more evident than at room temperature, while at high RH the obtained results need further investigations in order to be satisfactorily explained, a study that hopefully will be performed in the near future.

List of Tables

List of Figures